Langasite Bulk Acoustic Wave Resonant Sensor for High Temperature Applications

by

Huankiat Seh

Bachelor of Engineering, First Class
Imperial College (London, United Kingdoms), 1998

Submitted to the Department of Materials Science and Engineering
in Partial Fulfillment of the Requirements for the
Degree of Doctor of Philosophy in Electronic, Photonic and Magnetic Materials

at the

Massachusetts Institute of Technology

February, 2005

Signature of Author: ____

Huankiat Seh
Department of Materials Science and Engineering
3 January 2005

Certified by: ____

Harry L. Tuller
Professor of Ceramics and Electronic Materials
Thesis Advisor

Accepted by: ____

Carl V. Thompson II
Stavros Salapatas Professor of Materials Science and Engineering
Chair, Departmental Committee on Graduate Students

Langasite Bulk Acoustic Wave Resonant Sensor for High Temperature Applications

by

Huankiat Seh

Submitted to the Department of Materials Science and Engineering on **3 January 2005** in
Partial Fulfillment of the Requirements for the Degree of Doctor of Philosophy in
Electronic, Photonic and Magnetic Materials

ABSTRACT

The high temperature transport properties of langasite, $La_3Ga_5SiO_{14}$, were investigated with special attention focused on their potential impact on the utilization of langasite as a mass sensitive resonant platform for high temperature sensor applications. The electrical properties of acceptor and donor doped langasite were examined at temperatures ranging from 700 to 1000°C, and pO_2 of 1 to 10^{-25}atm. Acceptor doped langasite was shown to exhibit mixed ionic-electronic conductivity behavior, with predominant ionic conduction due to mobile oxygen vacancies at high pO_2, and n-type electronic conduction due to electrons at low pO_2. Increasing acceptor level resulted in the appearance of p-type hole conduction at high pO_2 and increased ionic conductivity, while the n-type electron conduction was depressed. Donor doped langasite was shown to be electronic at all temperatures and pO_2.

The electron mobility of langasite was found to be activated (polaron hopping) with an activation energy of 0.15(±0.01)eV, whereas the holes were assumed to be quasi free carriers. The activation energy for oxygen vacancy migration was estimated to be 0.91(±0.01)eV under dilute solution conditions and 1.27(±0.02)eV for 1%Sr level under concentrated solution conditions. Both values of activation energy of ionic conductivity-temperature product are consistent with activation energy of oxygen self-diffusivity in the respective materials.

The electrical properties were related to the underlying defect and transport processes using defect modeling. The self consistent defect model established the defect chemistry of langasite, enabling important parameters describing reduction (E_r=5.70±0.06eV and 6.57±0.24eV for acceptor and donor doped langasite respectively) and oxidation (E_o=2.18±0.08eV), intrinsic electron-hole generation (E_g≈4.0-4.4eV) and defect ionization (E_{D_ion}=1.52±0.06eV for Nb ionization), to be extracted. The predictive defect model was used to calculate the dependence of the partial ionic and electronic conductivities and mass change as functions of temperature, dopant level and pO_2. Given that the magnitudes of conductivity and mass change directly affect the resolution and sensitivity limits of langasite resonators, their predictions allowed for the definition of acceptable operating limits and/or the design of properties for optimum resolution and sensitivity.

Two high temperature applications of resonant sensors were studied. Praseodymium-cerium oxide was selected for oxygen partial pressure monitoring and is representative of films which change mass upon absorption or desorption of gaseous species. Barium carbonate film was selected for NO_2 sensing and is representative of films which change mass upon reaction with the gas phase to form a new product phase. Both sensors showed sensitivity to their respective target chemicals and demonstrated the feasibility of high temperature sensor applications. The performance of each sensor was discussed and suggestions for improving sensor performance were presented.

Thesis Advisor: Harry L. Tuller

Title: Professor of Ceramics and Electronic Materials

Biographical Note

I was born in Singapore in 1974. I went through primary school, secondary school and junior college in Singapore, before joining the army to fulfill my national service obligation. I was commissioned as a junior officer and after about two years I left for college. I applied and was accepted to the materials science department at Imperial College, London.

London was a great city and spending my undergraduate life there was satisfying and fun. Materials science at Imperial College tended to be metallurgy-oriented. The class was very international and it was interesting to meet many with different backgrounds. I had an electroceramics class by Professor Kilner and got to like it.

At the end of my second year, I was offered a place at the department of materials science at MIT. I accepted the offer and came to MIT in 1998. I then joined Professor Tuller's group to work on electroceramics and started on the langasite project.

Education

Bachelor of Engineering (First Class), Imperial College (London, UK), 1995-1998.

Patent

H. L. Tuller, H. Seh, T. Hyodo, *High-Temperature Gas Sensors*. 2004. Patent pending.

Publications

1. H. Seh, H. L. Tuller, H. Fritze, *Defect properties of langasite and effects on BAW gas sensor performance at high temperatures*. Journal of the European Ceramic Society, 2004. **24**(6): p.1425-1429.
2. H. Seh, H. L. Tuller, H. Fritze, *Thin Film Praseodymium-Cerium Oxide Langasite-Based Microbalance Gas Sensor,* J. Electroceramics, in press.
3. H. Seh, T. Hyodo and H. L. Tuller, *Bulk Acoustic Wave Resonator as a Sensing Platform for* NO_x *at High Temperatures*, Sensors and Actuators, in press.
4. M.Schulz, H.Fritze, H. L. Tuller, H. Seh, *Diffusion Related Implications for Langasite Resonator Operation*, IEEE Transactions on Ultrasonics, Ferroelectrics, and Frequency Control, **51**, 1381-1387 (2004).
5. Huankiat Seh, Takeo Hyodo, and Harry L. Tuller, *Porous Barium Carbonate Film on Resonator for* NO_2 *Detection at High Temperatures*, Proc. MIT-Tohoku "21COE" Joint Workshop on Nano-Science in Energy Technology, Sept.27-28, 2004, MIT, Cambridge, MA. pp. O-07-1 to O-07-5
6. H. Fritze, M. Schulz, H. Seh, H. L. Tuller, *High Temperature Operation and Stability of Langasite Resonators*, Symposium on Solid State Ionic, MRS, Boston, December, 2004, accepted for publication.
7. H. Fritze, O. Schneider, H. Seh, H. L. Tuller, G. Borchardt, *High temperature bulk acoustic wave properties of langasite*. Physical Chemistry Chemical Physics, 2003. **5**(23): p.5207-5214.

8. H. Seh, H. L. Tuller, H. Fritze, *Electrical conductivity prediction in langasite for optimized microbalance performance at elevated temperatures*. Materials Research Society Symposium Proceedings, 2003. **756**: p.175-180.
9. H. Seh, H. L. Tuller, H. Fritze, *Langasite for high-temperature acoustic wave gas sensors*. Sensors and Actuators B, 2003. **93**(1-3): p.169-174.
10. H. Fritze, H. Seh, O. Schneider, H. L. Tuller, G. Borchardt, *Thin film stoichiometry determination by high temperature microbalance technique*. Materials Research Society Symposium Proceedings, 2003. **756**: p.181-186.
11. Harry L. Tuller, Yongki Min and Huankiat Seh. *Thin Film and Resonant Sensors*, The 1st AIST International Workshop on Chemical Sensors, Synergy Materials Research Center, Nat. Inst. of Adv. Ind. Sc. and Tech., Nagoya, Japan, March 13, 2003, pp. 45-56
12. H. Fritze, G. Borchardt, H. Seh, H. L. Tuller, Sensor Concept based on High Temperature Piezoelectric Materials, Sensor 2001 Proceedings, Nürnberg, Germany, May 8-10, 2001, pp. 177-82 (Publisher: AMA Service GmbH, P.O. Box 2352, 31506 Wunstorf, Germany).
13. H. Fritze, H. Seh, H. L. Tuller, G. Borchardt, *Operation limits of langasite high temperature nanobalances*. Journal of European Ceramic Society, 2001. **21**(10-11): p.1473-1477.
14. H. Fritze, H. L. Tuller, H. Seh, G. Borchardt, *High temperature nanobalance sensor based on langasite*. Sensors and Actuators B, 2001. **76**(1-3): p.103-107.
15. K.-L. Choy, H. Seh, *Fabrication of Ni-*Al_2O_3*-based reforming catalyst using flame – assisted vapour deposition*. Materials Science and Engineering A, 2000. **A281**(1-2): p.253-258.

Acknowledgments

First of all, I would like to thank my advisor Professor Harry Tuller. He is knowledgeable, accessible and supportive, and this thesis would not be possible without his guidance. He has made my doctoral experience immensely enjoyable. I would also like to thank my committee members, Professor Scott Manalis and Professor Bernhardt Wuensch for their feedback and constructive criticisms.

A lot of people have contributed to this work, but I would like to especially mention and thank Dr. Holger Fritze. The many discussions I had with Dr. Fritze have provided important technical and theoretical insights to the working of high temperature langasite resonators. The collaborations between his group and ours have been extremely fruitful over the duration of my stay at MIT.

I have to also say that Professor Tuller's group has some of the best people that I have worked with. Not only do we work together, we had frequent group lunches, ski trips, climbing trips et cetera, which greatly enhanced my MIT experience. Todd, who joined the group at about the same time as I did, had been incredibly helpful with experimental problems I ran into. Zachi was always the person to turn to when I ran into computer or programming problems. Yongki, who had worked in Daewoo before joining the group, was knowledgeable and had provided a lot of technical advices on thin film processing. Takeo, who visited the group for a few months, had made important and direct contributions to the processing of silica and barium carbonate porous films. I also have great discussions about defect chemistry and modeling with Cengiz and Avner. The serious and not-so-serious discussions with Josh and Scott will always be remembered.

There are many people I have met at MIT that made the entire doctoral process much more than just research work. I participated in the 50K entrepreneur competition with Justin, Felix and Patrick; that has been a great learning experience. Dilan, who I have known since my undergraduate years, has been a great friend, roommate and climbing partner. I learned photography and hiking skills from Sybor, and I still derive a great deal of pleasure pursuing both pastimes. I started out ice-climbing with Steve who bravely agreed to accompany me. Kahshin convinced me that walking up Mount Rainier was fun, which I agree wholeheartedly even though we went only halfway. I have to thank Liangyu whose love and support made setbacks bearable and successes sweeter. Her encouragement, advice and company are always valuable.

Lastly, I have to give my thanks to my family. My parents, whose supports were essential in getting me to where I am today, have shared with me the ups and downs in my life. My sister, who stayed with me when she went to Boston University, had made leaving home tolerable during those years she was in Boston. My brother still cracks me up when he calls, and it is always great to hear from him when I am stressed out.

Table of Contents

List of Figures

List of Tables

Chapter 1: Background

1.1 Introduction

1.1.1 Motivations

Growing interest in environmental monitoring for health and security reasons, for achieving improved combustion efficiency and feedback control in industrial processes have all stimulated interest in chemical sensors. To achieve improved sensitivity and selectivity coupled with low cost, attention is being focused on sensor miniaturization, and their integration with electronic circuits and devices. Many different approaches are being pursued for chemical monitoring including electrochemical, chemoresistive, mass spectroscopic, optical and acoustic approaches. In this work we focus on acoustic wave devices given their characteristically high sensitivity, relatively low power consumption and suitability for wireless operation [1-8]. Increasingly, miniaturized resonators are being utilized, either singly or as an element in an array [9-13], to achieve increased sensitivity and selectivity (in the case of an array) and to lower power consumption.

One important application area is in-situ high temperature monitoring of various chemical processes, including emissions monitoring and/or process control. Acoustic wave sensors are good candidates for monitoring several industrial parameters simultaneously. Beside their inherent sensitivity to chemical species via mass loading (e.g. adsorption), they also exhibit sensitivity to fluid flow, temperature, and viscosity [14-21]. In addition, passive acoustic sensors (e.g. surface acoustic wave devices) can be wirelessly interrogated through inductive coupling, making it attractive for sensing applications in hostile environments [22-26]. By using an array of such sensors, a complete sensor system can, in principle, be designed.

To date, acoustic wave devices have rarely been used in high temperature applications given that few materials are known to remain stable as well as retain their piezoelectric properties under these conditions. For example, the most commonly used acoustic sensing material is single crystal alpha-quartz. Quartz is limited by high losses at high temperature and a destructive phase transformation (from alpha to beta quartz) at 573°C [27-30]. The other commonly used or investigated materials, such as $LiNbO_3$ [31, 32], $LiTaO_3$ [33, 34] and $Li_2B_4O_7$ [35, 36], for related reasons, also have maximum operating temperatures between 300 and 500°C [37]. Hence, there is the need for alternative materials which can operate at higher temperatures. Understanding the relationships between the material and device properties at high temperatures and their impact on sensor performance are the motivations behind this work.

1.1.2 Acoustic Devices as Chemical Sensors

The performance of a chemical sensor can be characterized by its sensitivity, selectivity, response time, reproducibility and long term stability [3, 38-41]. Definitions of these performance parameters are general to all sensor types. Sensitivity is defined as the ratio of the change in the sensor response to the change in the quantity of the target chemical. Selectivity is the ability of a sensor to differentiate between different chemical species, i.e. the ratio of sensitivity to different chemical species. Response time is defined as the time it takes for the sensor to achieve 90% of its steady state response. Reproducibility refers to the reversibility of each reading and the consistency of response to the same chemical species. The speed of that process also influences the maximum number of measurements the sensor can repeat in a certain time frame, which may be important in some applications. Long term stability refers to drift in sensor reading over an extended period of time. All of these are important factors determining the viability of the sensor as a commercial product.

An acoustic wave chemical sensor responds to changes in chemical potential by detecting changes in its mass via a change in resonant frequency [20, 39, 42]. The operation of the device depends on the use of an active film, supported on the resonator, which interacts with the gas phase. Thus, understanding the roles that the resonator and the active film play in the sensor operation is important in striving for sensor optimization. For example, the total sensitivity of a chemical acoustic sensor is influenced by both the mass sensitivity of the resonator and the chemical sensitivity of the active layer. The selectivity largely depends, however, on the active layers. This allows the independent optimization of the acoustic device for high mass sensitivity and the active film for selectivity, giving many interesting application possibilities.

1.2 Bulk Acoustic Wave Resonator

1.2.1 Theory

A resonator can be used as a sensor by monitoring the change in wave velocity and/or attenuation when it interacts with the environment. A bulk transverse shear mode (TSM) is commonly utilized with the prime example being the quartz crystal microbalance (QCM) [5, 43-45]. A schematic of a QCM resonator is shown in Figure 1.

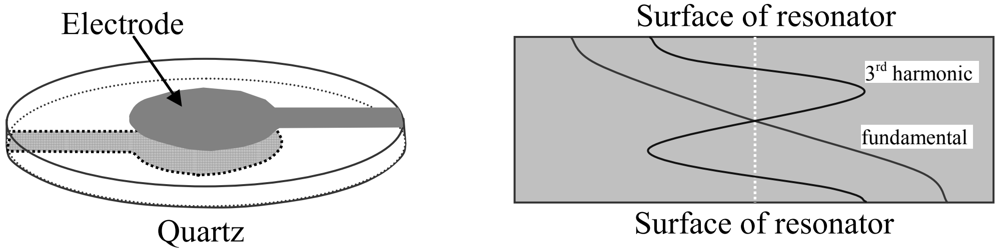

Figure 1: Quartz Crystal Microbalance, a transverse shear wave resonator. The allowable wavelengths are determined by the resonator thickness (see Eq.(1)) with maxima at the two surfaces of resonator (see right).

In a TSM resonator, an alternating voltage is applied to the electrodes to generate standing shear waves with maxima at the crystal surfaces (Figure 1, right), making the resonator sensitive to perturbations at the faces. The wavelength λ, the resonant frequency f_N, and the shear wave velocity v_s are given by:

$$\lambda = 2t_s/N \text{ or} \tag{1}$$

$$f_N = Nv_s/2t_s \text{ and} \tag{2}$$

$$v_s = (\mu_q/\rho_q)^{1/2} \tag{3}$$

where N= odd integers, t_s = thickness of resonator, μ_q: shear stiffness and ρ_q: mass density of resonator.

The basis for detection of surface perturbations, e.g. mass change, is given by the Rayleigh criterium. The Rayleigh criterium states that '*resonance in a mechanical system occurs at frequencies at which the peak kinetic energy exactly balances the peak potential energy. The accumulation of mass on the crystal surface causes an increase in kinetic energy without changing the potential energy*' [39]. During a mass change on the surface, in order that U_p (peak potential energy) and U_k (peak kinetic energy) are equal, the resonator will therefore change its resonant frequency, resulting in:

$$\left(\frac{\varpi_o}{\varpi}\right)^2 = 1 + \frac{2\rho_s}{t_s\rho_q} \tag{4}$$

where ρ_s is the areal mass density (i.e. mass per unit area) of mass layer on resonator and $(N\pi/t_s)(\mu_q/\rho_q)^{1/2} = \omega_o$ as shown in Eq. (2) (see Figure 2).

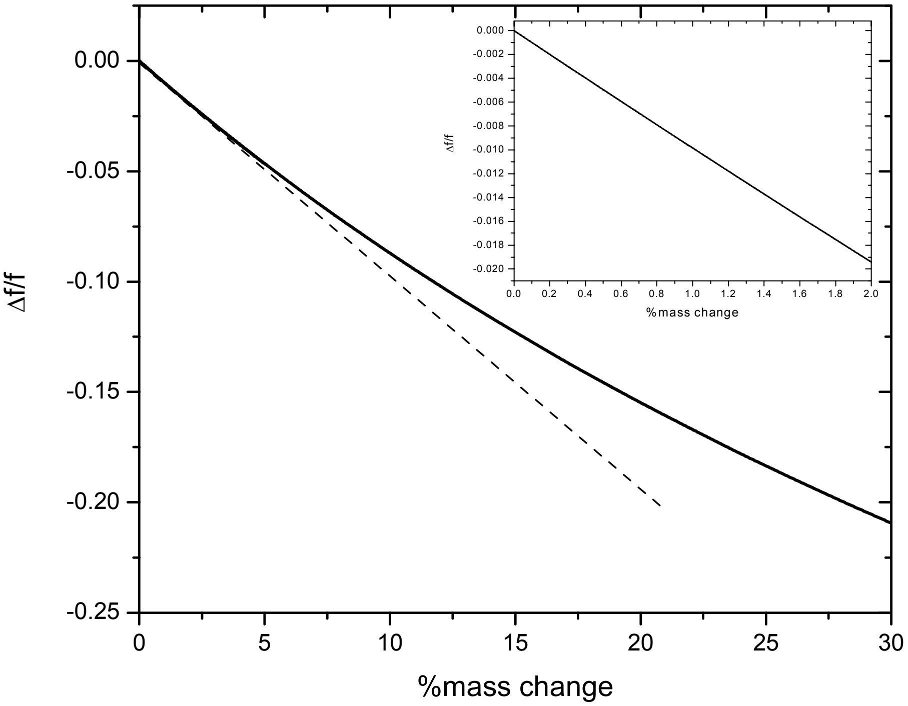

Figure 2: Δf/f versus percentage mass change. If the mass change is small, a linear approximation is valid (see insert).

For a small mass change (i.e. 2% or less, see Figure 2), a linear approximation can be made and Eq. (4) can be rewritten as:

$$\frac{\Delta f}{f_o} = -\frac{\rho_s}{t_s \rho_q} \qquad (5)$$

Eq. (5) indicates that a fractional shift in resonant frequency is equal to a fractional change in mass. By combining Eq. (4) and (5), we obtain the so-called Sauerbrey equation, commonly used to relate change in TSM resonant frequency to changes in surface mass density ρ_s:

$$\Delta f = -\frac{2 f_1^2 \rho_s}{(\mu_q \rho_q)^{1/2}} \qquad (6)$$

where f_1=fundamental frequency, ρ_s=mass/area of the layer whose mass is changing, ρ_q=mass/volume of resonator, μ_q=shear stiffness.

The Sauerbrey equation makes the assumption of ideal mass layer (no energy lost). On a TSM resonator, a film is considered ideal if it is thin and rigid, and therefore moves synchronously with the oscillating surface. More quantitatively, the acoustic phase shift ϕ across the film must fulfill $\phi << \pi$, in which the phase shift can be calculated using:

$$\phi = \omega t \left(\frac{\rho}{G} \right)^{1/2} \qquad (7)$$

where ρ: film density, G: shear modulus, t: thickness.

Furthermore, a quality factor Q can be defined. Several definitions exist, one of which uses the U_p (peak potential energy) and P_d (power loss in lossy medium), which is defined as $P_d = 2\alpha P_0 e^{-2\alpha x}$, where x is the distance from the wave source and α is the loss coefficient. In this case, the quality factor, Q, is defined as:

$$Q = \omega U_p / P_d \qquad (8)$$

where ω is the angular frequency.

A more visual definition is:

$$Q = f_o/\Delta f \quad (9)$$

where f_o is the resonant frequency and Δf is the width at half-height. Q represents the resonant stability of the resonator and affects the resolution at which the resonant frequency can be measured. Hence, for high resolution mass detection, a high Q is necessary.

1.2.2 Equivalent Circuit Model

Above, the theory of mass detection in piezoelectric resonators was discussed. Practically, one must be able to measure the mechanical resonant frequency electrically, which is simpler to implement and compatible with sensing electronics. In order to establish the relationship between the measured electrical response and the mechanical properties, the resonant system can be approximated by an equivalent circuit model know as Butterworth-van Dyke circuit [46]:

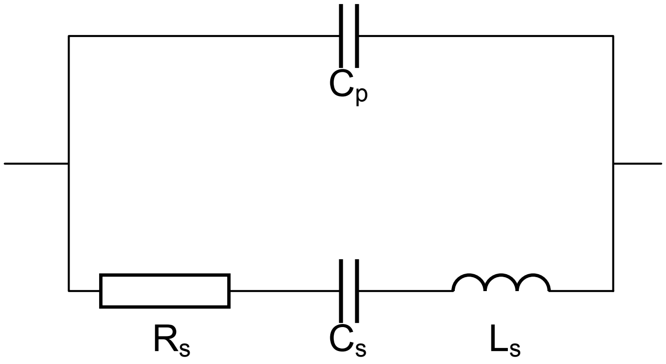

Figure 3: Butterworth-van Dyke equivalent circuit.

C_p is the static capacitance (from the layer sandwiched by the two electrodes and the parasitic capacitance from the test fixture). R_s, C_s and L_s give the motional contributions due to the electromechanical coupling of the piezoelectric material. The static capacitance dominates the electrical behavior far from resonance and the motional contribution dominates near the resonance. The model provides simulation of the TSM resonator electrical characteristic near the resonant frequency.

The elements of the circuit correspond to physical properties of the resonator as listed below [46]:

Static Component

$$C_p = \frac{\varepsilon_{22} A}{t_s} \tag{10}$$

Motional Components

$$C_s = \frac{8K^2 C_p}{(N\pi)^2} \tag{11}$$

$$L_s = \frac{1}{\omega_s^2 C_s} \tag{12}$$

$$R_s = \frac{\eta_q}{\mu_q C_s} \tag{13}$$

where:

η_q = effective viscosity

μ_q= shear stiffness

K^2 = electromechanical coupling coefficient

ρ_q = mass density

ω_s = angular series resonant frequency (unperturbed)

ε_{22} = dielectric permittivity

A = electrode area

t_s = resonator thickness

From the equivalent circuit, the following equations can be written to describe the circuit behavior [46]:

$$Z = \frac{\omega L_s - \frac{1}{\omega C_s} - jR_s}{\omega C_p R_s + j\left[\omega C_p\left(\omega L_s - \frac{1}{\omega C_s}\right)\right] - 1} \tag{14}$$

From this Butterworth-van Dyke circuit (Figure 3) and Eq. (14), six characteristic frequencies can be defined and measured (Figure 4). They are:

1. ***f_m***: frequency at which |Z| is at the minimum
2. ***f_n***: frequency at which |Z| is at the maximum
3. ***f_s***: series frequency defined as $f_s = \dfrac{1}{2\pi(L_s C_s)^{1/2}}$ (15)
4. ***f_p***: parallel frequency defined as $f_p = \dfrac{1}{2\pi}\left[\dfrac{1}{L_s}\left(\dfrac{1}{C_s}+\dfrac{1}{C_p}\right)\right]^{1/2}$ (16)
5. ***f_r***: resonant frequency where Im(Z) is zero
6. ***f_a***: antiresonant frequency where Im(Z) is also zero ($f_a > f_r$)

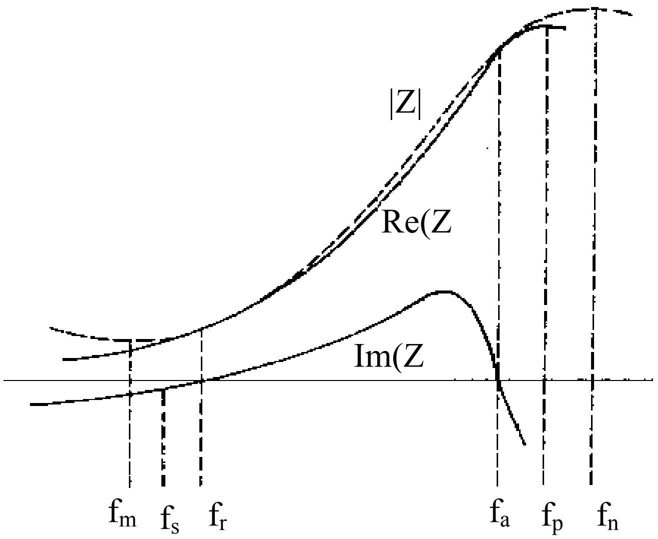

Figure 4: Re(Z) and Im(Z) plot of the equivalent circuit near the resonant frequency. Various characteristic frequencies are shown [46].

In the circuit model, another definition of quality factor Q can be derived: $Q = \omega_s L_s / R_s$, where ω_s is the series angular frequency, and is not unlike the Q defined in mechanical terms.

All these frequencies are shown again in the complex plot of Z of the equivalent circuit (Figure 5). For finite Q, $f_m < f_s < f_r$, and the $f_n < f_p < f_a$. The higher the Q, the closer f_m is to f_r, and f_n to f_a. At infinite Q, $f_m = f_r = f_s$, and $f_n = f_a = f_p$.

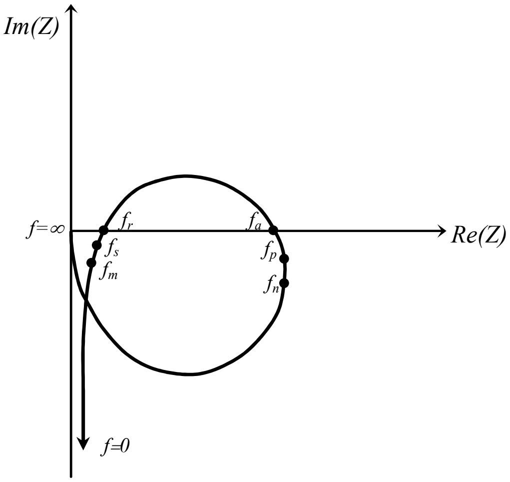

Figure 5: Im(Z) vs Re(Z) plot with the positions of the characteristic frequencies.

With the addition of a general surface perturbation (e.g. surface mass change), an additional motional impedance Z_e can be added to the equivalent circuit.

$$Z_e = R_m + j\omega L_m \tag{17}$$

R_m and L_m in Eq. (17) are defined as:

$$R_m = \frac{N\pi}{4K^2\omega_s C_p}\left(\frac{\mathrm{Re}(Z_s)}{Z_q}\right) \tag{18}$$

$$L_m = \frac{N\pi}{4K^2\omega_s C_p}\left(\frac{\mathrm{Im}(Z_s)}{Z_q}\right) \tag{19}$$

where $Z_q = \left(\rho_q \mu_q\right)^{1/2}$ and $Z_s = \frac{T_{xy}}{v_x}$, T_{xy} is the force/area in the x-direction on the resonator surface (assume y-face), v_x is surface shear particle velocity in the x-direction.

The new equivalent circuit, taking into account mass perturbation, is shown in Figure 6, which results in a shift in the characteristic frequencies. And the motional impedance is now given by:

$$Z_m = \left(R_s + R_m\right) + j\omega\left(L_s + L_m\right) + \frac{1}{j\omega C_s} \tag{20}$$

Due to this, the series resonant frequency will change according to (R_m is zero, assuming mass layer is ideal):

$$\Delta f_s = -\frac{L_m f_s}{2(L_s + L_m)} \approx -\frac{L_m f_s}{2L_s} \tag{21}$$

From [46], it is shown that:

$$L_m = \frac{2\omega_s L_s \rho_s}{N\pi\sqrt{\mu_q \rho_q}} = \frac{N\pi\rho_s}{4K^2\omega_s C_p\sqrt{\mu_q \rho_q}} \tag{22}$$

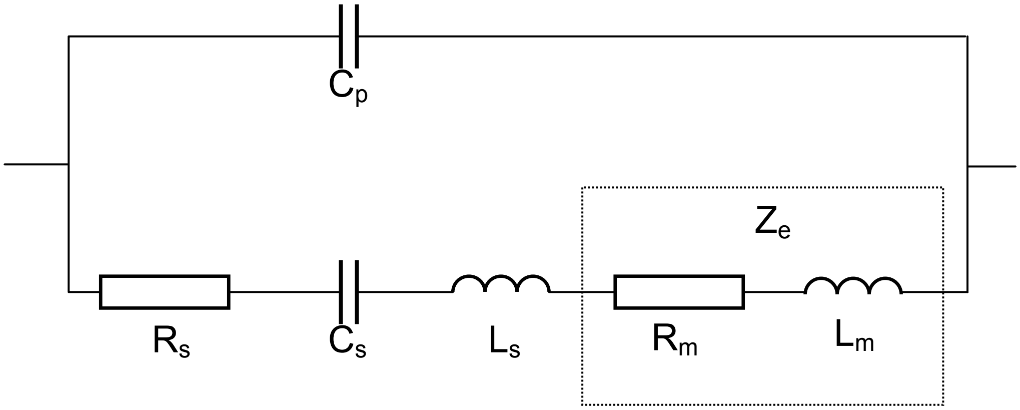

Figure 6: Equivalent circuit with additional *Z*Z_e simulating surface perturbation.

The shift in series resonant frequency could be obtained by substituting Eq. (22) into Eq.(21), giving the Sauerbrey Equation, similar to that obtained from a mechanical derivation (Eq. (6)):

$$\Delta f_s \approx -\frac{L_m f_s}{2L_s} = -\frac{2 f_1^2 \rho_s}{(\mu_q \rho_q)^{1/2}} \tag{23}$$

1.2.3 High Temperature Circuit Model

Due to the increased electrical conductivity at high temperature, electric losses in the resonator become significant. To describe that phenomenon, an additional circuit element, a parallel resistance R_p, has to be added to the equivalent circuit (Figure 6) to account for the resistive loss [47, 48]. The final circuit model used is shown in Figure 7.

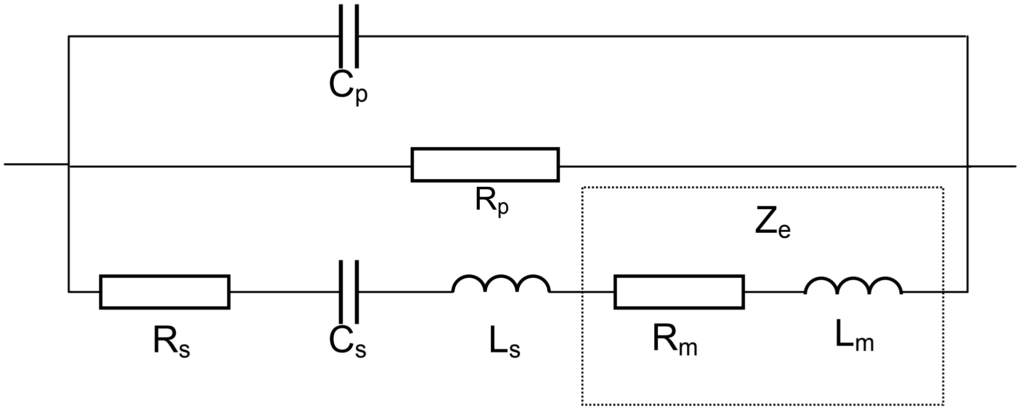

Figure 7: Modified equivalent circuit for resonator at high temperature.

The additional resistive element R_p is the bulk resistance, which becomes sufficiently small (i.e. when R_p is within an order of magnitude of R_s) at elevated temperature and certain oxygen partial pressures, causing the attenuation of the resonant signal (i.e. electrical losses), e.g. Figure 8. The increased electrical losses that are associated with that decrease in bulk resistance can be controlled through material design, e.g. decreasing electrical conductivity via doping. In addition, with the addition of R_p, a new Q-factor can be defined [49]:

$$Q_{modifed} = \frac{R_p}{\left(R_s^2 + R_s R_p\right)} \sqrt{\frac{L_s}{C_s}} \tag{24}$$

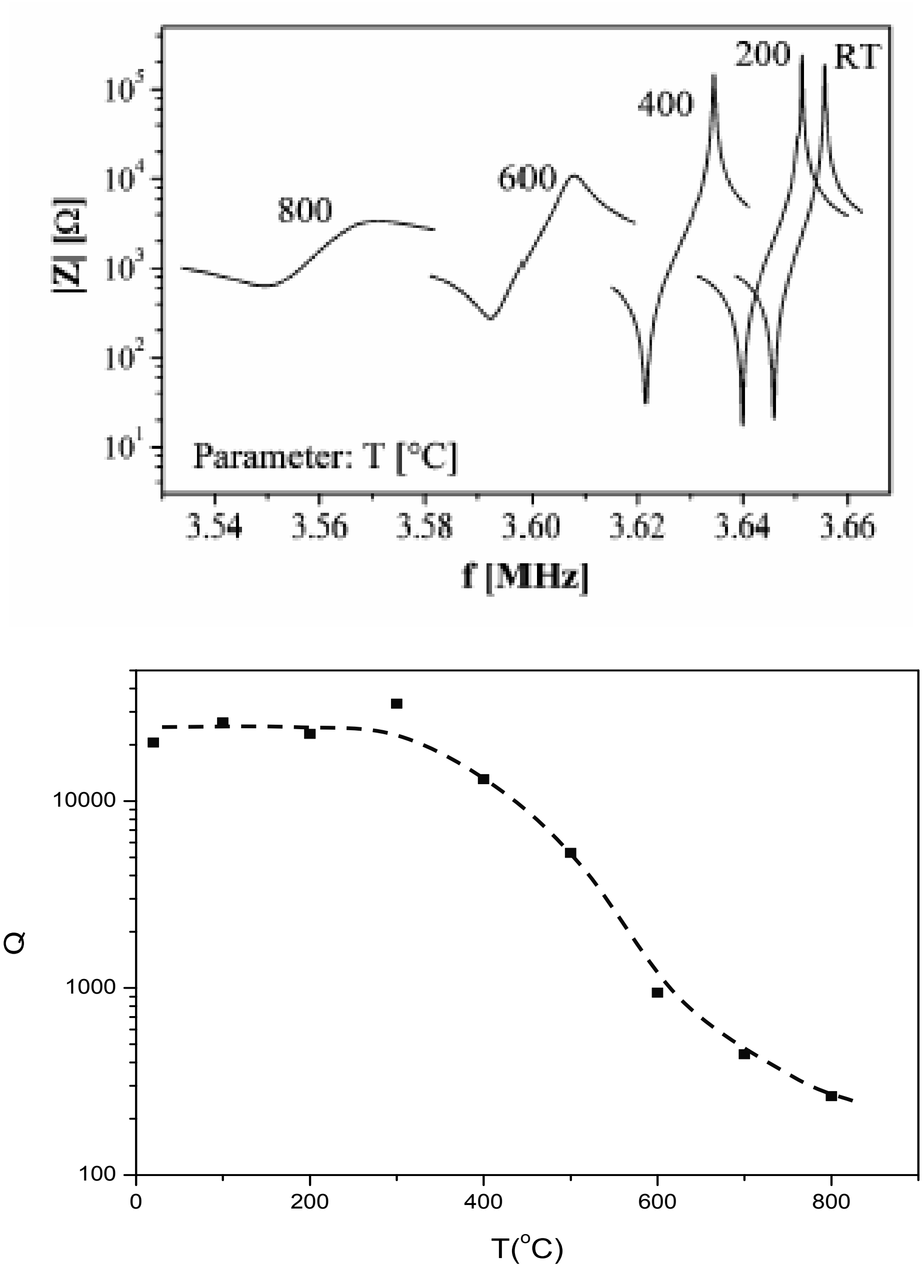

Figure 8: Increasing attenuation of resonant signal of a langasite resonator at pO_2=1atm. The left shows the attenuation of the resonant signal, and the right shows the decrease in quality factor *Q* with temperature [50].

1.3 High Temperature Piezoelectric Materials

Materials that show promise for high temperature operation include: $La_3Ga_5SiO_{14}$ (LGS or langasite) [51-57], (Al,Ga)N [58-61] and $GaPO_4$ [49, 62-67]. Langasite appears attractive given the absence of phase transitions up to its melting point of 1470°C (see Table 1). Indeed, surface acoustic (SAW) devices, based on langasite have been operated up to a temperature of 1000°C [68]. These developments together point to the potential use of langasite resonators as the basis of a chemical sensor platform, with ability to operate at elevated temperatures. This provides the opportunity to extend the operation of resonant sensors to harsh environments including the realm of automotive and industrial process control applications.

Table 1: Temperature limitation of piezoelectric materials.

Piezoelectric Material	*Max Operating Temp (°C)*	*Remarks*
$LiNbO_3$	≈ 300	High Li vapor pressures
$LiTaO_3$	≈ 300	High Li vapor pressures
α-Quartz	573	Phase transformation
$Li_2B_4O_7$	≈ 230	Excessive ionic conductivity
$AlPO_4$	580	Phase transformation
$GaPO_4$	933	Phase transformation
$La_3Ga_5SiO_{14}$ (langasite)	1470	Melting point
AlN	≈ 1040	Oxidation

Growth of single crystal langasite is suitable for large-scale commercial production. Up to 3" wafers of langasite have been grown on a consistent basis [69, 70], and larger wafer sizes were grown experimentally [71, 72]. The langasite family also contains other materials with similar structure such as $La_3Ga_{5.5}Nb_{0.5}O_{14}$ (langanite) and $La_3Ga_{5.5}Ta_{0.5}O_{14}$ (langatate), which were also investigated [55-57, 73]. On the other hand, (Al,Ga)N oxidizes at about 1040°C and cannot be grown as large single crystals [58-61]; and while

$GaPO_4$ has an operation ceiling of 933^{o}C, it is not available as large size wafers due to difficulties with the growth process [64, 66, 68].

To date, studies on langasite have concentrated on its applications at or near room temperature (e.g. radio frequency filters as quartz replacements, Mitsubishi Materials Corp). Key properties of langasite are listed in Table 2 [56, 74-77].

Table 2: Properties of langasite.

Physical	
Density (kg/m^3)	5764
Melting point (^{o}C)	1470
Phase transition temperatures (^{o}C)	None (from room temperature to its melting point)
Moh's hardness	6.6
Crystal Structure	Trigonal, point group 32, space group P321
Lattice parameter (Å)	a = 8.1-8.2, c = 5.1-5.2
Coeff. Thermal Expansion (ppm/K)	$\alpha_{11} = 5.1$ $\alpha_{33} = 3.6$
Elastic compliances (10^{12} M^2/N)	$s_{11} = 8.75$, $s_{33} = 5.31$ $s_{12} = -4.02$, $s_{13} = -1.88$ $s_{44} = 21.99$, $s_{66}=25.54$

Piezoelectric (Y-cut when not specified)	
K^2 (%)	0.3-0.4
Acoustic velocity (m/s)	2400
Temperature coefficient (ppm/K)	1-2 (room temp)
Frequency constant (kHz.mm)	1380
Piezoelectric constant (10^{12} C/N)	$d_{11} = -6.2$, $d_{14}=5.4$
Attenuation value (dB/cm)	1.9 (shear mode), 0.5(long. mode)

Langasite has a chemical formula of $A_3BC_3D_2O_{14}$ [37, 78], where A, B, C and D indicate particular cation sites. *A* is a *decahedral* (Thomson cube) site coordinated by 8 oxygen atoms. *B* is *octahedral* site coordinated by 6 oxygen atoms, and *C* and *D* are *tetrahedral* sites coordinated by 4 oxygen atoms. The crystal structure is shown in Figure 9 [78]. The attractiveness of langasite is further enhanced by the possibility of materials design (i.e. modifying electrical or piezoelectric properties) within the langasite family [54, 55, 79-81] through cation substitutions and doping.

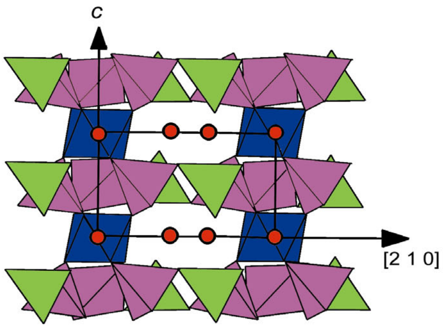

Cations	***Sites occupied***
La^{3+}	A
Ga^{3+}	B, C and half of D
Si^{4+}	Half of D

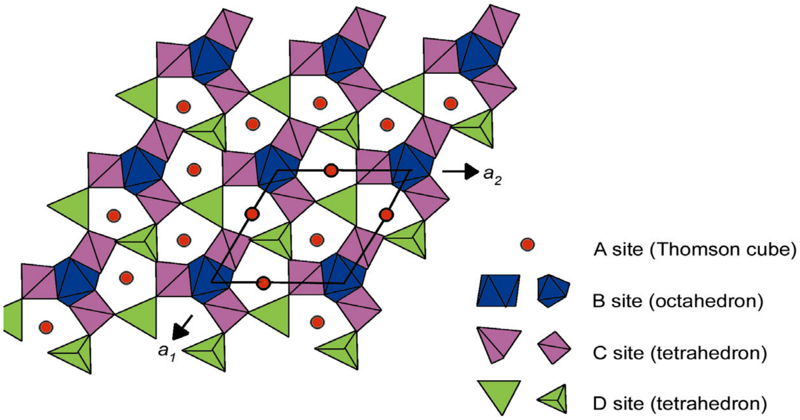

Figure 9: Crystal structure of langasite ($La_3Ga_5SiO_{14}$).

Growth of langasite single crystals has been investigated by several groups [78, 82-87]. The most successful and hence most common growth technique has been the Czochralski method, in which crystallization is initiated on a rotating seed crystal lowered into the melt followed by pulling from the melt. The growth atmosphere is usually Ar or N_2 with up to 5% O_2. The use of O_2 in the growth environment is reported to suppress Ga loss from the melt; however, too high a O_2 level can lead to Pt dissolution in the melt [78]. Crucibles used are often platinum (m.p. = 1769°C). Other materials tend to react with langasite during growth, leading to the incorporation of impurities [88, 89]. Coloration of langasite is also reported to be due to impurity incorporation [89], which may also have an influence on its electrical characteristics [90]. The growth of langasite is primarily along the Z-direction. Currently the 3-inch langasite boules produced commercially have growth rates of 1.5 to 5mm/hr. The quality of the crystals tends to improve as the growth rate is reduced.

1.4 BAW Resonant Sensor at High Temperature

1.4.1 BAW Resonator for Chemical Sensing

Nearly all current sensor designs deal with measurements at low or ambient temperatures, due either to operating limitations characteristic of the piezoelectric materials, and/or of the active films, typically polymers, which decompose at elevated temperatures. By utilizing langasite and a suitable active layer, we hope to design and implement a high temperature, high performance gas sensor.

Utilizing the resonator as a chemical sensor is a matter of selecting a suitable film which responds to the target chemical species. Typically, such a response is a change in mass, which can be accurately measured by the resonator. Alternatively, temperature responses produced during reactions between the film and the target chemical have also been used [91, 92]. In general, when acoustic resonators are used for mass measurement, the effects of temperature and stress must be eliminated or minimized. Hence it is important to maximize the sensitivity to mass and to minimize sensitivity to other perturbations. The mass sensitivity of a resonator is defined as [8, 20, 42]:

$$S_f = 2f^2 / (\rho_q v) \tag{25}$$

where f: resonant frequency, ρ_q: density of resonator, and v: velocity of shear wave. Note that percentage mass change must be less than 2% for Eq. (25) to be valid.

To maximize mass sensitivity, the most obvious way is to increase the resonant frequency of the resonator. In the case of bulk TSM acoustic resonators, this is done by reducing the resonator thickness (Eq. (2)). However, this also increases its response to other perturbations. Hence, the more acceptable approach is to increase the sensitivity of the active film towards the target chemicals.

In addition, minimization of cross sensitivity towards temperature and stress is important for a practical implementation of a resonator as a high temperature sensor. Stresses can be induced at the interface between the deposited film and the resonator, leading to resonance shifts. In general, for a uniform biaxial lateral stress of T_q in the resonator, the fractional frequency shift can be written as [45]:

$$\frac{\Delta f}{f} = KT_q \tag{26}$$

where K is a constant for a given crystallographic orientation.

Stress relaxation can occur between the resonator and its electrodes at high temperatures [93], which leads to changes in resonant frequency. In addition, the change in stoichiometry of active films, when exposed to changing temperatures and atmosphere, might lead to stresses large enough to affect the resonant frequency.

The effect of cross-sensitivity to temperature is significant since many applications at high temperature involve rapid temperature fluctuations. Several methods can be used to minimize the effect of temperature variations on sensor performance. The first is to find a temperature compensated cut (where $df/dT \approx 0$) for the temperature range in which the sensor will operate; for example, using AT-cut quartz resonator for near-room temperature applications. However, this only works if the operating temperature range is small. With a wide dynamic range, the temperature coefficient would likely be sufficiently large to mask the mass change.

An alternative method uses another identical resonator without the active film (the reference resonator) for compensation. To ensure proper operation, one must maintain both resonators under identical environments. It is therefore desirable to fashion both resonators on the same wafer – thereby providing physical proximity. This method also has the additional advantage of compensating out other spurious effects, such as stress change between the film and resonator, and temperature change due to heat of reaction (e.g. if the active film catalyzes gas phase reactions). However, if great care is not taken, temperature effects might not be compensated for completely due to large temperature gradients between sensor and reference.

More sophisticated compensation techniques are available. One that is often mentioned is the use of dual mode resonators, implemented with microcomputers [50, 94-98]. The basis of the technique is to utilize the difference in temperature coefficients of two resonant frequencies obtained with two modes of operation in a single resonator crystal. The two modes used can be, for example, the fundamental and the third harmonic, f_1 and f_3 respectively. In this case [50], given temperature coefficients of nth harmonic *(i.e.* f_n) be c_n and the frequency shift due to mass change be $\Delta f_{m,n}$, the total change in resonant frequency Δf_n (due to mass and temperature changes) is:

$$\Delta f_n = \Delta f_{m,n} + c_n \Delta T \tag{27}$$

A characteristic frequency, Δf_o, which is mass dependent and temperature independent can be defined as follow:

$$\begin{aligned}\Delta f_o(m) &= \Delta f_{n+2}(T,m) - \frac{c_{n+2}}{c_n}\Delta f_n(T,m) \\ &= \Delta f_{m,n+2}(m) - \frac{c_{n+2}}{c_n}\Delta f_{m,n}(m)\end{aligned} \tag{28}$$

Eq. (28) removes the need for a temperature sensor at the resonator, and provides excellent temperature-compensated measurements for sensing applications.

1.4.2 Active Films for Chemical Sensing

In our studies, we have identified and categorized films relying on mass change into three general types (Figure 10). Bulk based, relying on changes in stoichiometry of the entire film volume. Surface based, relying on adsorption of the target chemical onto the film. Here films are often selected to achieve quick recovery and high selectivity. Reaction based, relying on specific reaction pathways resulting in a reaction product between vapor and films with associated mass change.

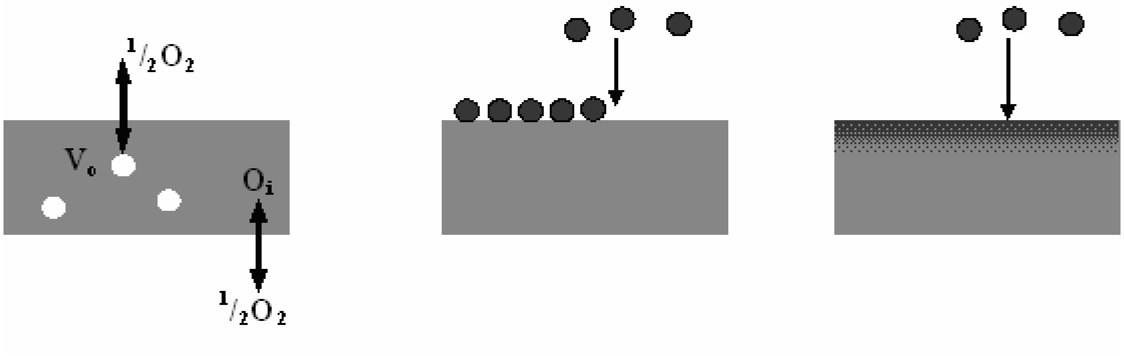

Figure 10: Three different operation modes of active films used in chemical sensing. Bulk based, surface based and reaction based films (left to right).

<u>Sensor utilizing bulk based film</u>

Oxide films exhibit oxygen non-stoichiometry which is sensitive to oxygen partial pressure variations [99-102]. Changing the oxygen partial pressure of the environment modifies the concentration of point defects within the film. For example, increasing oxygen partial pressure will increase the oxygen content of oxide, i.e. reducing the oxygen vacancy concentration or increasing the oxygen interstitial concentration, thereby changing the film mass . The mass change will have a power law dependence on oxygen partial pressure; depending on several factors (see 1.5.2 for details on defect chemistry).

Apart from using the bulk based film as part of an oxygen partial pressure resonant sensor, similar setups can be used for experimental determination of film mass change due to, for example, stoichiometry changes, ion intercalations, corrosion reactions, and film deposition. The film of interest can be deposited onto the resonator, and the mass change of the film can be measured via changes in resonant frequency. Therefore, the resonator essentially operates as a mass balance. Although quartz crystal microbalances are currently used in such capacities [43, 103-108] and even as a micro-thermal gravimetric analyzers (micro-TGA) [109], the use of a high temperature piezoelectric will markedly extend such measurements to include elevated temperatures. In earlier collaborative work, titanium oxide (TiO_2) thin films on langasite [48, 110] were investigated as the basis of a gas sensor. Dramatic resonant frequency changes were recorded when the resonator was subjected to a reducing environment at 600^{o}C. The ability to do such measurements on thin films is important, since materials in thin film and bulk form sometimes exhibit very different properties [111, 112].

In this thesis work, praseodymium-cerium oxide (PCO) was chosen as the active film for its oxygen partial pressure sensitivity given its highly non-stoichiometric nature at high oxygen partial pressures [113-115]. This allows us to evaluate a relatively large mass shift without interference from possible redox processes active in langasite at much more highly reducing conditions and temperatures, as demonstrated below in later sections.

Sensor utilizing surface based film

Surface active films have been used extensively for chemical sensing with acoustic devices for some time [1, 2, 6, 7, 9, 13, 41, 44, 92, 116-118]. Many of these sensing applications occur near room temperature.

One low temperature application we have examined that utilized surface based film is a chemical sensor based on AT-cut quartz resonator with SiO_2 active film. This sensor was fabricated for sensing a chemical agent simulant, dimethyl methylphosphonate (DMMP). DMMP is a simulant for the chemical agent, Sarin, and it readily adsorbs on the SiO_2 thin films. Chemical and biological weapons are a serious threat to national security and pose a potential danger to both civilians and military personnel. Sensors, sensitive to toxic biological and chemical agents, when deployed at strategic locations, can detect their release and thus minimize their impact. Sensors are also required for monitoring suspected chemical and biological production facilities. Due to the nature of their roles, such sensors need to be highly sensitive and selective, and resonant sensors are appropriate for these roles.

However, as this work was performed at relatively low temperature using only quartz resonator and therefore not directly related to the thesis, it is included only in Appendix A for reference and is not discussed in the main body of this thesis.

Sensor utilizing reaction based film

Reaction based films rely on chemical reactions between the chemical species and the active film for detection. One example is the corrosion of metal films [107, 119, 120]. In this thesis work, a reaction based film is used for detection of NO_2.

Diesel engines provide power to nearly every type of vehicle used in commerce, as well as to electrical power generating equipment. The diesel exhaust includes particulate matter (PM), oxides of nitrogen (NO_x), sulfur dioxide (SO_2) and various hydrocarbons. NO_x, which includes the nitrogen compounds (NO_2 and NO), plays an important role in atmospheric reactions that create harmful ground-level ozone (smog) and acid rain and is the focus of legislation, both in the US and Europe, which stipulates large reductions in emission levels beginning in 2007 [121]. In an effort to limit NO_x emissions for vehicles, the lean NO_x trap (LNT) has been proven to be promising.

The LNT system [122, 123] removes NO_x by storing NO_2 (NO in exhaust is preoxidized to NO_2 by Pt catalyst) in a compound containing an alkaline base metal (e.g. barium carbonate) as the nitrate (Figure 11). The *storage stage* occurs during lean burn operation of the diesel engine:

$$NO + \frac{1}{2} O_2 \rightarrow NO_2 \tag{29}$$

$$BaCO_3 + 2\,NO_2 + \frac{1}{2} O_2 \rightarrow Ba(NO_3)_2 + CO_2 \tag{30}$$

When the storage site is saturated, the engine switches briefly to rich burn operation. The NO_2 is then released and reduced by the excess hydrocarbons and carbon monoxide in the presence of a Pt catalyst into N_2, H_2O, and CO_2. This is known as the *purge stage*:

$$Ba(NO_3)_2 \rightarrow BaO + 2\ NO_2 + \tfrac{1}{2}\ O_2 \qquad (31)$$

$$BaO + CO_2 \rightarrow BaCO_3 \qquad (32)$$

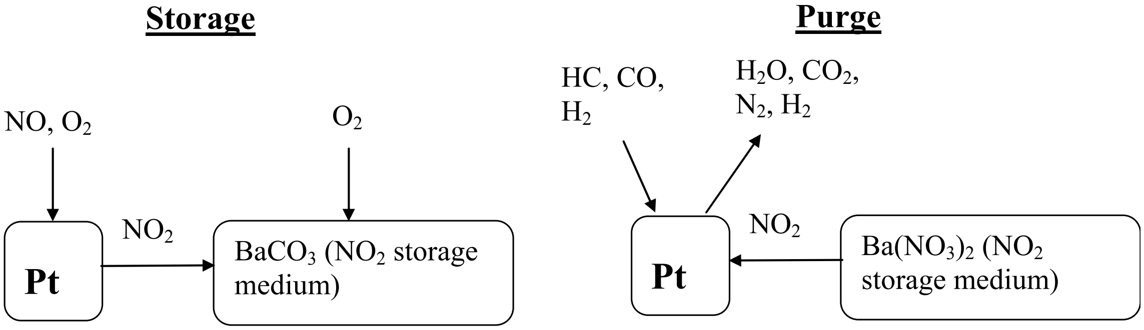

Figure 11: LNT Storage and Purge mechanism.

For LNT, NO_2 storage capacity needs to be monitored in order to maximize fuel efficiency. It is undesirable for the engine to prematurely switch to the rich burn mode or to remain excessively long in the rich burn mode resulting in reduced fuel economy. Hence, for optimum functioning of LNT, rapid and effective feedback is necessary and a monitor is needed to determine when the storage sites are saturated during lean burn, and when they are fully purged during rich burn.

In this thesis, the langasite-based resonant sensor system will be configured for monitoring NO_2 concentration levels in a given atmosphere. Typical diesel operating conditions can reach temperature as high as 700-800°C (although 250-300°C is typical), making langasite resonators an excellent choice. The reaction based active film is $BaCO_3$ which is converted to $Ba(NO_3)_2$ in the presence of NO_2 (Eq. (30)) with a large associated mass change. However, since the reaction product is stable under lean burn condition, the frequency shift is irreversible in this instant; the sensor will act as a NO_2 concentration integrator. The film will only be regenerated when the engine is switched to rich burn, converting $Ba(NO_3)_2$ back to $BaCO_3$ (Eq. (31) and (32)).

1.4.3 Requirements for Resonator and Active Film at High Temperature

For operating at extreme conditions, additional requirements for the piezoelectric resonator are:

1. Chemical stability – the resonator has to be chemically inert in the operating environment (e.g. no phase transformation, irreversible mass loss). Lack of reactions between the electrode-film-resonator is important as well.
2. Negligible mass change – reducing and oxidizing environments can change the oxygen stoichiometry of an oxide piezoelectric material, such as langasite. The proper operation of the resonator must occur in the pO_2 range for which negligible oxidation and reduction of the resonator material takes place.
3. Low electrical losses – this requirement has been discussed in 1.2.3 and the repercussion of high loss can be seen in Figure 8. The resultant low Q values adversely affect the resolution and signal-to-noise ratio of the resonant signals.

Defect chemistry will provide us the ability to modify langasite properties to achieve the optimum performance in term of stability, negligible mass change and low loss.

For active films of chemical sensors, in addition to chemical and structural stability at high temperatures, there are other requirements for achieving high sensitivity, and, depending on what type of film is used, these requirements are:

1. For bulk-based films, a significant stoichiometry change at the target oxygen partial pressure range and temperatures.
2. For surface-based films, a large number of selective adsorption sites (e.g. high surface area).
3. For reaction-based films, a significant associated mass change with the reaction.

Generally, the kinetics of any of interactions between the film and target chemicals should be rapid, together with fast recovery with the removal of the chemicals. Cross sensitivity to other chemicals should be limited, i.e. high selectivity, and long term stability is desirable.

1.5 Defect Chemistry and Model

1.5.1 Introduction

The aim of defect analysis is to create a model based on analyzed raw electrical, mass transport and stoichiometry data of a material that describes the sources of electrical conductivity, diffusion, nonstoichiometry, etc, and identifies the dominant mechanisms over a wide range of temperatures and pO_2 [100, 124-134]. Using an accurate defect model allows systematic enhancement of the electrical and transport properties of the material through cation substitution (doping), as well as prediction of stable operating conditions. Defect analysis is important to understand the mechanisms of resistive losses and their dependence on temperatures and pO_2, the kinetics of various transport pathways, and to identify the stability regime of langasite-related materials. The latter two are important to ensure that langasite continues to be a stable platform for mass measurements. With the defect model in place, we will optimize langasite for low loss (i.e. high resistivity) and stability at high temperatures by cation substitution. In this regard, langasite is particularly accommodating since nearly every size cation can be accommodated on one of its four different cation sites [54]. Cation substitutions have already been successfully applied in langasite to modify its electromechanical properties (e.g. piezoelectric constants, acoustic velocity and Q-values) [54, 56, 79-82, 135-140].

1.5.2 Theory

The defect chemical approach, which assumes dilute solutions, requires one to select the key defect reactions incorporating the dominant electronic and ionic defects. These normally include oxidation/reduction, intrinsic lattice defect generation, intrinsic electron-hole generation, and ionization reactions as well as overall charge and mass balance relations. The reaction equations (that are commonly occuring for oxide semiconducting materials) and their respective mass action laws[1] are listed below [141-143]:

---

[1] The unit for defect concentration and pO_2 used throughout this work would be cm^{-3} and atm respectively. This makes the dimensions of k_s be cm^{-69}, k_F be cm^{-6}, k_e be cm^{-6}, k_r be $cm^{-9}atm^{0.5}$, and k_o be $cm^{-3}atm^{-0.5}$.

Schottky Reaction

$$null \rightarrow 14V_{O}^{\bullet\bullet} + 3V_{La}^{'''} + 5V_{Ga}^{'''} + V_{Si}^{''''} \tag{33}$$

$$K_{s} = \left[V_{O}^{\bullet\bullet}\right]^{14}\left[V_{La}^{'''}\right]^{3}\left[V_{Ga}^{'''}\right]^{5}\left[V_{Si}^{''''}\right] = k_{s}\exp\left(\frac{-E_{s}}{kT}\right) \tag{34}$$

Anion Frenkel Reaction

$$O_{O}^{X} \rightarrow V_{O}^{\bullet\bullet} + O_{i}^{''} \tag{35}$$

$$K_{F} = \left[V_{O}^{\bullet\bullet}\right]\left[O_{i}^{''}\right] = k_{F}\exp\left(\frac{-E_{F}}{kT}\right) \tag{36}$$

Generation Reaction

$$null \rightarrow h^{\bullet} + e^{'} \tag{37}$$

$$K_{e} = np = k_{e}\exp\left(\frac{-E_{g}}{kT}\right) \tag{38}$$

Reduction Reaction

$$O_{O}^{X} \rightarrow V_{O}^{\bullet\bullet} + 2e^{'} + \tfrac{1}{2}O_{2} \tag{39}$$

$$K_{r} = \left[V_{O}^{\bullet\bullet}\right]n^{2}\,pO_{2}^{\frac{1}{2}} = k_{r}\exp\left(\frac{-E_{r}}{kT}\right) \tag{40}$$

Oxidation Reaction

$$\tfrac{1}{2}O_{2} + V_{o}^{\bullet\bullet} \rightarrow O_{o}^{x} + 2h^{\bullet} \tag{41}$$

$$K_{O} = p^{2}\left[V_{o}^{\bullet\bullet}\right]^{-1}pO_{2}^{-\frac{1}{2}} = k_{O}\exp\left(\frac{-E_{O}}{kT}\right) \tag{42}$$

For either acceptor or donor doped material, an additional ionization equation for the dopant can be written[2]. For acceptor doped material, the ionization equation, together with its mass action law, will be:

$$A \rightarrow A_c^{'} + h^{\bullet} \tag{43}$$

$$K_{Ac} = \left[A_c^{'}\right]p = k_{Ac}\exp\left(\frac{-E_{A\_ion}}{kT}\right) \tag{44}$$

And for donor doped material, they are:

$$D \rightarrow D_c^{\bullet} + e^{'} \tag{45}$$

$$K_{Dn} = \left[D_c^{\bullet}\right]n = k_{Dn}\exp\left(\frac{-E_{D\_ion}}{kT}\right) \tag{46}$$

In addition, for all the charged species, a general electrical neutrality equation incorporating all the defect species mentioned above can be written as (assuming Anion Frenkel dominates):

$$n + 2\left[O_i^{''}\right] + \left[A_C^{'}\right] = p + 2\left[V_O^{\bullet\bullet}\right] + \left[D_C^{\bullet}\right] \tag{47}$$

By solving the appropriate equations above, it would be possible to determine the concentration of electrical species present at a given temperature, oxygen partial pressure and dopant level. It is then possible to predict the electrical conductivity of the material in conjunction with mobility information of the electrical species.

However, simultaneously solving the above set of equations is normally difficult and so the so-called Brouwer approximation is often applied, in which the neutrality and mass balance equations are simplified to include only one defect species on either side of the equality over restricted ranges of pO_2 and temperature [141-143]. The defect regions are defined by a dominant defect chemical reaction over restricted ranges of pO_2 and temperatures. Commonly, for acceptor and donor-doped materials, four defect regions

---

[2] The dimensions of k_{Ac} and k_{Dn} are both cm^{-6}.

can be defined: reduction, ionic compensation, electronic compensation, and oxidation regions. In each region, the neutrality equation, Eq. (47), can be simplified as shown below:

Reduction

$$n \approx 2\left[V_O^{\bullet\bullet}\right] \tag{48}$$

Ionic Compensation

$$\textit{Acceptor:}\ 2\left[V_O^{\bullet\bullet}\right] \approx \left[A_c^{'}\right] \tag{49}$$

$$\textit{Donor:}\ 2\left[O_i^{''}\right] \approx \left[D_c^{\bullet}\right] \tag{50}$$

Electronic Compensation

$$\textit{Acceptor:}\ p \approx \left[A_c^{'}\right] \tag{51}$$

$$\textit{Donor:}\ n \approx \left[D_c^{\bullet}\right] \tag{52}$$

Oxidation

$$p \approx 2\left[O_i^{''}\right] \tag{53}$$

By applying the above approximations, it allows us to characterize the oxygen partial pressure and temperature dependence of the electrical species; which is key in analyzing raw electrical data in term of defect chemistry. For example, in acceptor doped material, the approximation for the reduction reaction dominant region, Eq. (48), can be substituted into Eq. (40), giving:

$$n = 2^{\frac{1}{3}} pO_2^{-\frac{1}{6}} k_r^{\frac{1}{3}} \exp\left(\frac{-E_r}{3kT}\right) \tag{54}$$

Eq. (54) tells us two crucial pieces of information. First, the electrical conductivity at the reduction dominant region will have a $pO_2^{-\frac{1}{6}}$ dependence due to electron (i.e. electronic conductivity instead of ionic), and, secondly, the activation energy obtained from the

Arrhenius plot of electrical conductivity at that region will give us $^1/_3$ of the reduction enthalpy, plus a mobility activation energy (if the conduction mechanism is activated hopping).

To continue to obtain similar equations for other electrical species in this reduction dominant region, the following analysis is performed:

Substituting Eq. (54) into Eq. (38), the oxygen partial pressure dependence for holes is:

$$p = 2^{-\frac{1}{3}} pO_2^{+\frac{1}{6}} k_r^{-\frac{1}{3}} k_e \exp\left(-\frac{\left(E_g - \frac{1}{3}E_r\right)}{kT} \right) \tag{55}$$

Substituting Eq. (48) into Eq. (54), the oxygen partial pressure dependence for oxygen vacancies is:

$$\left[V_O^{\bullet\bullet}\right] = 2^{-\frac{2}{3}} pO_2^{-\frac{1}{6}} k_r^{\frac{1}{3}} \exp\left(\frac{-E_r}{3kT} \right) \tag{56}$$

Substituting Eq. (56) into Eq. (36), the oxygen partial pressure dependence for oxygen interstitials is:

$$\left[O_i''\right] = 2^{\frac{2}{3}} pO_2^{+\frac{1}{6}} k_r^{-\frac{1}{3}} k_F \exp\left(-\frac{\left(E_F - \frac{1}{3}E_r\right)}{kT} \right) \tag{57}$$

Similar analyses can be done for the three other regions, and the results are summarized in Table 3. The equations in the table give the pO_2 dependence of the electrical species, and the enthalpy associated with their generation in a particular defect region.

Table 3: Equations for defect species concentration in acceptor doped material.

Electrical Carrier	Region I $n \approx 2\left[V_O^{\bullet\bullet}\right]$	Region II $2\left[V_O^{\bullet\bullet}\right] \approx \left[A_c^{'}\right]$	Region III $p \approx \left[A_c^{'}\right]$	Region IV $p \approx 2\left[O_i^{''}\right]$
n	$2^{\frac{1}{3}} pO_2^{-\frac{1}{6}} k_r^{\frac{1}{3}} \exp\left(\frac{-E_r}{3kT}\right)$	$2^{\frac{1}{2}} \left[A_c^{'}\right]^{-\frac{1}{2}} pO_2^{-\frac{1}{4}} k_r^{\frac{1}{2}} \exp\left(-\frac{E_r}{2kT}\right)$	$\left[A_c^{'}\right]^{-1} k_e \exp\left(-\frac{E_g}{kT}\right)$	$2^{-\frac{1}{3}} pO_2^{-\frac{1}{6}} k_F^{-\frac{1}{3}} k_o^{-\frac{1}{3}} k_e \exp\left(\frac{\left(E_0 + E_F - 3E_g\right)}{3kT}\right)$
p	$2^{-\frac{1}{3}} pO_2^{\frac{1}{6}} k_r^{-\frac{1}{3}} k_e \exp\left(-\frac{\left(E_g - \frac{1}{3}E_r\right)}{kT}\right)$	$2^{-\frac{1}{2}} \left[A_c^{'}\right]^{\frac{1}{2}} pO_2^{\frac{1}{4}} k_r^{-\frac{1}{2}} k_e \exp\left(-\frac{\left(E_g - \frac{1}{2}E_r\right)}{kT}\right)$	$\left[A_c^{'}\right]$	$2^{\frac{1}{3}} pO_2^{\frac{1}{6}} k_F^{\frac{1}{3}} k_o^{\frac{1}{3}} \exp\left(-\frac{\left(E_o + E_F\right)}{3kT}\right)$
$\left[V_O^{\bullet\bullet}\right]$	$2^{-\frac{2}{3}} pO_2^{-\frac{1}{6}} k_r^{\frac{1}{3}} \exp\left(\frac{-E_r}{3kT}\right)$	$\frac{1}{2}\left[A_c^{'}\right]$	$\left[A_c^{'}\right]^2 pO_2^{-\frac{1}{2}} k_r k_e^{-2} \exp\left(-\frac{\left(E_r - 2E_g\right)}{kT}\right)$	$2^{\frac{2}{3}} pO_2^{-\frac{1}{6}} k_o^{-\frac{1}{3}} k_F^{\frac{2}{3}} \exp\left(-\frac{\left(2E_F - E_o\right)}{3kT}\right)$
$\left[O_i^{''}\right]$	$2^{\frac{2}{3}} pO_2^{\frac{1}{6}} k_r^{-\frac{1}{3}} k_F \exp\left(-\frac{\left(E_F - \frac{1}{3}E_r\right)}{kT}\right)$	$2\left[A_c^{'}\right]^{-1} k_F \exp\left(-\frac{E_F}{kT}\right)$	$\left[A_c^{'}\right]^{-2} pO_2^{\frac{1}{2}} k_o k_F \exp\left(-\frac{E_o + E_F}{kT}\right)$	$2^{-\frac{2}{3}} pO_2^{\frac{1}{6}} k_F^{\frac{1}{3}} k_o^{\frac{1}{3}} \exp\left(-\frac{\left(E_o + E_F\right)}{3kT}\right)$

In addition, a Kroger-Vink diagram (Figure 12) can be drawn for the acceptor doped material after solving for all 4 regions, showing the oxygen partial dependence and relative carrier density of various electrical species. Note that the acceptor concentration represents the ionized acceptor concentration.

From the Kroger-Vink diagram for acceptor doped material (Figure 12), it can be observed that, for example, in Region I, electrons and oxygen vacancies are the dominant defects. Region I, however, is likely to have purely electronic conduction since the mobility of electrons is usually orders of magnitude higher than that of oxygen vacancies. In Region II, oxygen vacancies begin to dominate as the electron density decreases with increasing pO_2. In Region III, holes become the dominant charge carriers, and this likely carries into Region IV, since the mobility of holes is generally much higher than that of oxygen interstitials.

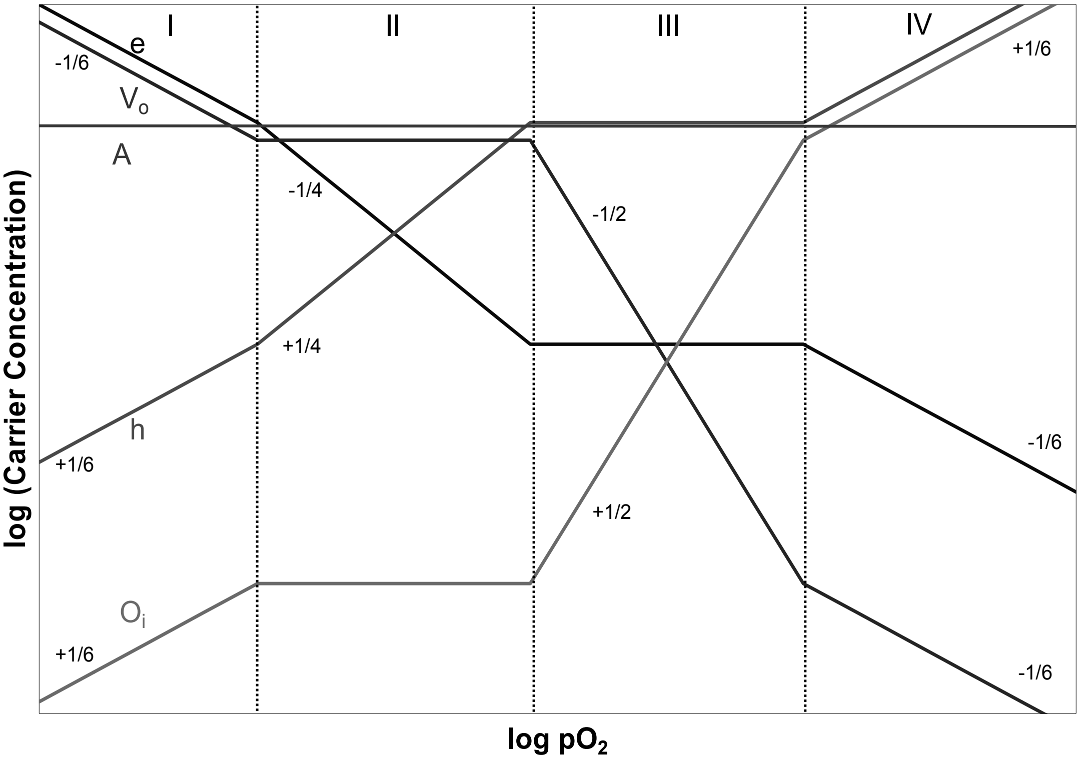

Figure 12: Kroger-Vink diagram for acceptor doped material.

For donor doped material, the oxygen partial pressure dependence is summarized in Table 4, and its Kroger-Vink diagram is shown in Figure 13. Similarly, the donor concentration in the Kroger-Vink diagram represents the ionized donor concentration.

Similar to the acceptor doped case, for donor doped materials in Region I (see Figure 13), the electron is expected to be the dominant electrical carrier with a $pO_2^{-\frac{1}{6}}$-dependence. Region II would be pO_2 independent with the electron density fixed by the concentration of ionized donors. As the pO_2 increases further, progressing to Region III, the electrical conductivity could switch to ionic towards the middle of this region if the intrinsic electron-hole product becomes low enough. At sufficiently high pO_2, increasing numbers of holes will again shift the balance to electronic conduction. In Region IV, the material is expected to be dominated by hole conduction but now with a $pO_2^{1/6}$ dependence.

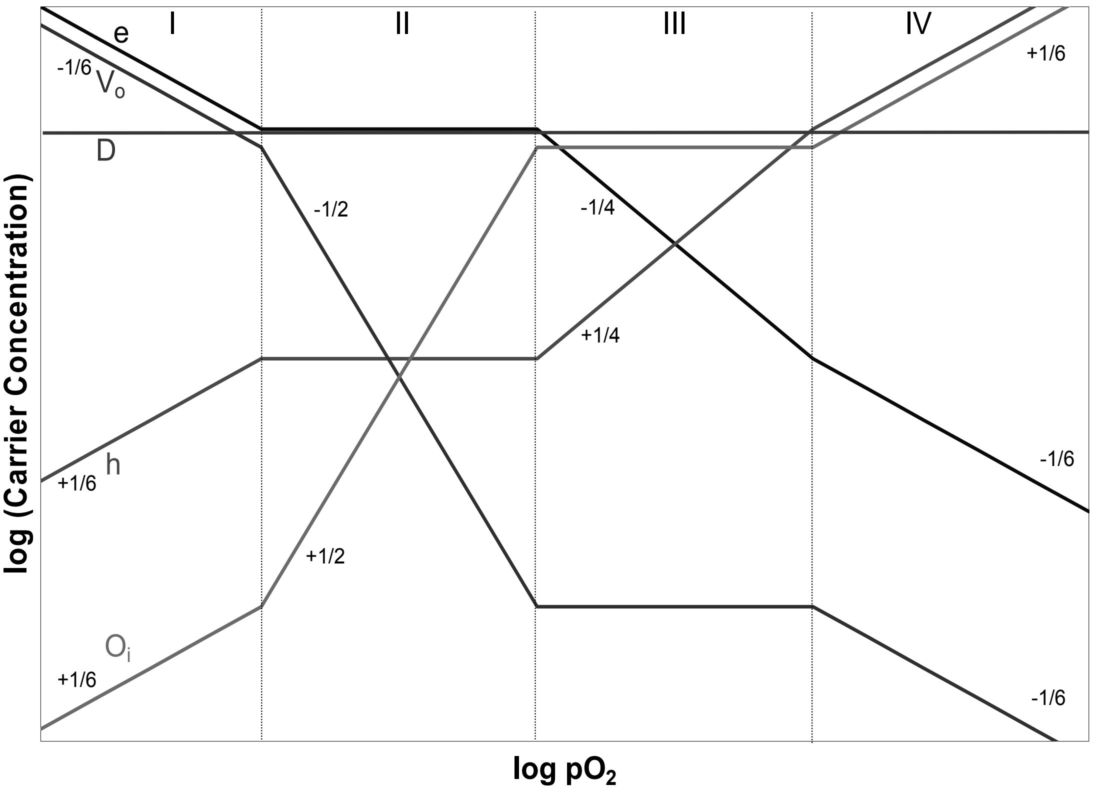

Figure 13: Kroger-Vink diagram for donor doped material.

Table 4: Equations for defect species concentration in donor doped material.

Electrical Carrier	Region I $n \approx 2\left[V_O^{\bullet\bullet}\right]$	Region II $n \approx \left[D_c^{\bullet}\right]$	Region III $2\left[O_i^{''}\right] \approx \left[D_c^{\bullet}\right]$	Region IV $p \approx 2\left[O_i^{''}\right]$
n	$2^{\frac{1}{3}} pO_2^{-\frac{1}{6}} k_r^{\frac{1}{3}} \exp\left(\frac{-E_r}{3kT}\right)$	$\left[D_c^{\bullet}\right]$	$2^{\frac{1}{2}} \left[D_c^{\bullet}\right]^{-\frac{1}{2}} pO_2^{-\frac{1}{4}} k_r^{\frac{1}{2}} k_F^{\frac{1}{2}} \exp\left(-\frac{(E_r + E_F)}{2kT}\right)$	$2^{\frac{1}{3}} pO_2^{-\frac{1}{6}} k_o^{-\frac{1}{3}} k_e \exp\left(-\frac{\left(E_g - \frac{1}{3}E_o\right)}{kT}\right)$
p	$2^{-\frac{1}{3}} pO_2^{+\frac{1}{6}} k_r^{-\frac{1}{3}} k_e \exp\left(-\frac{\left(E_g - \frac{1}{3}E_r\right)}{kT}\right)$	$\left[D_c^{\bullet}\right]^{-1} k_e \exp\left(-\frac{E_g}{kT}\right)$	$2^{-\frac{1}{2}} \left[D_c^{\bullet}\right]^{\frac{1}{2}} pO_2^{\frac{1}{4}} k_r^{-\frac{1}{2}} k_F^{-\frac{1}{2}} k_e \exp\left(\frac{(E_r + E_F - 2E_g)}{2kT}\right)$	$2^{-\frac{1}{3}} pO_2^{\frac{1}{6}} k_o^{\frac{1}{3}} \exp\left(-\frac{E_o}{3kT}\right)$
$\left[V_O^{\bullet\bullet}\right]$	$2^{-\frac{2}{3}} pO_2^{-\frac{1}{6}} k_r^{\frac{1}{3}} \exp\left(\frac{-E_r}{3kT}\right)$	$\left[D_c^{\bullet}\right]^{-2} pO_2^{-\frac{1}{2}} k_r \exp\left(-\frac{E_r}{kT}\right)$	$2\left[D_c^{\bullet}\right]^{-1} k_F \exp\left(-\frac{E_F}{kT}\right)$	$2^{\frac{2}{3}} pO_2^{-\frac{1}{6}} k_o^{-\frac{1}{3}} k_F^{\frac{2}{3}} \exp\left(-\frac{(2E_F - E_o)}{3kT}\right)$
$\left[O_i^{''}\right]$	$2^{\frac{2}{3}} pO_2^{+\frac{1}{6}} k_r^{-\frac{1}{3}} k_F \exp\left(-\frac{\left(E_F - \frac{1}{3}E_r\right)}{kT}\right)$	$\left[D_c^{\bullet}\right]^{2} pO_2^{\frac{1}{2}} k_r^{-1} k_F \exp\left(-\frac{(E_F - E_r)}{kT}\right)$	$\frac{1}{2}\left[D_c^{\bullet}\right]$	$2^{-\frac{2}{3}} pO_2^{\frac{1}{6}} k_o^{\frac{1}{3}} k_F^{\frac{1}{3}} \exp\left(-\frac{(E_F + E_o)}{3kT}\right)$

1.5.3 Application of Defect Chemistry and Model

To apply defect analysis to a material, its total bulk electrical conductivity needs to be collected over a range of temperatures and oxygen partial pressures. The total conductivity of a material is a summation of contributions by all electrically charged species, i.e.:

$$\sigma_{total} = \sum_i qZ_i c_i \mu_i \tag{58}$$

where q is the elemental charge, Z is the valence, c is the concentration, and μ is the mobility of the species.

The bulk conductivity data at each temperature are plotted as function of pO_2. The plot gives information about the defect region that the material is in. Relying on Table 3 or Table 4 for acceptor or donor doped material respectively, the pO_2-dependence of the electrical conductivity across the pO_2 range allows us to establish the possible defect chemical reactions that are dominant under those conditions, and hence establish which electrical species dominate. In addition, the activation energy of the bulk electrical conductivity acquires physical meaning, as it can then be related to specific defect reactions (after accounting for the mobility activation energy).

However, to solve the defect equations presented in Table 3 or Table 4 so as to establish a predictive defect model for a material, the mobility must be known. For ionic species, the process for determining the mobility is through systematic acceptor or donor doping. In the ionic compensation region (Eq. (49) and (50), p.49), the oxygen vacancies or interstitials are fixed at the ionized acceptor or donor level respectively. With known dopant level, the mobility can then be extracted from the bulk conductivity data (see Eq. (58))[3].

---

[3] This is assuming that there is no association between defects (e.g. between ionized acceptors and oxygen vacancies). Effect of defect association is discussed in the Discussion section.

For electronic species, their concentration and type (hole or electron) can be determined using thermoelectric power (TEP) measurements. By combining the bulk conductivity and TEP data, the electron or hole mobility can be extracted. In TEP measurement (also know as the Seebeck measurement), a temperature gradient is created across the sample. The dominant electronic species will migrate from the hot end where they have higher kinetic energy to the cool end. The resultant voltage and polarity at the cold end can be measured and correlated to the electronic species concentration. In the case of electrons being the majority carrier, negative voltage will be measured at the cold end. The voltage measurements are repeated for different temperature gradients at a certain temperature, and *dV* versus *dT* can be plotted. The slope of *dV* versus *dT* will then be the TEP or the Seebeck coefficient, *Q*, at that temperature:

$$Q = \frac{dV}{dT} \tag{59}$$

The electron density, *n*, can be calculated from the TEP, assuming it is the majority carriers, by [141]:

$$Q = -\frac{k}{e}\left[\ln\frac{N_C}{n} + \frac{H_e^*}{kT}\right] \tag{60}$$

Alternatively, the hole density, *p*, can be calculated from the TEP, assuming it is the majority carriers, by:

$$Q = \frac{k}{e}\left[\ln\frac{N_V}{p} + \frac{H_e^*}{kT}\right] \tag{61}$$

In the case where neither electrons nor holes are dominant and, therefore, both contribute to the electrical conductivity, the Seebeck coefficient is defined as:

$$Q = \frac{n\mu_e Q_e + p\mu_h Q_h}{n\mu_e + p\mu_h} \tag{62}$$

In semiconducting oxides, the heat of transport, *H**, is typically small and is usually neglected [134].

For a case where electron is the majority carrier, with its concentration derived from TEP and conductivity from impedance measurements, the electron mobility can be calculated using Eq. (58). TEP can also serve as an alternative method to impedance measurements for checking the pO_2-dependence of the concentration of electronic species, allowing for independent verification of the model.

Concentration cell measurements allow the determination of ionic species contribution to the total conductivity, and thereby provide a further mean for verifying the defect model. The fractional ionic, electron and hole contributions to the total electrical conductivity are defined by their respective transference number, t_i, t_e and t_h as:

$$t_i = \frac{\sigma_i}{\sigma_{total}}; t_e = \frac{\sigma_e}{\sigma_{total}}; t_h = \frac{\sigma_h}{\sigma_{total}} \tag{63}$$

Concentration cell measurements are used for determining ionic transference numbers. The open circuit voltage, V, measured across a specimen, with one side kept at a reference (e.g. air) while the other is exposed to a varying oxygen partial pressure. The average ionic transference number, t_i, is related to V by:

$$V = \bar{t}_i \frac{kT}{4q} \ln \frac{pO_2}{pO_{2,air}} \tag{64}$$

When t_i is unity, the voltage, V, is simply the Nernst potential [143].

To obtain a precise t_i at a specific oxygen partial pressure, a differential form of the above equation can to be used [144]:

$$\left| \frac{dV}{d(\ln pO_2)} \right|_{pO_2} = t_i(pO_2)\frac{kT}{4q} \tag{65}$$

In order that the first derivative can be taken from a V versus pO_2 plot, an equation that relates V to pO_2 is needed [144]:

$$V = \frac{kT}{q}\left\{ \ln\left[\frac{P_p^{\frac{1}{4}} + \left(pO_2^{I}\right)^{\frac{1}{4}}}{P_p^{\frac{1}{4}} + \left(pO_2^{II}\right)^{\frac{1}{4}}} \right] + \ln\left[\frac{P_n^{\frac{1}{4}} + \left(pO_2^{II}\right)^{\frac{1}{4}}}{P_n^{\frac{1}{4}} + \left(pO_2^{I}\right)^{\frac{1}{4}}} \right] \right\} \tag{66}$$

where P_p and P_n are the pO_2's at which the electronic transference numbers of holes and electrons are 0.5 respectively, pO_2^I is the reference pO_2, and pO_2^{II} is the working pO_2. By fitting Eq. (66) to the V versus pO_2 plot, and taking the first derivative of the fitted equation with respective to log pO_2, the precise ionic transport number (t_i) can be obtained (Eq. (65)).

Chapter 2: Objectives

2.1 Langasite Transport Properties and Stability Limits

In order to utilize langasite as a piezoelectric for a viable bulk acoustic wave resonator at high temperatures, it is necessary to understand its electrical properties (with contributions from both ionic and electronic species) and ionic transport properties. To achieve this aim, we will measure its bulk electrical properties using impedance spectroscopy, in conjunction with thermoelectric power and concentration cell measurements to distinguish between ionic and electronic contributions. Diffusion studies, performed with collaborators, will allow us to obtain further information about ionic transport properties of langasite. With data from these studies, it will be possible to predict the electrical and defect properties, and subsequently, be able to minimize resistive losses and assist in the derivation of the stability regime of langasite at high temperatures.

2.2 Langasite BAW Resonant Chemical Sensor

For applying the langasite resonator platform together with a sensitive film as a chemical sensor, not only must the langasite resonator be stable and its loss kept to a minimum, but the sensitive film must exhibit significant mass change associated with exposure to the target chemicals. Hence, we will evaluate the sensitivity of films to target chemicals, using quartz for test of concept since the result can be transferred readily to langasite resonators for more extreme conditions.

In the sensor application studies, we focused on two applications that demonstrated high temperature resonant sensor applications, namely:

1. Detection of oxygen partial pressure change due to oxygen stoichiometry change in oxide materials, as an example of a bulk-based film.
2. Detection of NO_x through reaction with $BaCO_3$ film, as an example of a reaction-based film.

We also seek to understand the processes that control sensitivity and response time, and will attempt to improve them through optimization of microstructures and addition of catalyst.

Chapter 3: Experimental

3.1 General

In this chapter, we describe the experimental procedures used in our work. Experiments were designed in order to achieve the stated objectives in Chapter 2, and they can be classified into two areas: (a) transport property measurements, and (b) high temperature sensor applications. In both areas, sample/device preparations, sample/device setup, and data acquisition equipment and techniques are described.

3.2 Transport Properties of Langasite

3.2.1 Sample Preparations

Because single crystal langasite was found [145] to exhibit slow reduction-oxidation kinetics, even at elevated temperatures, we utilized polycrystalline specimens with interconnected porosity in this study to examine equilibrium electrical and defect properties. Polycrystalline undoped, 1%Sr-doped and 5%Nb-doped langasite samples were produced using the mixed oxide route. Sr and Nb were chosen as an acceptor and donor respectively, because they have been known to form solid solutions with or completely substituting a cation in materials with the langasite-type structure [54, 82, 135-137, 140]. Since the cation sites they substituted into are known (i.e. Sr replaces La, and Nb replaces Ga), the dopant behaviors are more predictable. The amount of dopant required was calculated as molecular percentage of the targeted cation site[4], instead of total weight percentage of langasite (which would be different, see Table 5).

Table 5: Amount of acceptor and donor in mol% and wt%.

Dopant	Mol %	Wt % of Langasite
Sr	1 mol% of La	0.4 wt%
Nb	5 mol% of Ga	2.2 wt%

---

[4] This definition is used in this thesis unless otherwise stated.

Stoichiometric amounts of La_2O_3, Ga_2O_3, SiO_2, $Sr(CO_3)$ (for 1%Sr doped) and Nb_2O_5 (for 5%Nb doped) powders (Alfa Aesar, 99.99% metal basis) were mixed and ball-milled in deionized water for approximately 24hrs. The mixture was then dried at 110^oC while stirred, and then uniaxially pressed into 1" pellets. The pellets were calcined at 950^oC for 3 hours and then sintered at 1450^oC for 10 hours. The pellets were placed on powder beds (with composition identical to the pellets') to prevent reactions with the alumina sintering dishes used.

Density achieved for undoped langasite was greater than 94% and for both the doped samples was greater than 90%. In all cases, grain sizes on the order of 10 μm were obtained. X-ray diffraction showed the material to be langasite with no observable second phases. Previous attempts where sintering steps were performed at 1200^oC or lower showed the formation of $LaGaO_3$ as a second phase.

3.2.2 Two-point Impedance Spectroscopy Measurements

Pellets of nominally undoped, 5%Nb-doped and 1%Sr-doped langasite were cut into bars with effective cross sectional area of 6.5-7.0mm^2 and length of 5.5-6.5mm. The bars were electroded with platinum using platinum ink paint from Engelhard-Clal and then cured at 850^oC for 3 hours. AC complex impedance measurements were conducted using a frequency response analyzer (Solartron 1260). Samples were heated in a tube furnace (Thermolyne 21100 Tube Furnace) to temperatures of 700-1000^oC (controlled using Eurotherm 818 programmable controller) with the oxygen partial pressure controlled with Ar/O_2 (for high pO_2 range) or CO/CO_2 (for low pO_2 range) gas mixtures. The schematic of the experimental setup is shown in Figure 14. Samples were allowed to equilibrate from a day (at 700^oC) to 2hr (at 1000^oC).

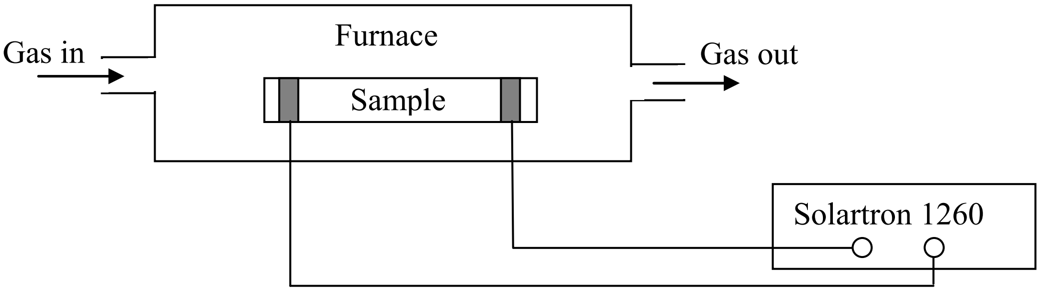

Figure 14: Experimental setup for two-point impedance measurements.

A polycrystalline material has, in general, 3 different contributions to its total resistance: the bulk, the grain boundaries, and the electrodes/contacts. When 2-point impedance measurements are performed, three semicircles appear on the impedance plot under ideal conditions for which the different time constants of each contribution are sufficiently distinct (Figure 15).

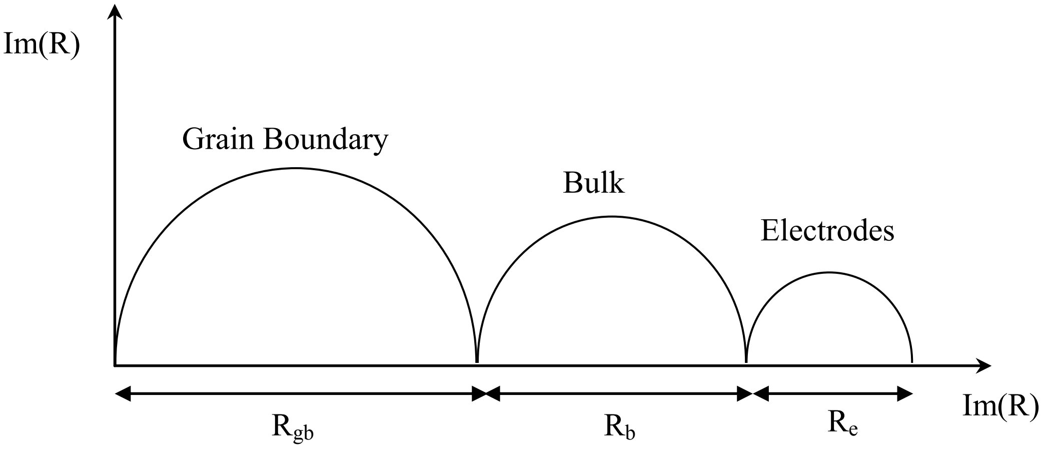

Figure 15: Idealized impedance plot for a polycrystalline material.

The electrical conductivity at a certain temperature and pO_2 is then analyzed by fitting the corresponding impedance spectrum (using Zview software program, Scribner Associates Inc., Version 2.0) with an equivalent circuit that contains parallel R-C elements, one each for electrodes, grain boundary and bulk (Figure 16). The resistance contribution from each contribution can then be extracted from the diameter of the corresponding semicircle. The conductivity is then calculated by normalizing by the bulk geometry even for the interfacial contributions. This allows one to continue to compare the relative contributions in a log conductivity versus reciprocal temperature plot. Note, in this study, only the bulk component of the conductivity is examined in any detail. The extracted bulk electrical conductivities at different temperatures for all three samples were plotted as function of pO_2 for further analysis. Tests for reversibility were performed after measurements at low pO_2 by repeating the measurements at higher pO_2.

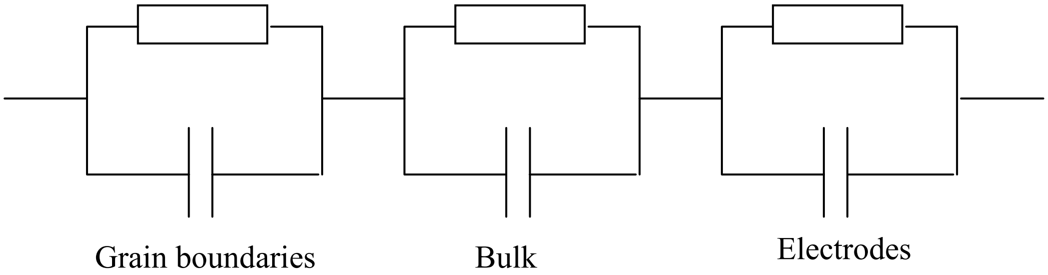

Figure 16: Equivalent circuit modeling R-C contributions from electrodes, grain boundaries and bulk.

3.2.3 Thermoelectric Power Measurements

Thermoelectric power (TEP) measurements were performed on polycrystalline 5%-Nb doped langasite to confirm the sign and concentration of its majority carrier. It also served to independently verify the prediction made by the defect model that electrons rather than ions were the dominant carriers. In addition, with the determination of the majority carrier density, it became possible to determine the carrier mobility.

A 12mm long of 5%-Nb doped langasite sample, in the shape of a parallelepiped, was cut from the pellet used for impedance measurements. Pt wires, together with a pair of type-S thermocouples, were attached to each end. The schematic of the experimental setup is shown in Figure 17. Samples were heated in a tube furnace (Thermolyne 21100 Tube Furnace) to temperatures of 700-1000^{o}C (controlled using Eurotherm 818 programmable controller) with the oxygen partial pressure controlled with Ar/O_2 (for high pO_2 range) or CO/CO_2 (for low pO_2 range) gas mixtures. The temperature difference was naturally generated in the furnace by moving the sample along the length of the furnace outside of the central isothermal region. The sample was allowed to equilibrate for 2hr between each set of measurements before measurements were made. The voltage and polarity of the hot end was measured using a nano-voltmeter (Keithley 197), while simultaneously measuring the temperatures (using thermometer, Omega HH506R) at the hot and cold ends using two pairs of type-S thermocouples.

The measurement was performed at a constant temperature, but at different temperature gradients *dT*. The resultant *dV* was plotted against *dT* to obtain the TEP coefficient, *Q* (Eq.(59), p.56).

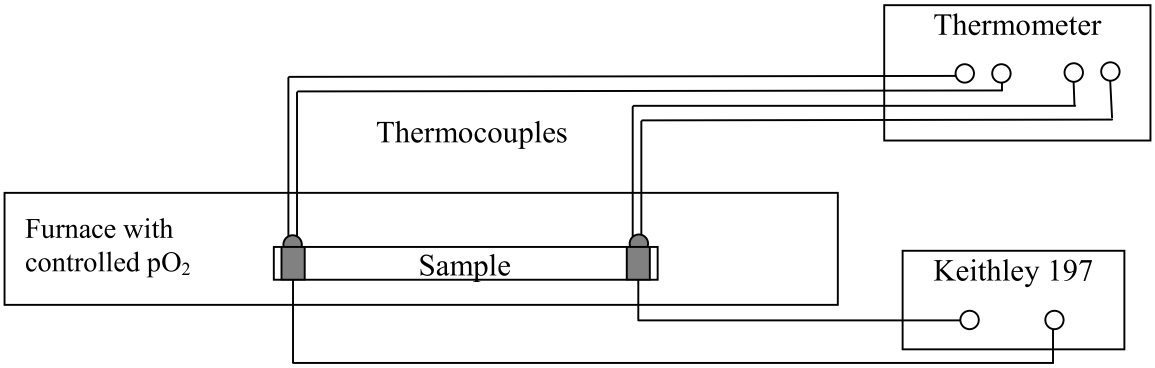

Figure 17: Experimental setup for thermoelectric power measurements.

3.2.4 Concentration Cell Measurements

Concentration cell measurements were performed on undoped langasite and 5%Nb-doped langasite to determine their ionic transference numbers. This is important for independently verifying the predictions of the defect model.

Slabs of undoped and 5%Nb-doped polycrystalline langasite were cemented onto one end of alumina tubes using a high temperature cement (Ceramabond 569, Aremco Products Inc, Valley Cottage NY). After the cement dried at room temperature overnight, the interface was sealed against gas leakage using a glass frit dispersed in deionized water (Glass #13, Elan Technology, Midway GA), which was fired at 1000°C before measurements were performed. The experiment was performed in a tube furnace (Thermolyne 21100) with temperature varying from 700 to 1000°C (controlled using Eurotherm 818), and the oxygen partial pressure was varied by using CO/CO_2 or O_2/Ar gas mixtures. The open circuit voltage (V_{oc}) was measured (using Keithley 196) after equilibrating the setup at a set condition for 2hrs. The experimental apparatus for obtaining the ionic transport number is shown in Figure 18.

The open circuit voltage was then plotted as function of pO_2, and fitted with Eq. (66) (p.57). The first derivative of the fit was then taken. The first derivative of that plot at various pO_2 was related to the ionic transport number and ionic transport numbers at various temperatures can be obtained as function of pO_2 using Eq. (65) (p.57).

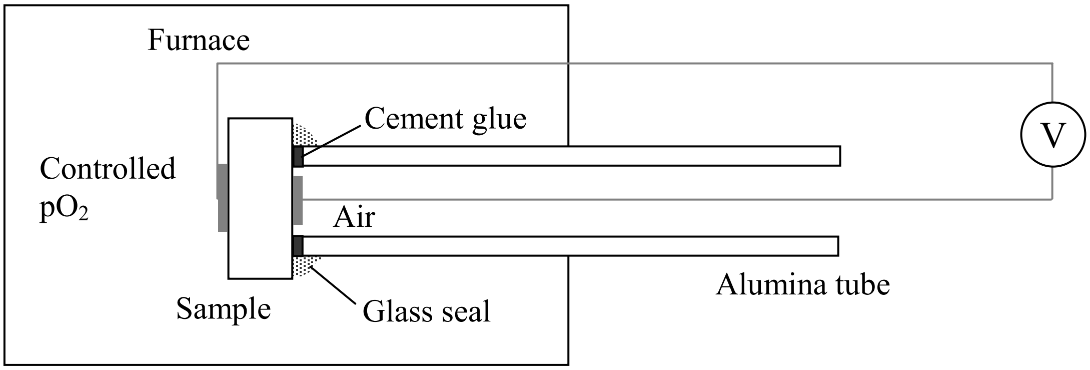

Figure 18: Experimental setup for concentration cell measurements.

3.2.5 *Oxygen Exchange and Diffusion studies*

Oxygen exchange experiments were performed by our colleagues and collaborators at the University of Clausthal in Clausthal, Germany. Due to their importance in the understanding of the transport properties of langasite, a brief description is given here. The samples used were prepared by us as in 3.2.1 so that they could be compared directly against the results from impedance studies.

Oxygen diffusion in langasite was studied and reported recently by M. Schulz et al [146], our collaborators, using the oxygen isotope exchange method. It utilized the exchange of stable tracer isotope ^{18}O with the naturally occurring ^{16}O in our langasite samples. The samples were exposed to ^{18}O-rich oxygen mixture at temperatures from 400-1000°C to allow for ^{18}O-^{16}O exchange. Secondary Ion Mass Spectrometry (SIMS) was then utilized to evaluate the concentration profile of oxygen in the langasite samples. The oxygen self-diffusivity is then extracted by fitting the oxygen concentration profile. In polycrystalline material, one has to take into account the different diffusion mechanism that is in play in the grain boundaries; the details are given in [146]. In this study, the profiles for Nb-doped langasite were found to be too noisy due to high porosity and therefore only 1%Sr-doped and the undoped samples were analyzed.

3.3 Sensor Studies

3.3.1 *Device Preparations*

Langasite single crystals were cut in the Y-direction, grounded and polished into discs. The resonator was loaded into the sputtering chamber and pumped down to a vacuum of 5×10^{-6} torr. To deposit the electrodes, 10nm of titanium were first sputtered as an adhesion layer, followed by 120nm of platinum using a contact mask. The deposition was done using 50W of DC power at room temperature, with working pressure of around 5 mtorr. The deposition rates for both titanium and platinum were determined to be ~10 nm/min. The final resonant frequency for the langasite resonators created ranged from 3.5 to 4.0MHz.

We also obtained AT-cut quartz crystal microbalances (QCM) for testing of various active films for sensing applications. It allows us to evaluate the sensitivity of film materials cheaply and quickly before depositing them on langasite resonators. The AT-cut QCM were obtained from Maxtek Inc, with resonant frequencies of 5MHz (Part #149211-2). Electrodes in al the QCM were gold, with chromium as adhesion layer.

Active films were deposited onto the resonators using pulsed laser deposition (PLD) and PMMA templating technique. The two methods are detailed below.

$Pr_{0.15}Ce_{0.85}O_2$ film preparation using PLD

Solid solution $Pr_{0.15}Ce_{0.85}O_2$ (praseodymium-cerium oxide, PCO) was deposited onto a single crystal Y-cut langasite resonator (resonant frequency of 4.0MHz) with Pt electrodes using pulsed laser deposition (PLD). A PCO target was prepared using the mixed oxide route by combining appropriate amounts of praseodymium oxide (Pr_2O_3) and cerium oxide (CeO_2) (Alfa Aesar, 99.99% metal basis). The target was first uniaxially and then equiaxially pressed, and then sintered at 1100°C in air. The PCO target was then used for PLD, which allowed precise stoichiometric PCO to be deposited onto the langasite resonator.

The langasite resonator (Y-cut) was loaded into the vacuum chamber. The chamber was then pumped down to 3.5×10^{-6} torr for deposition. The deposition was performed at room temperature, with the excimer laser set at 700mJ (~2.809J/cm^2) and ablation frequency of 20Hz. The final PCO thickness obtained was 150nm, with average deposition rate of 0.02nm/pulse.

$BaCO_3$ film preparation using PMMA templating technique

This technique was introduced to our group by T. Hyodo, and both $BaCO_3$ and SiO_2 films were coated onto the resonators by him. This technique has been shown [147] to improve sensing properties tin oxide towards NO_x and H_2, and allows us to deposit highly porous films for high specific surface area.

$BaCO_3$ (barium carbonate) films were deposited using the PMMA templating technique [148] onto 5MHz (Maxtek Inc) AT-cut quartz resonators respectively. In addition, $BaCO_3$ films were also deposited onto 3.6MHz Y-cut langasite resonators. The first step of this technique is to create a 3-D array of PMMA microspheres. For that, about 0.20g (800nm in diameter) or 0.16g (400 nm in diameter) of PMMA microspheres (Soken Chem. & Eng. Co., Ltd.) was dispersed in 10 ml deionized water using ultrasonicator for 10min. The suspension was then dripped by pipette onto one electrode face of quartz resonators and allowed to dry at room temperature over night. Only the 800nm PMMA template was used on the langasite resonator. The resultant scanning electron microscope (SEM) images of the structures are shown in Figure 19.

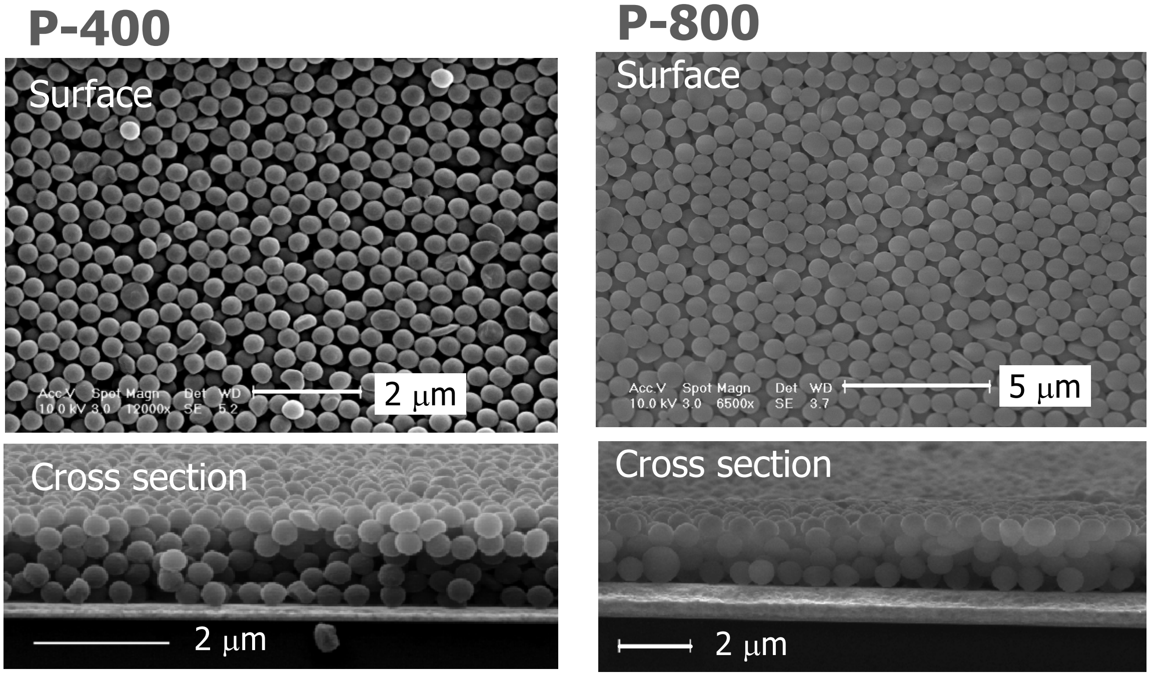

Figure 19: 3-D arrays of PMMA microspheres with different diameters (left-400nm, right-800nm).

For the $BaCO_3$ film, 1.5M $Ba(CH_3COO)_2$ aqueous solution was permeated (using a pipette) into the interstices of the 3-D array of PMMA microspheres, in vacuo, at room temperature. Additional platinum chloride (~0.075mol/liter) was added to the

$Ba(CH_3COO)_2$ on the Y-cut langasite resonator to include Pt catalyst in the active film. Thereafter, the resultant film was subjected to heat treatment at 400°C for 2hr to remove the PMMA microspheres through thermal decomposition and to obtain the porous $BaCO_3$ framework. The resultant microstructures of the $BaCO_3$ films are shown in Figure 20, with interconnected pores derived from PMMA size.

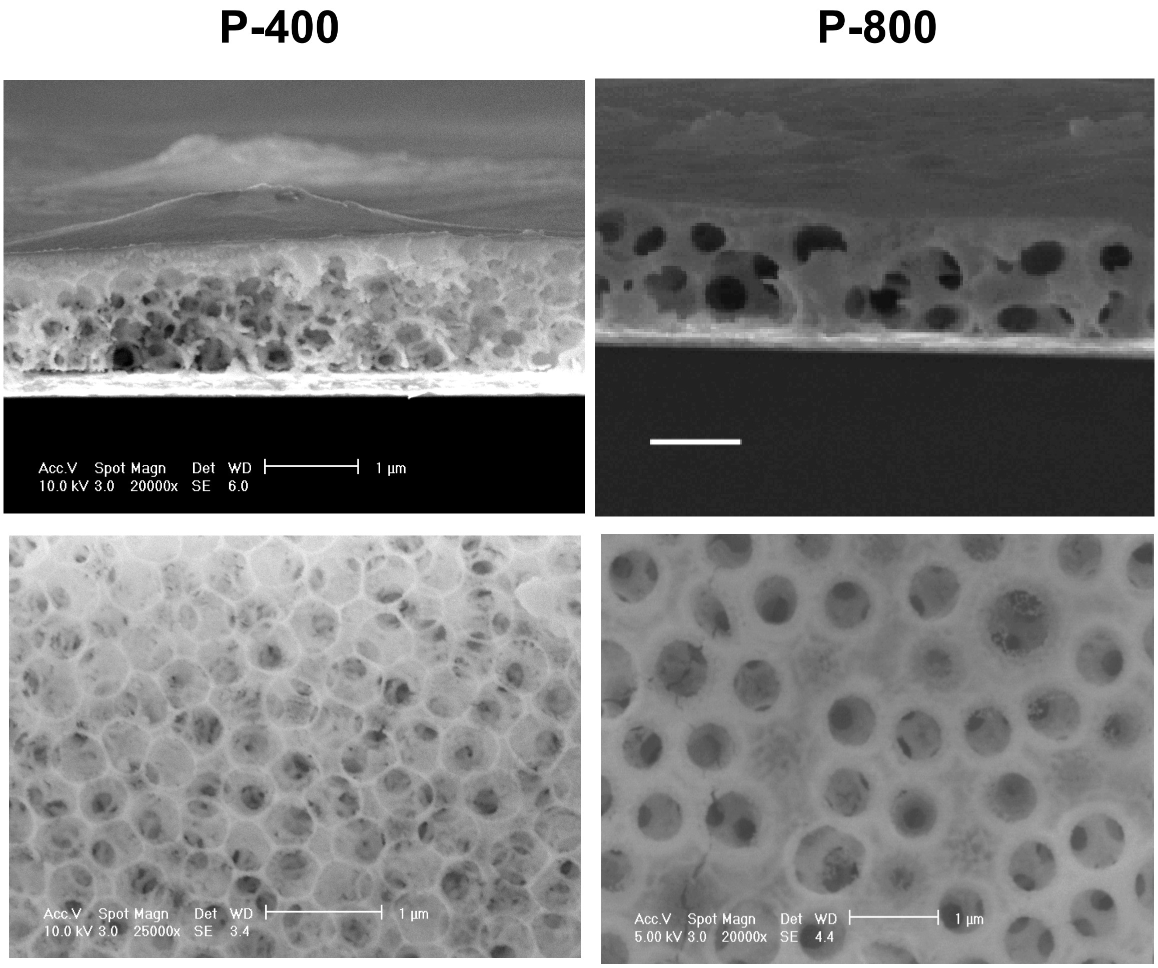

Figure 20: Microstructures of $BaCO_3$ films from 400nm and 800nm diameter PMMA microspheres (without Pt catalyst).

3.3.2 Sensor Testing

Sensor testing was performed in an air-tight chamber in a furnace (Thermolyne 21100 tube furnace with controller) for atmospheric and temperature control. Gas species of interest were continuously flowed into the chamber, and the flow rate and gas composition were controlled manually using mass flow controllers (4 flow valves, MKS 1259C, with multi-channel mass flow controller MKS 647A). Two resonators, the sensor and the reference, were placed in close proximity in the test chamber. The sensor was a resonator with the appropriate active film that was selective towards the chemical of interest. A reference, a resonator without the active film, was used for compensation of extraneous effects, e.g. temperature fluctuations.

The resonant frequency was monitored using a network analyzer (Agilent E5100A[5]). A low-loss high frequency power splitter (Agilent 11850C) was used to divide the output power so that both resonators (sensor and reference) were excited simultaneously. A pair of K-type thermocouples was placed near the sensor for temperature measurements and the thermocouple voltage was recorded by the HP 3478A multimeter.

The computer with GPIB controller and Labview (National Instrument) program recorded the differences in resonant frequency changes of both sensor and reference ($\Delta f = \Delta f_{sensor} - \Delta f_{ref}$) and the thermocouple voltage reading, with about 0.5 second interval between frequency and voltage readings. Following a set of readings, it paused for 6 second before another set of readings was taken. This allowed us to plot Δf versus *time* for sensor testing.

The schematic of the setup is shown in Figure 21, which was used for testing three different sensors as detailed below.

---

[5] The setting up and calibration of Agilent E5100A are outlined in Appendix D.

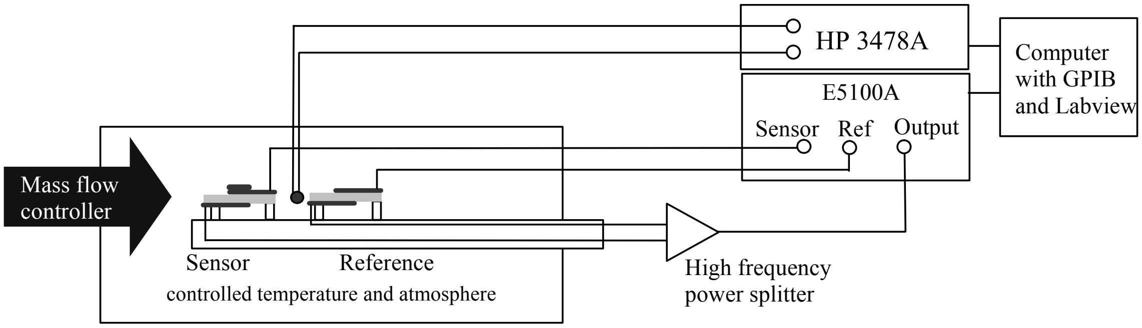

Figure 21: Schematic setup for sensor testing.

Oxygen partial pressure sensing with PCO active film

The solid solution $Pr_{0.15}Ce_{0.85}O_2$ (PCO) was used as the active film on a single crystal Y-cut langasite resonator with Pt electrodes. The fabrication details of this sensor were described in previous section (using PLD, see 3.3.1). The resonant sensor was placed at 600°C at varying pO_2 controlled by changing the ratio of O_2/Ar in the gas mixture. Before measurement, the sensor was first annealed in 100% O_2 at 600°C for a day. The base line was re-zeroed for drift at 30 minutes intervals each time pure oxygen was introduced.

NO_2 sensing with $BaCO_3$ active film

Two sensors were tested: a 5MHz AT-cut QCM (Maxtek Inc) and a Y-cut langasite resonator were coated with $BaCO_3$ films (using PMMA templating technique) and used for NO_2 sensing testing. The fabrication details of this sensor were described in previous section (3.3.1). Gas compositions were controlled using mass flow controllers by varying the flow rate of 100ppm NO_2/Ar, pure Ar and CO/CO_2 gas mixtures. Readings were taken approximately every 6 seconds using Labview (National Instrument) software. During testing, the sensor was equilibrated in Ar for 15 min, exposed to 100 ppm NO_2/Ar for 30 min, reduced in 50%CO/CO_2 mixtures for another 30 min, and finally flushed with argon for 15 min. Temperature ranges for the tests were 250-400^{o}C for QCM based sensor and 250-700^{o}C for langasite based sensor.

Chapter 4: Results

4.1 General

This chapter contains results from both the transport and sensor studies, divided into two subsections. The transport studies examine the electrical and transport properties of langasite at high temperatures and over a range of oxygen partial pressures. They also examine the influence of dopants on those properties. The sensor studies examine the sensitivities and response times of the resonant sensors to their respective target chemicals.

4.2 Transport Studies

4.2.1 Impedance Spectroscopy

Two-point impedance spectroscopy studies were performed on nominally undoped, 1%Sr-doped and 5%-Nb doped langasite samples. Examples of typical impedance spectra obtained for 1%Sr-doped langasite in 100%O_2 atmosphere at different temperatures are shown in Figure 22, with symbols representing the impedance of the material at a certain frequency and the solid lines are the fitted lines to the data using the equivalent circuit (Figure 16, p.64).

Zview software (Scribner Associates Inc., Version 2.0) was used for fitting the spectra. The equivalent circuit (Figure 16, p.64) was defined in the software and the fitting routines generated fitted values for each element in the equivalent circuit. The high frequency arc (i.e. the largest arc in a spectrum in Figure 22), with the corresponding resistance and capacitance, can be attributed to the bulk resistance. Similar analyses were performed for all three different samples at all the experimental pO_2 and temperature ranges. Bulk conductivities were then extracted as function of pO_2 and temperature. DC biasing up to 2V shows no effect on the impedance spectra.

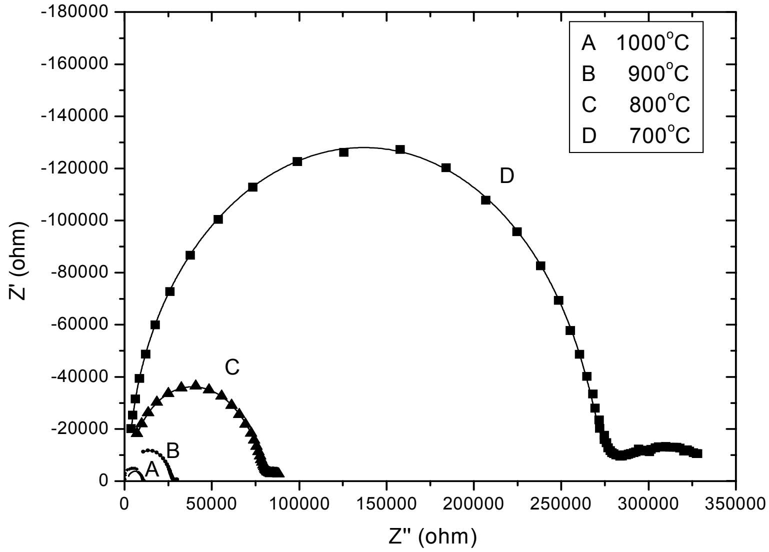

Figure 22: Impedance spectra for 1%Sr-doped langasite at different temperature in 100% O_2 atmosphere.

4.2.2 Electrical Conductivity of Nominally Undoped Langasite

The bulk electrical conductivity, as functions of oxygen partial pressure and temperature, of nominally undoped langasite were extracted from impedance spectroscopy spectra using the equivalent circuit described in section 3.2.2 (Figure 16, p.64).

Figure 23 shows the bulk electrical conductivity and its dependence on oxygen partial pressure. The symbols represent the measured bulk conductivity data. The dashed lines are fitted conductivity values based on defect model derived below (see in 1.5, p.46). One observes that at high pO_2, the bulk electrical conductivity is pO_2 independent. Under reducing conditions, the bulk electrical conductivity begins to acquire a dependence on pO_2. At sufficiently low pO_2, the conductivity approaches a $pO_2^{-\frac{1}{4}}$-dependence, as we demonstrate below. This is indicative of an acceptor-type defect behavior in Region II, where the pO_2-independent conductivity is ionic in nature and fixed by the acceptor and the electron and hole density follow a $pO_2^{-\frac{1}{4}}$ and $pO_2^{\frac{1}{4}}$-dependence respectively.

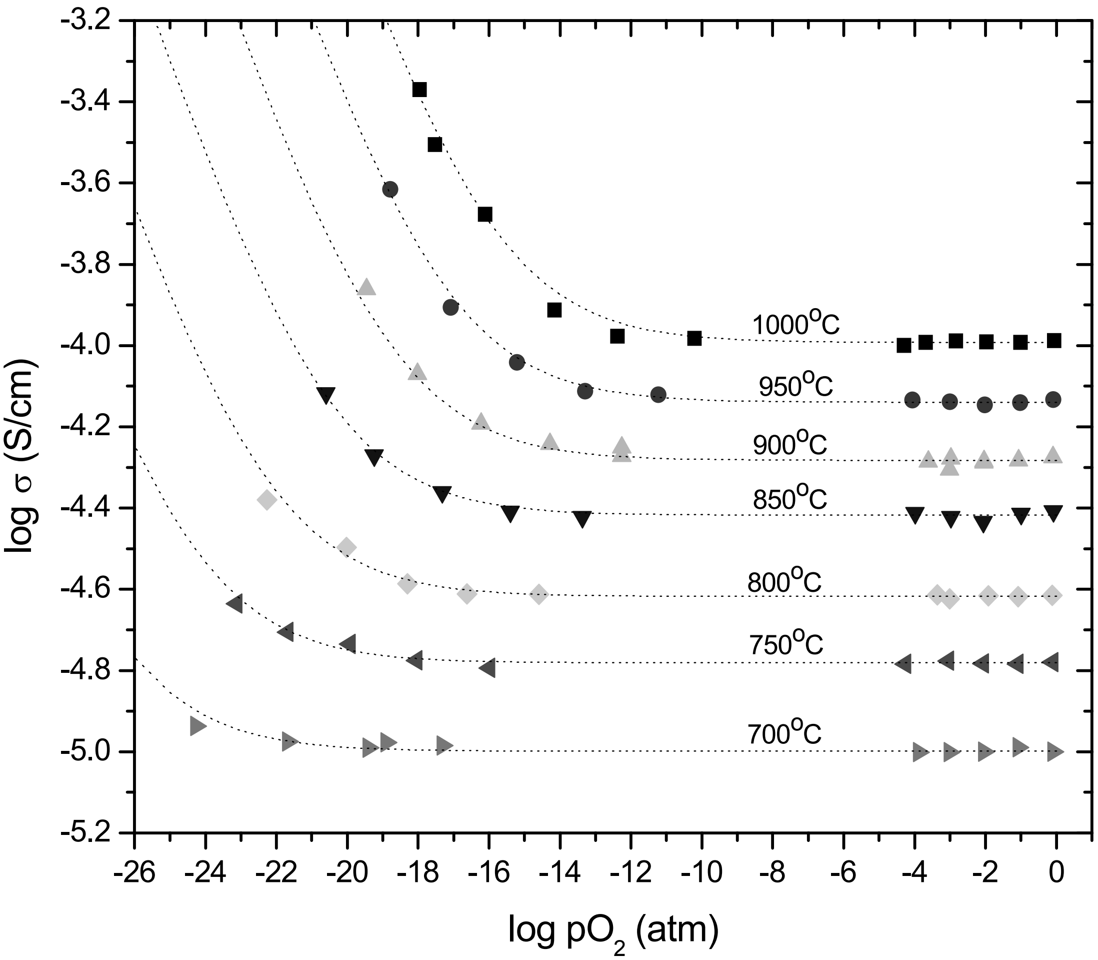

Figure 23: Bulk conductivity of nominally undoped langasite as function of temperatures and pO_2.

Since it is ascertained that the nominally undoped langasite is in Region II (the shaded area in the Kroger-Vink diagram, see Figure 24), the bulk electrical conductivity will be the sum of contributions from electrons and oxygen vacancies (contributions from other electrical species is negligible, Figure 24). The ionic conductivity can then be separated from the electronic conductivity.

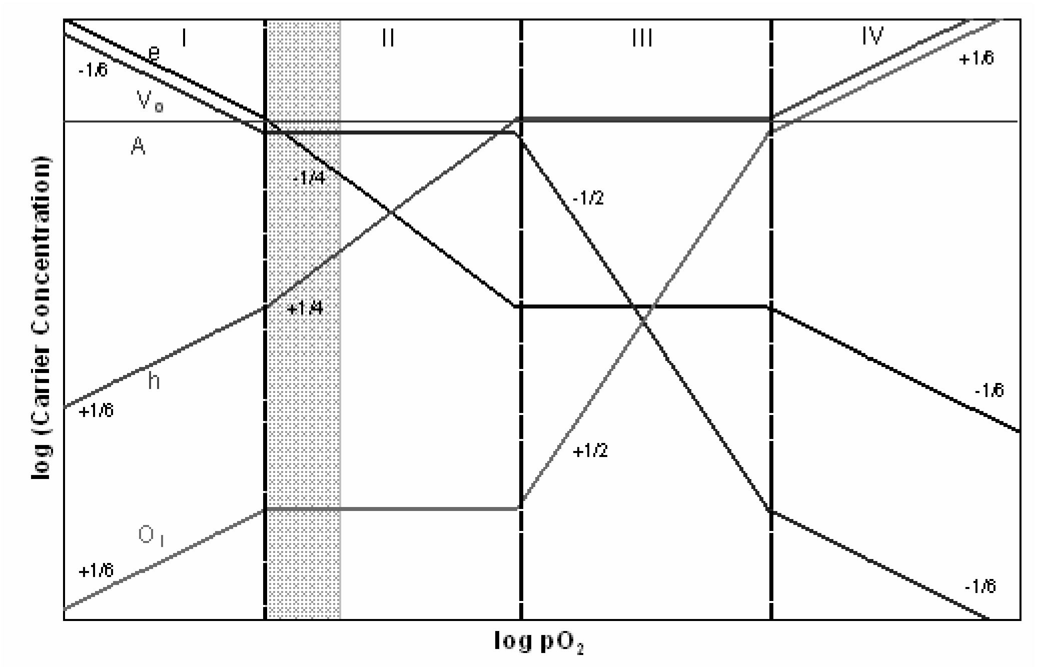

Figure 24: Kroger-Vink diagram of acceptor-doped material with grayed-out area indicating the regime nominally undoped langasite was operating.

From the bulk conductivity data (Figure 23), the ionic conductivity is then simply the pO_2-independent conductivity (high pO_2 regime). Ionic conductivity is defined as:

$$\sigma_{ionic} = ZqC_i\mu = ZqC_i\frac{\mu_o}{T}\exp\left(-\frac{E_m}{kT}\right) \tag{67}$$

where Z is the amount of charge carried by the ionic specie, q is the elemental charge, C_i is the specie concentration, μ is the ionic mobility and E_m is the ionic migration energy.

In order to obtain the migration energy, E_m, we have to plot $\log\sigma_{ionic}T$ as function of inverse temperature. For the nominally undoped langasite, the product of ionic conductivity, contributed by oxygen vacancies, and temperature is plotted as function of inverse temperatures in Figure 25. The activation energy calculated from the plot, assuming an Arrhenius-type relationship, is calculated to be 0.91(±0.01)eV. The Arrhenius relationship, used for the activated process, is:

$$y = A\exp\left(-\frac{E_a}{kT}\right) \tag{68}$$

where y is a physical quantity that is temperature activated, A is the Arrhenius coefficient and E_a is the activation energy. Hence if log y is plotted against $1/T$, the gradient of the plot will give $-E_a/(k \ln 10)$.

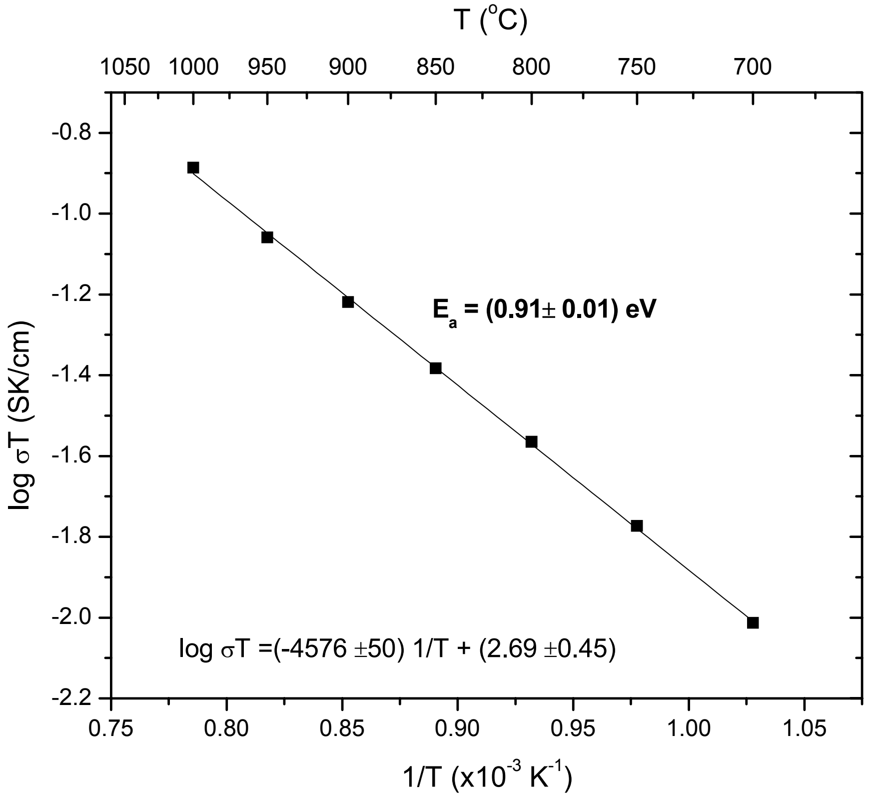

Figure 25: Ionic conductivity-temperature product of nominally undoped langasite.

The electronic conductivity can then be extracted by subtracting the ionic conductivity from the total conductivity in the lower pO_2 regime, where the electrical conductivity becomes pO_2-dependent. The extracted electronic conductivity is plotted in Figure 26. The electronic conductivity at each temperature fits well to a -1/4 slope (except at the highest pO_2's where we expect a larger error) indicating good agreement with the defect model (Region II, Table 3, p.51) where n has a predicted $pO_2^{-\frac{1}{4}}$-dependence. Furthermore, the electronic conductivity is conveniently extrapolated to $\log pO_2=0$ and the Arrhenius plot of the electronic conductivity (Figure 27) gives the activation energy of 3.0(±0.02) eV. With expressions for the electronic and ionic conductivities, the total conductivity (sum of the electronic and ionic conductivity) can then be fitted as shown in Figure 23 (dotted lines).

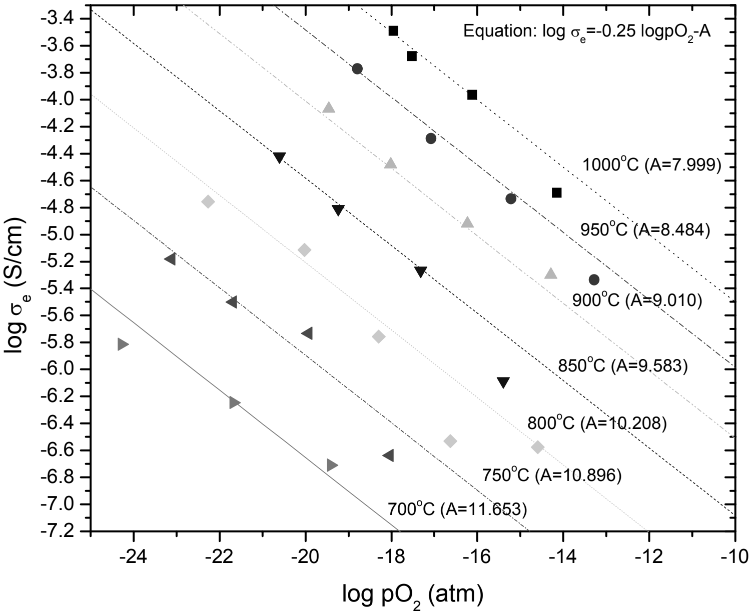

Figure 26: Electronic conductivity of nominally undoped langasite as function of temperature and pO_2.

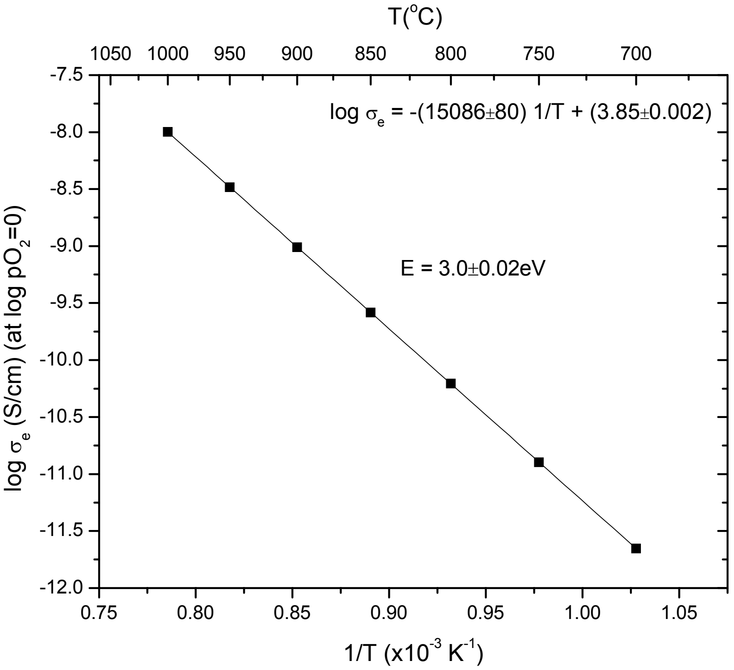

Figure 27: Temperature dependence of electronic conductivity (extrapolated to $\log pO_2=0$) of nominally undoped langasite.

4.2.3 Electrical Conductivity of 1%Sr-doped Langasite

Similarly, the bulk electrical conductivity, as functions of oxygen partial pressure and temperature, of 1%Sr-doped langasite were extracted from impedance spectroscopy spectra using the equivalent circuit described in the Experimental Section (Figure 16, p.64). Figure 28 shows the bulk electrical conductivity and its dependence on oxygen partial pressure for a series of isotherms from 700-1000°C. The symbols represent measured values, and the dashed lines are fitted values based on the defect model (see in 1.5, p.46).

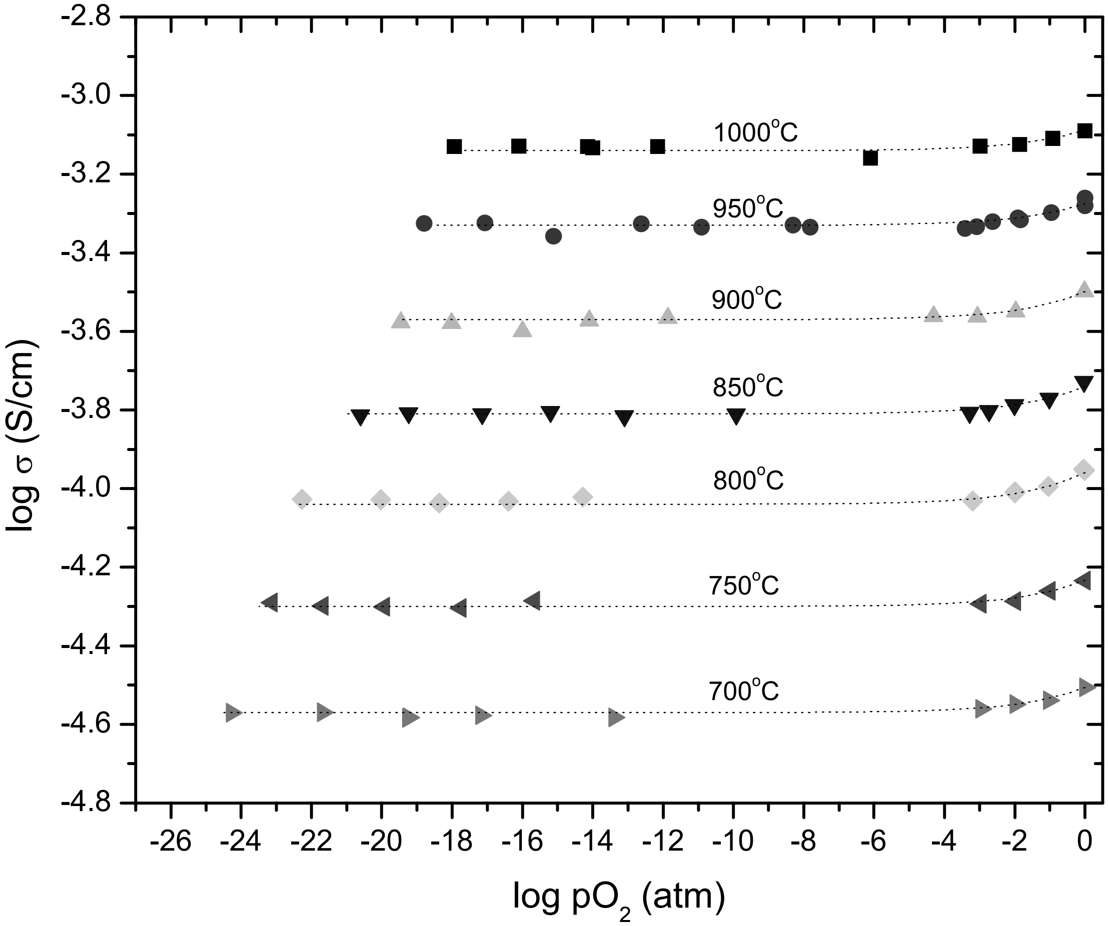

Figure 28: Bulk conductivity of 1%Sr-doped langasite as functions of temperature and pO_2.

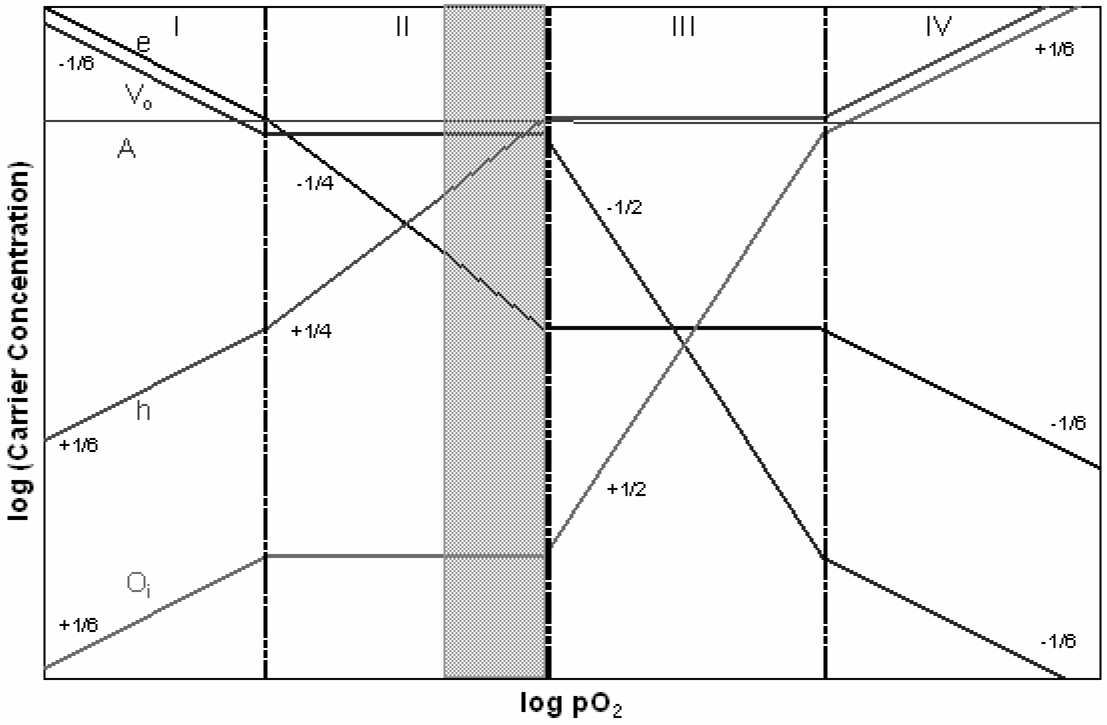

Figure 29: Kroger-Vink diagram of acceptor-doped material with grayed-out area indicating the regime 1%Sr-doped langasite was operating.

In Figure 28, it can be observed that at high pO_2, the bulk electrical conductivity at a fixed temperature has slight pO_2 dependence, while under more reducing conditions, the bulk electrical conductivity becomes pO_2-independent. This electrical conductivity behavior is indicative of a material in Region II of the defect model (as shown in the shaded regime of Figure 29), with its total conductivity contributed mainly by oxygen vacancies and holes. Hole conductivity at high pO_2 is predicted to have a $pO_2^{+\frac{1}{4}}$-dependence (Table 3, p.51), hence explaining the slightly pO_2 dependence in Figure 28. The change in behavior when compared to the nominally undoped langasite can be attributed to the addition of Sr. Since Sr is an acceptor, increasing its level will depress *n*, consistent with the suppression of n-type conductivity at lower pO_2, and increase the ionic and p-type conductivity at higher pO_2, as observed in Figure 28 (Table 3, p.51).

Similar to the case for nominally undoped langasite, the electronic (p-type hole) conductivity can be extracted by subtracting the pO_2-independent ionic conductivity at low pO_2 from the total conductivity at high pO_2. The product of ionic conductivity, contributed by oxygen vacancies, and temperature is plotted as function of inverse temperatures in Figure 30. The calculated activation energy calculated from the plot is 1.27(±0.02)eV. The extracted electronic conductivity is plotted in Figure 31, and is fitted with a +1/4 slope. The fit is acceptable, considering the relatively small hole conductivity, and remains in good agreement with the defect model. The hole conductivity at log pO_2=0 is plotted as function of inverse temperature in Figure 32, giving an activation energy of 1.09(±0.04)eV. The sum of the expressions for the hole and ionic conductivity is then used to calculate the predicted total conductivity as shown in Figure 28 (dotted lines).

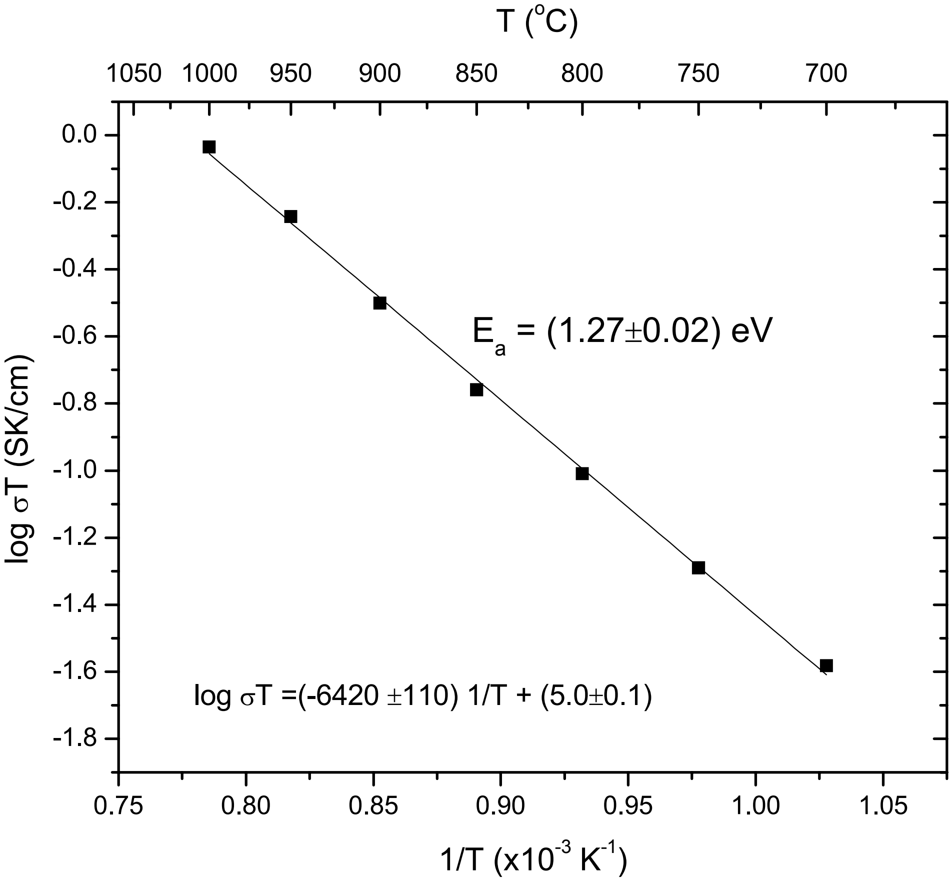

Figure 30: Ionic conductivity-temperature product of 1%Sr-doped langasite.

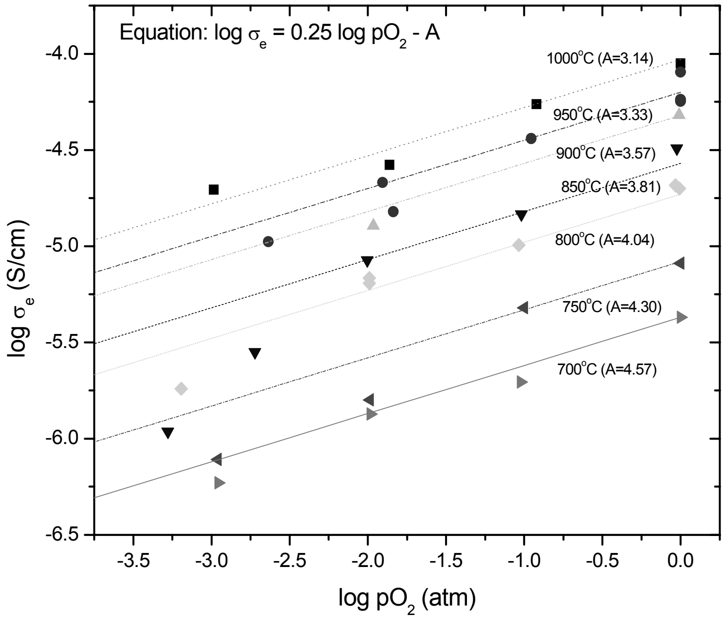

Figure 31: Electronic conductivity of 1%Sr-doped langasite as functions of temperature and pO_2.

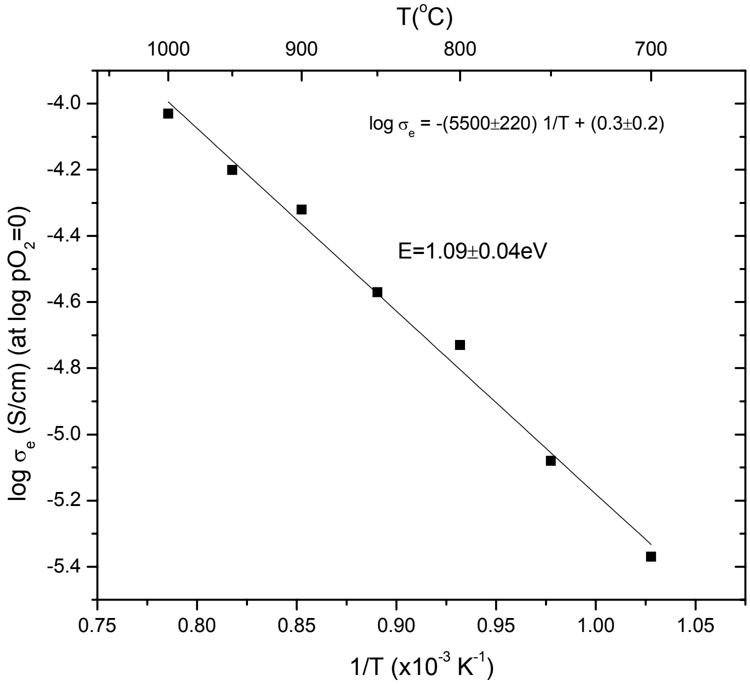

Figure 32: Temperature dependence of electronic conductivity of 1%Sr-doped langasite at log pO_2=0

4.2.4 Electrical Conductivity 5%Nb-doped Langasite

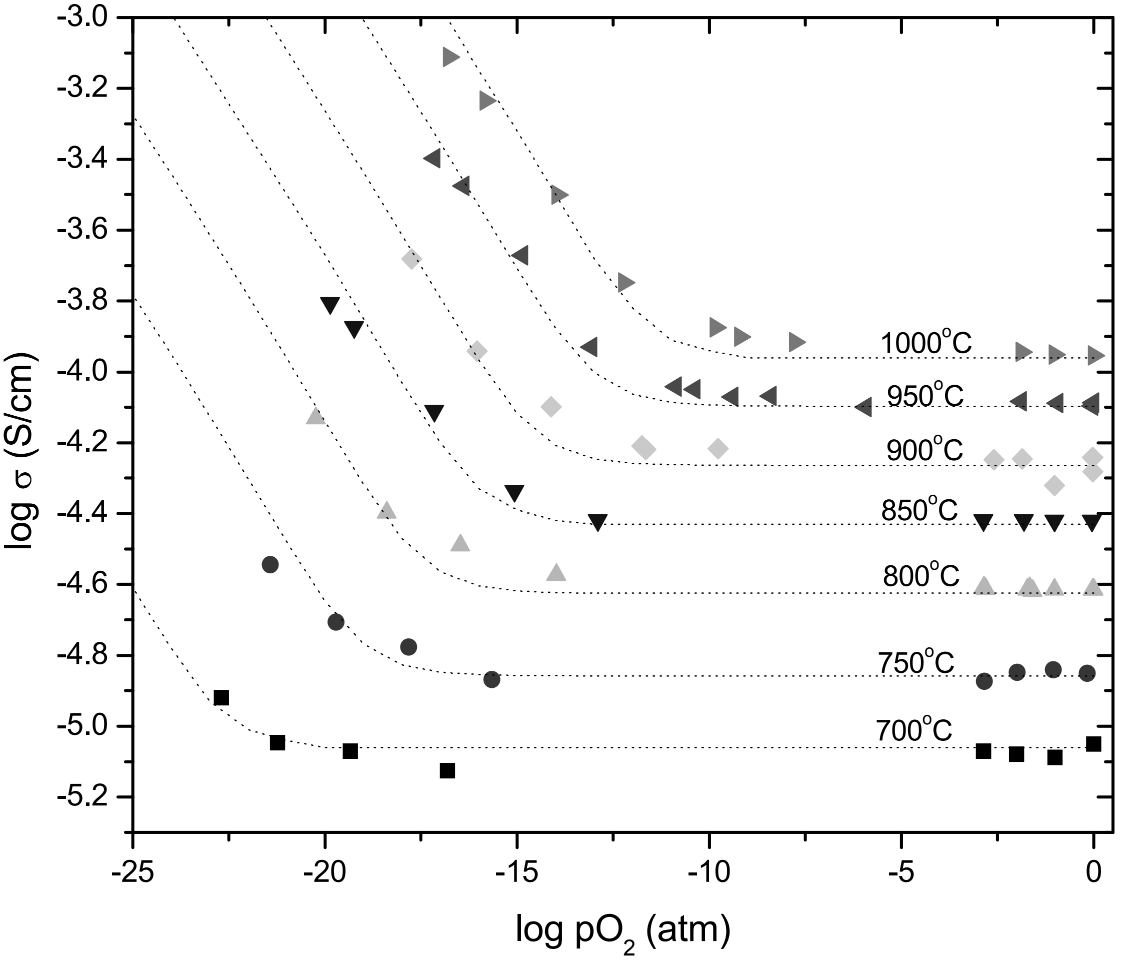

Figure 33: Bulk conductivity of 5%Nb-doped langasite as functions of temperature and pO_2.

The bulk electrical conductivity, as functions of oxygen partial pressure and temperature, of 5%Nb-doped langasite were extracted from impedance spectroscopy spectra using the equivalent circuit described in the Experimental Section (Figure 16, p.64). Figure 33 shows the bulk electrical conductivity and its dependence on oxygen partial pressure for isotherms ranging from 700-1000°C. The symbols represent measured bulk conductivity data, and the dashed lines are fitted values based on the defect model (detailed in Chapter 5, p.124).

In the conductivity data for 5%Nb-doped langasite, it can be observed that at high pO_2, the bulk electrical conductivity at a fixed temperature is pO_2-independentand becomes pO_2-dependent at lower pO_2 as for the acceptor doped material. However, since donors depress oxygen vacancies, we need to look for an alternate explanation. Turning to the defect model for donor-type material in Regions I and II (see shaded regime of Figure 34). In Region I, *n* is $pO_2^{-\frac{1}{6}}$-dependent, and, at higher pO_2, in Region II, *n* becomes pO_2-independent, fixed by the ionized donor concentration (Table 4, p.54). It also means that the conductivity data of 5%Nb-doped langasite in Figure 33 is n-type electronic in nature, i.e. contributed predominantly by electrons, throughout the measured pO_2 range.

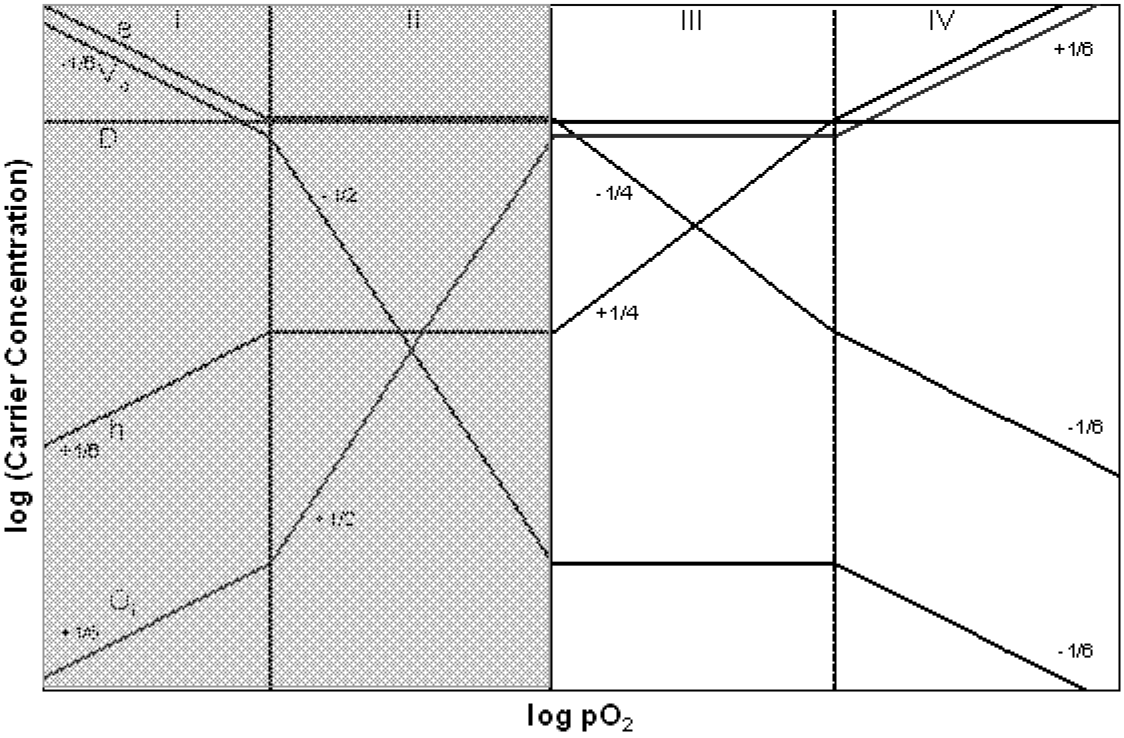

Figure 34: Kroger-Vink diagram of donor-doped material with grayed-out area indicating the regime 5%Nb-doped langasite was operating.

As before, we analyze the data of 5%Nb-doped langasite at the high pO_2 (flat regime) and at the low pO_2 ($pO_2^{-\frac{1}{6}}$-dependent regime) where the Brouwer approximations can be used. The pO_2-independent electrical conductivity data is plotted as function of temperature in Figure 35 for which one calculates an activation energy of 0.91(±0.01)eV.

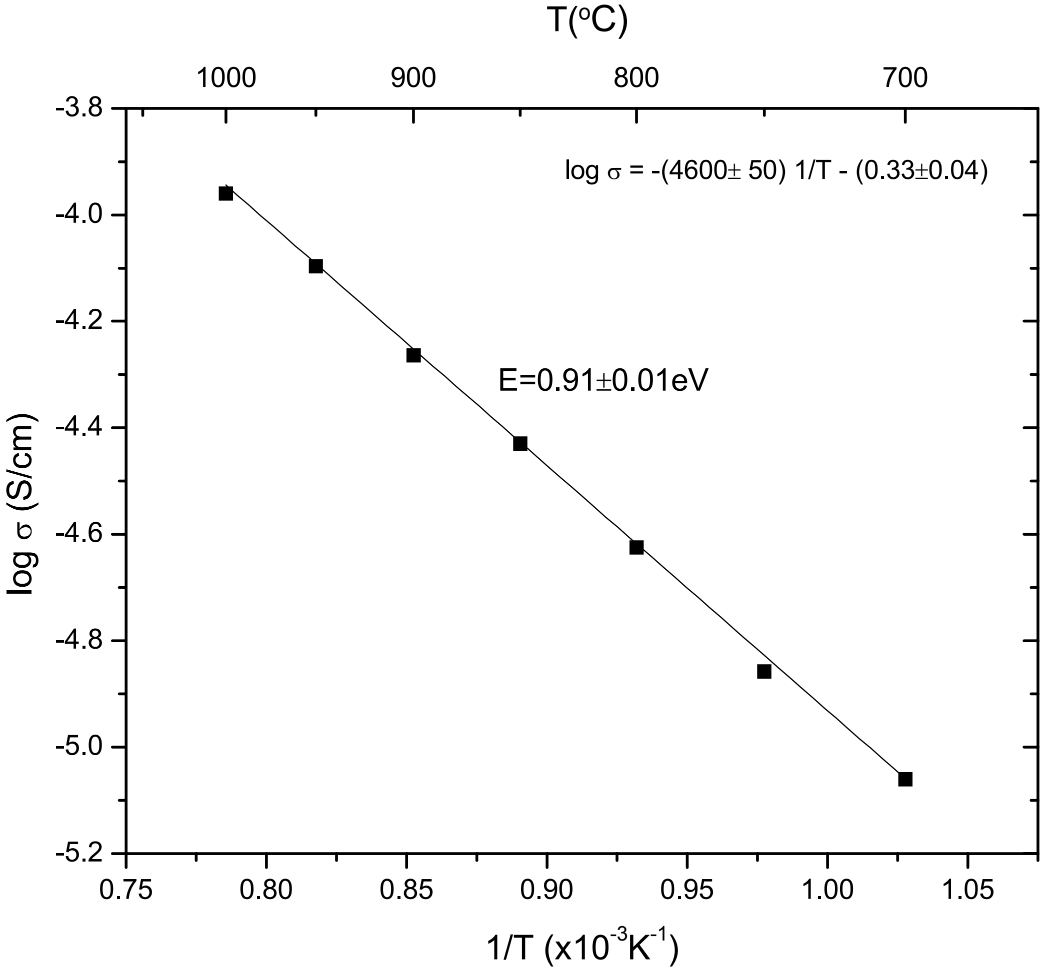

Figure 35: Conductivity at pO_2-independent regime for 5%Nb-doped langasite.

At low pO_2, by extrapolating the electrical conductivity using a $pO_2^{-\frac{1}{6}}$-dependence to $pO_2=10^{-35}$atm, the activation energy for Region I can be obtained by plotting the result as function of inverse temperature (Figure 36). The activation energy of the pO_2-dependent n-type electrical conductivity at the pO_2-dependent is calculated to be 2.34(±0.07)eV.

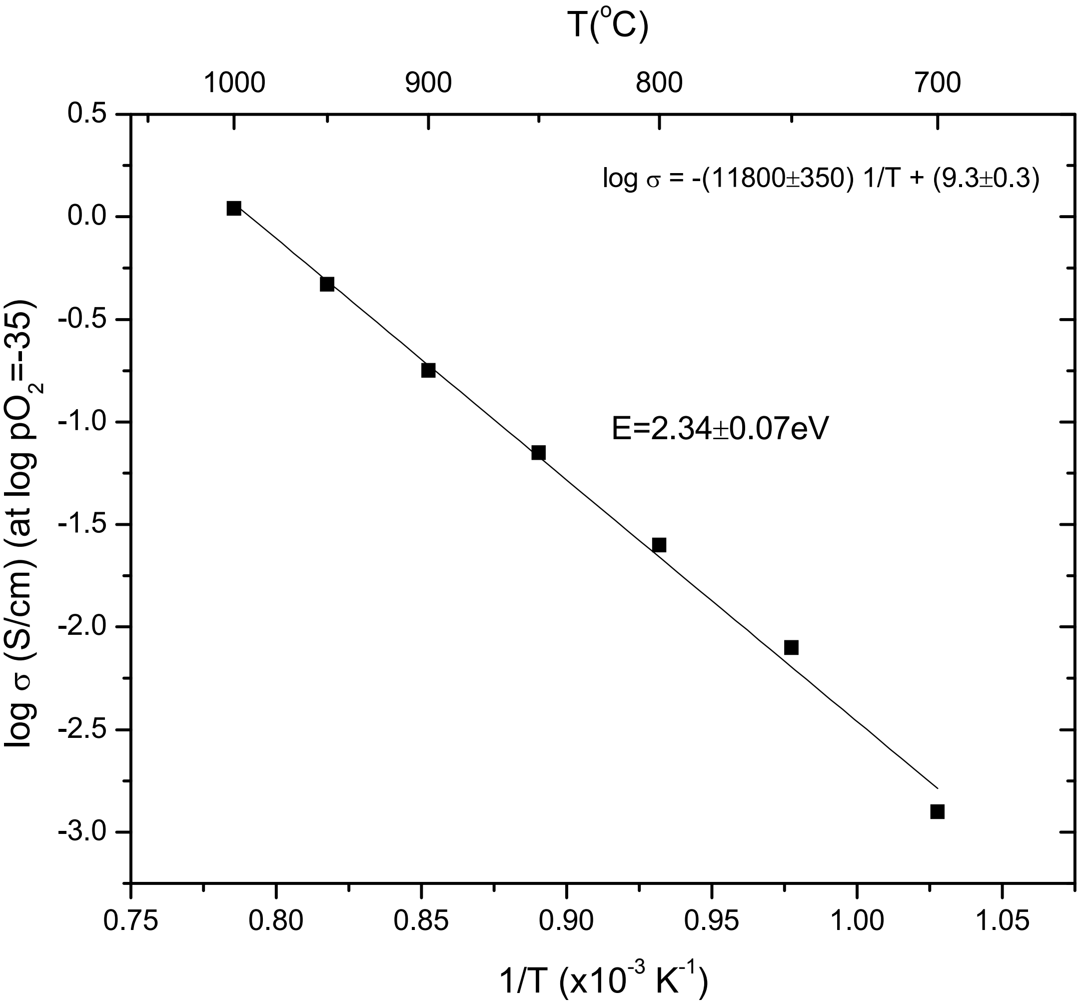

Figure 36: Conductivity at $pO_2^{-\frac{1}{6}}$-dependent regime for 5%Nb-doped langasite.

4.2.5 Thermoelectric Power Measurements

Thermoelectric power (TEP) measurements were performed on 5%Nb-doped langasite so that electrons can be confirmed as the dominant conductive species at high pO_2 and the electron density could be evaluated from the TEP, Q, using Eq. (60) (p. 56), as function of temperature and pO_2. The raw ΔV versus ΔT data in air at different temperatures are presented in Figure 37. The insert shows the normalized plot where intercepts are fixed at the origin. It clearly illustrates that the slope, which is proportional to Q, decreases with increasing temperatures, indicting increasing n as temperature rises as per Eq. (60) (p. 56). The thermoelectric power or Seebeck coefficients, Q, at all the temperatures, were then

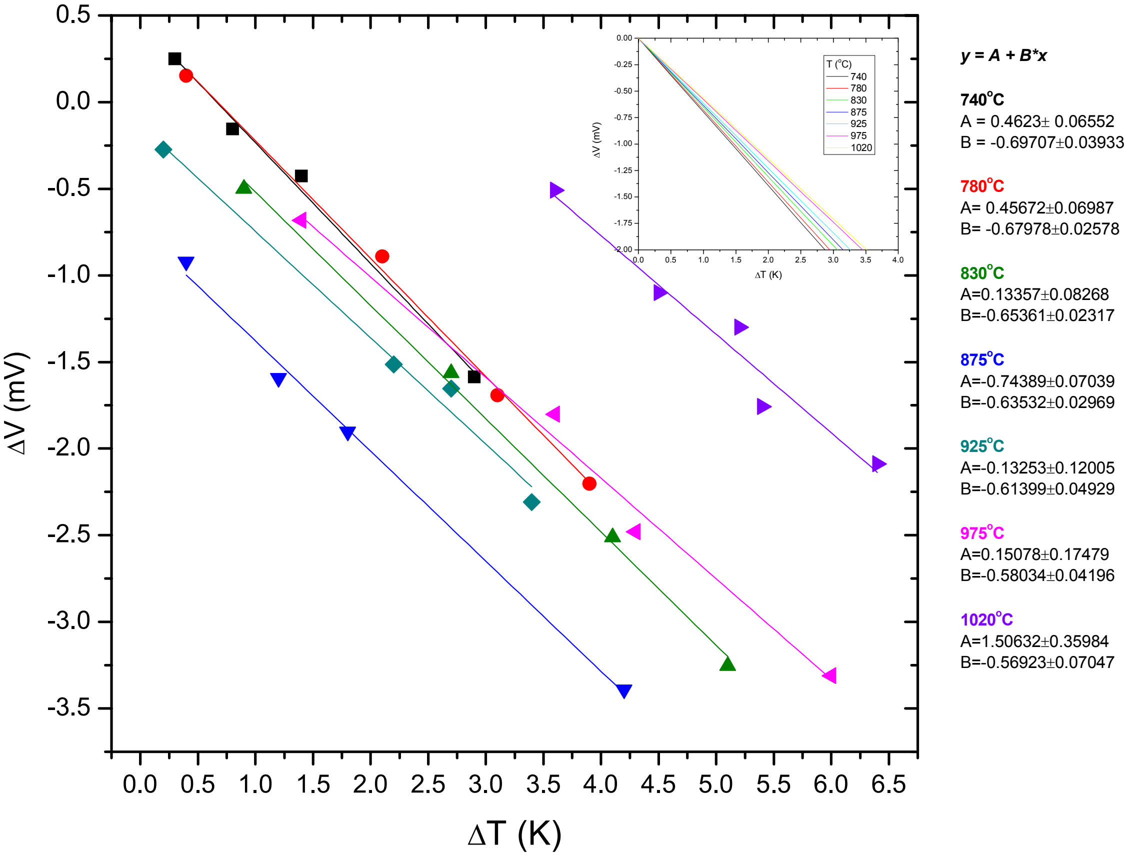

Figure 37: Raw TEP data of ΔV against ΔT for 5%Nb-doped langasite in air obtained at different temperatures. The insert is a normalized plot, where the intercepts are fixed at the origin.

evaluated and plotted in Figure 38. By using Eq. (60) (p. 56), Figure 38 allows the determination of the electron density, *n*, as a function of temperatures. The calculated electron density is plotted versus inverse temperature in Figure 39, giving an activation energy of 0.76(±0.03)eV.

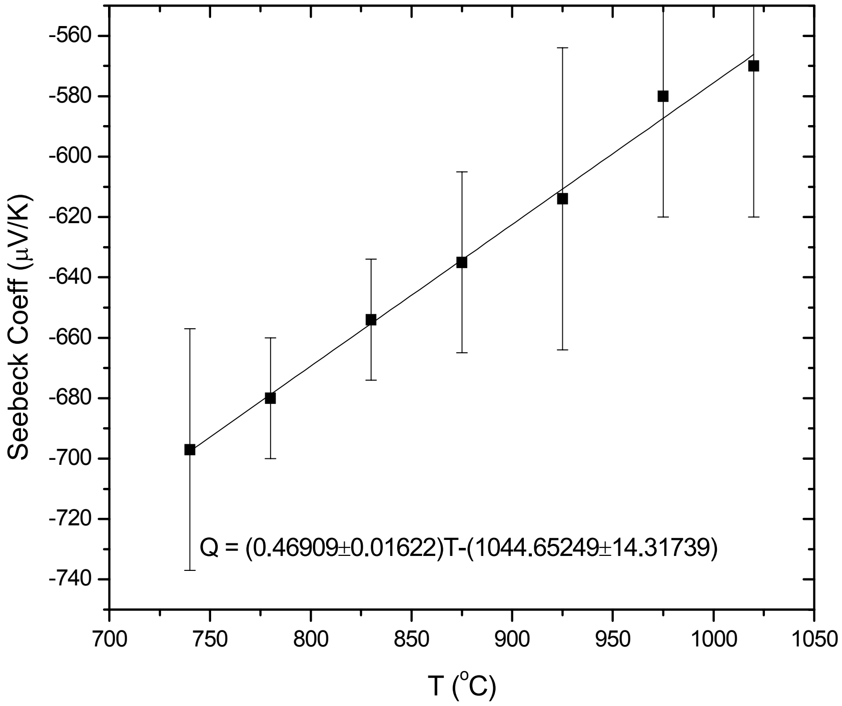

Figure 38: TEP or Seebeck coefficients of 5%Nb-doped langasite in air as a function of temperature.

Using the electron density (Figure 39) and conductivity data from the pO_2-independent regime presented in Figure 35 (p.85), the electron mobility, ($\mu_e = \sigma_e/nq$), as function of temperature is obtained. Note that the actual data for both electron density and conductivity are used, not the fitted results. The results are plotted in Figure 40. The electron mobility, μ_e, is temperature-dependent with a calculated activation energy of 0.15(±0.01)eV.

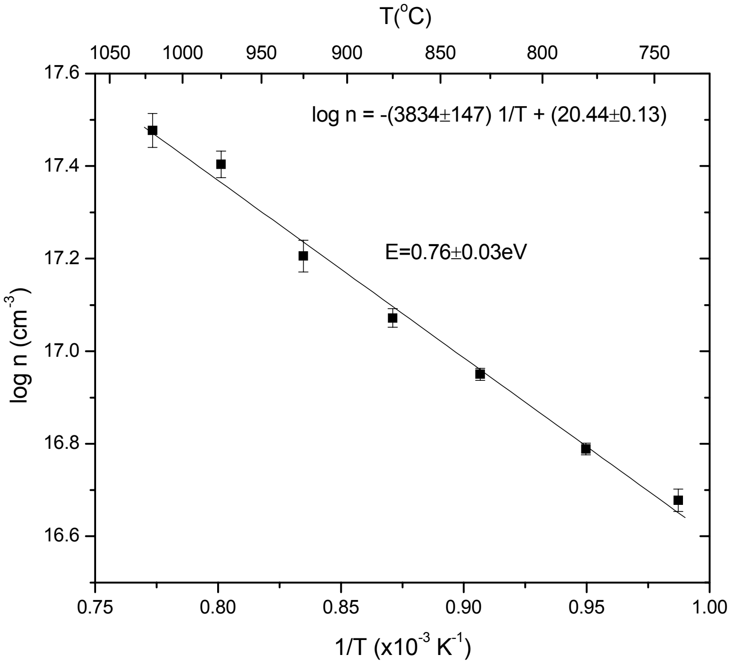

Figure 39: Electron density of 5%Nb-doped langasite in air as function of temperatures.

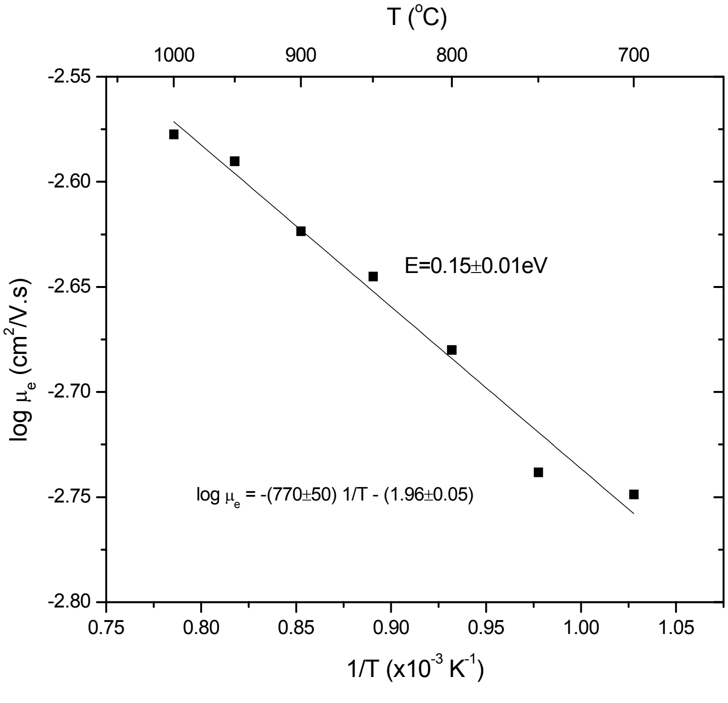

Figure 40: Electron mobility as function of temperature.

TEP measurements were also performed as function of pO_2 for 5%Nb-doped langasite at a fixed temperature of 950°C. A similar range of pO_2 to the conductivity measurements was used so that both sets of results could be easily compared. Q as function of pO_2 is obtained from the gradients of ΔV versus ΔT (Figure 41) for pO_2's from 10^{-19}atm to 1atm using Eq. (60) (p. 56). The results are plotted in Figure 42.

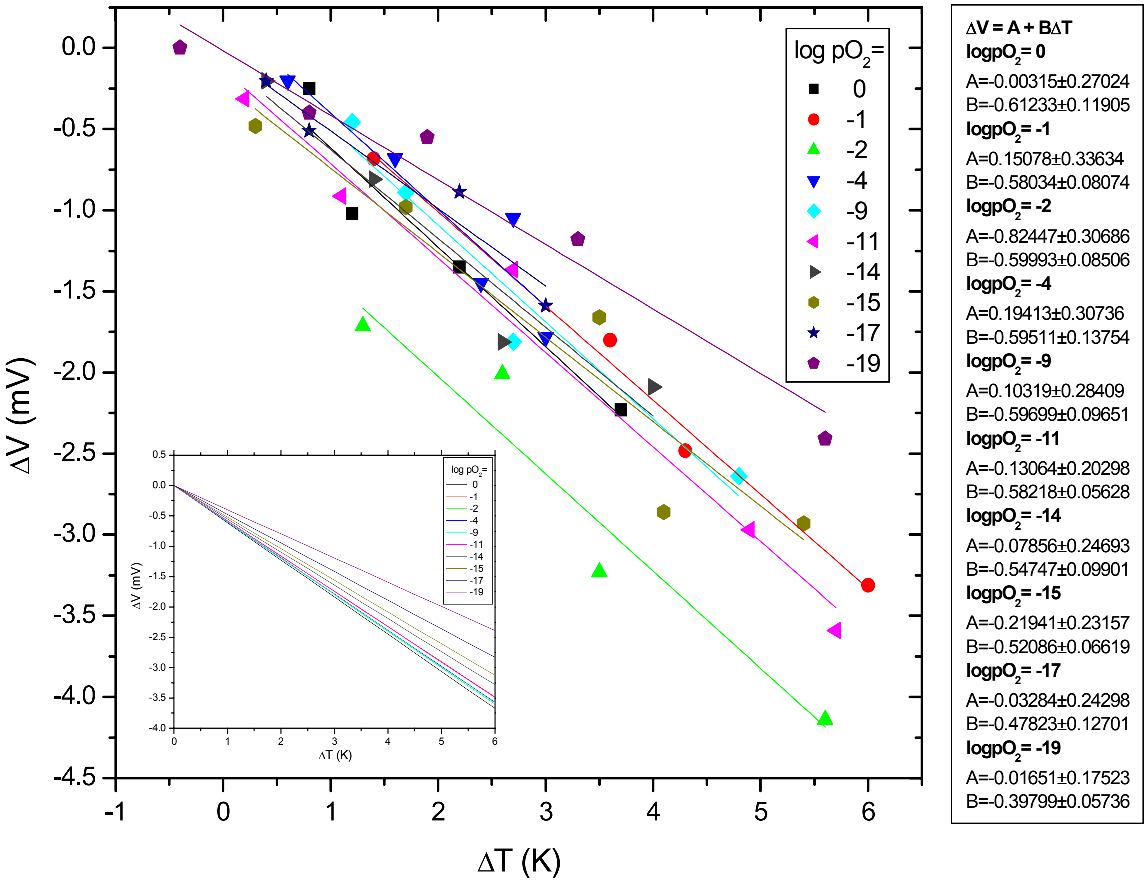

$\Delta V = A + B\Delta T$

$\log pO_2 = 0$
$A=-0.00315\pm0.27024$
$B=-0.61233\pm0.11905$

$\log pO_2 = -1$
$A=0.15078\pm0.33634$
$B=-0.58034\pm0.08074$

$\log pO_2 = -2$
$A=-0.82447\pm0.30686$
$B=-0.59993\pm0.08506$

$\log pO_2 = -4$
$A=0.19413\pm0.30736$
$B=-0.59511\pm0.13754$

$\log pO_2 = -9$
$A=0.10319\pm0.28409$
$B=-0.59699\pm0.09651$

$\log pO_2 = -11$
$A=-0.13064\pm0.20298$
$B=-0.58218\pm0.05628$

$\log pO_2 = -14$
$A=-0.07856\pm0.24693$
$B=-0.54747\pm0.09901$

$\log pO_2 = -15$
$A=-0.21941\pm0.23157$
$B=-0.52086\pm0.06619$

$\log pO_2 = -17$
$A=-0.03284\pm0.24298$
$B=-0.47823\pm0.12701$

$\log pO_2 = -19$
$A=-0.01651\pm0.17523$
$B=-0.39799\pm0.05736$

Figure 41: Raw TEP data of ΔV against ΔT for 5%Nb-doped langasite at 950°C obtained at different pO_2. The insert is a normalized plot, where the intercepts are fixed at the origin.

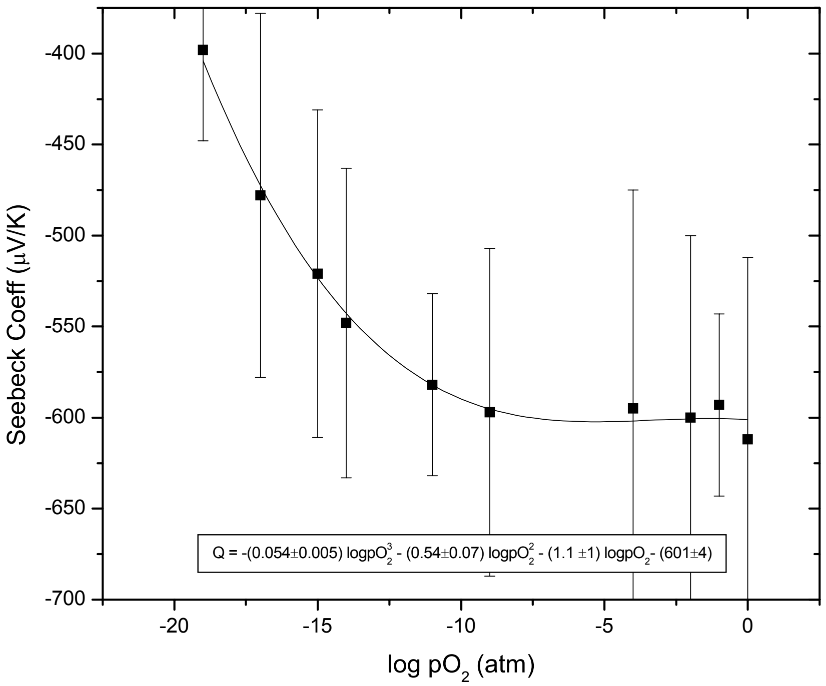

Figure 42: TEP or Seebeck coefficients of 5%Nb-doped langasite at 950°C as function of pO_2.

With Eq. (60) (p. 56), the electron density, *n*, calculated from Figure 42 and its pO_2 dependence at 950°C is shown in Figure 43. These data confirm that both the pO_2-independent conductivity at high pO_2 and the pO_2-dependent conductivity at low pO_2 are both controlled by electrons in contrast to the situation earlier described for acceptor doped langasite. The data also confirms the predicted $pO_2^{-\frac{1}{6}}$-dependence of *n* at low pO_2.

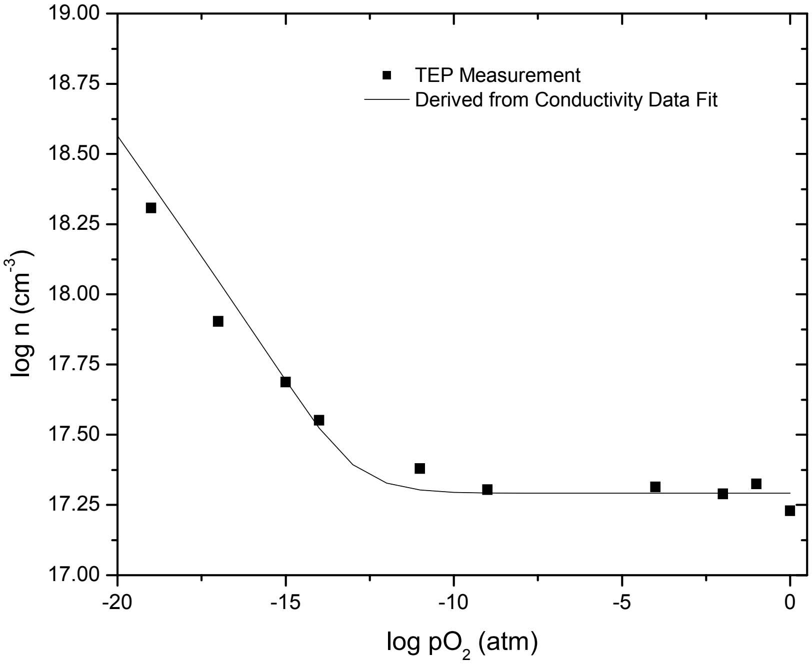

Figure 43: Electron density of 5%Nb-doped langasite at 950°C as function of pO$_2$. The symbols represent *n* values derived from the TEP data collected over a range of pO$_2$. The solid curve is the electron density calculated from conductivity measurements (Figure 33, p.83) using the electron mobility determined in (Figure 40, p.89).

4.2.6 Concentration Cell Measurements

The concentration cell measurements were performed on nominally undoped and 5%Nb-doped langasite samples. For nominally undoped langasite, the raw open circuit voltage, V_{oc}, versus pO$_2$ data at various temperatures were fitted using Eq. (66) (p.57), as shown in Figure 44. Note that voltages up to the order of 1V were obtained confirming a major contribution of ionic to the total conductivity. The first derivatives of the resultant curves at any pO$_2$ can be related to the ionic transference number, t_i, at that specific pO$_2$ (Eq.(65), p.57). The ionic transference number t_i for nominally undoped langasite as function of pO$_2$ is shown in Figure 45.

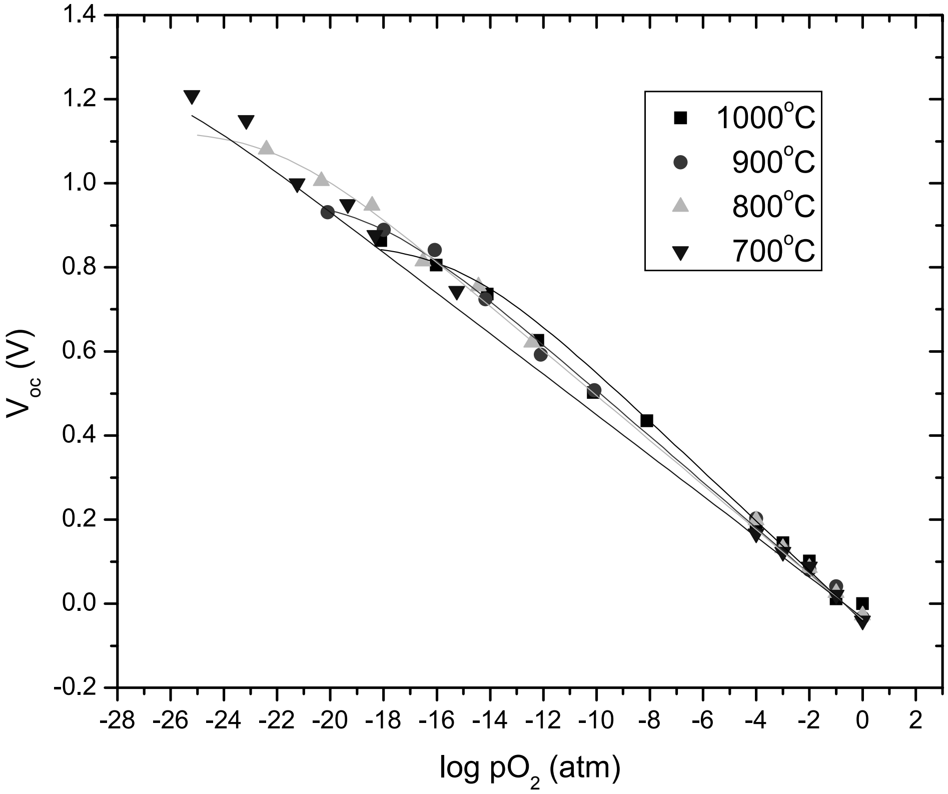

Figure 44: V_{oc} versus pO_2 concentration cell data for nominally undoped langasite.

In Figure 45, the solid lines, derived from the concentration cell data, show the ionic conductivity to be dominant at high pO_2. The fall-off in t_i under reducing conditions is expected based on our expectation of the electron conductivity becoming dominant under those conditions. Likewise, as expected, t_i begins to fall off at higher pO_2 as temperature increases. The concentration cell results are compared with t_i derived from the conductivity data with the aid of the defect model for nominally undoped langasite in Figure 45. The ionic transference number t_i derived from the conductivity data was calculated by taking the ratio of ionic conductivity (Figure 25, p.77) to the total conductivity (Figure 23, p.75) of undoped langasite. Good agreement is observed between the two types of data.

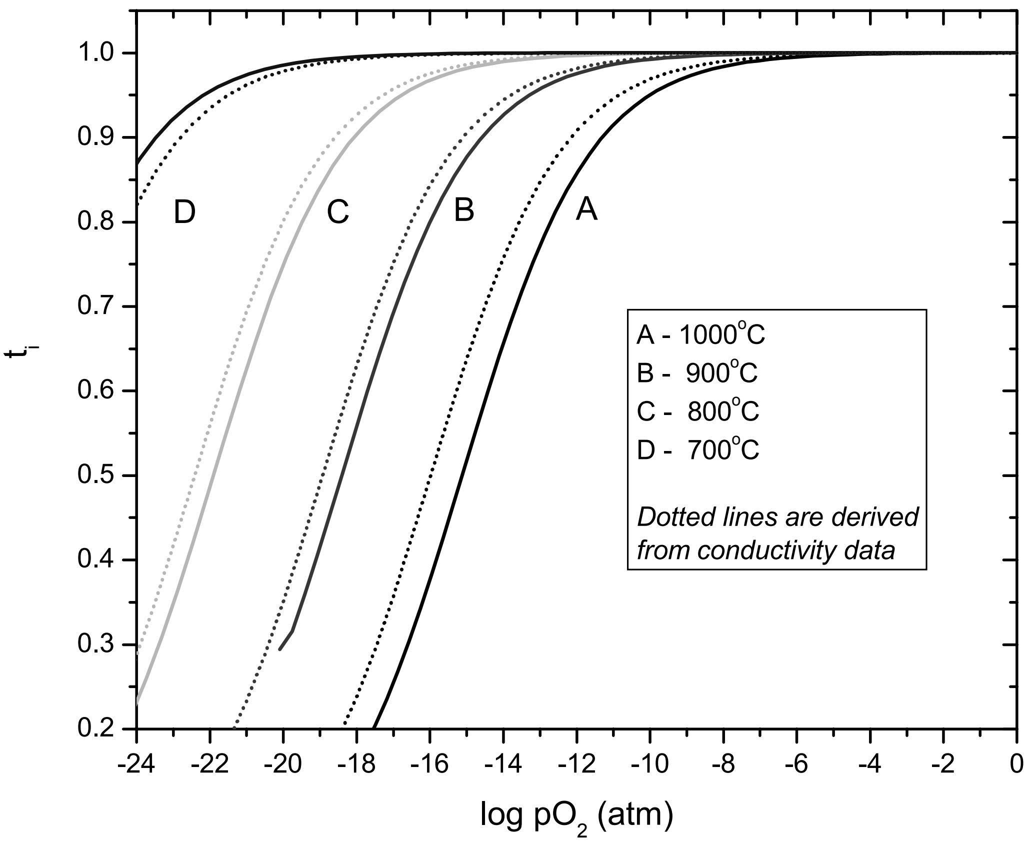

Figure 45: Ionic transport number, t_i, at various temperatures for nominally undoped langasite as function of pO_2. Solid lines are from concentration cell measurements, and dotted lines are derived from conductivity data with the aid of the defect model.

For 5%Nb-doped langasite, the open circuit voltage versus pO_2 data at various temperatures are plotted in Figure 46. The data show a great deal of scatter, but more importantly, the voltages were on the order of mV rather than hundreds of mV as in the case of nominally undoped langasite. Linear curves were fitted to the data at all three temperatures in Figure 46. The average t_i's were evaluated using the obtained gradients (Eq.(64), p.57) and they are at most on the order of 0.1%, consistent with the expectation that the electrical conductivity, even in the pO_2 independent regime is largely n-type electronic.

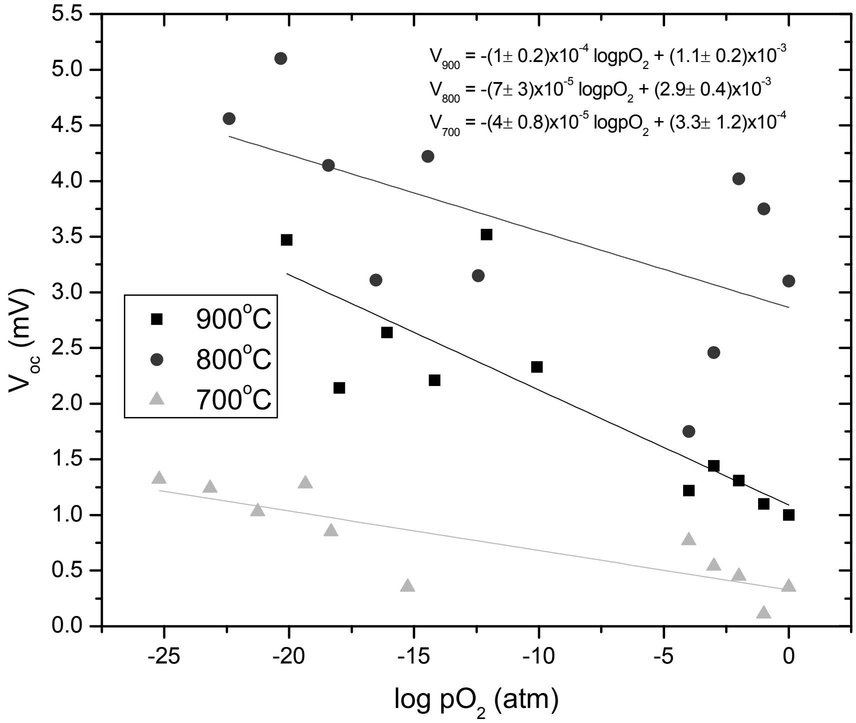

Figure 46: V_{oc} versus pO_2 concentration cell data for 5%Nb-doped langasite.

4.2.7 Oxygen Exchange and Diffusion Studies

Oxygen exchange experiments for nominally undoped and 1%Sr-doped langasite polycrystalline ceramics were performed by M. Schulz et al [146], our collaborators at the University of Clausthal in Germany. The results are presented in Figure 47 along with results for langasite single crystals, which are included for comparison.

The oxygen self-diffusivity is shown to be thermally activated, with activation energy of 1.4eV and 1.1eV for nominally undoped and 1%Sr-doped langasite respectively. Note that for nominally undoped langasite, the data consists of only two points and hence a large error is expected. As comparison, the activation energy for oxygen self-diffusion in single crystals from several sources (Tohuku and IKZ) is about 1.4eV. Figure 47 also shows that 1%Sr addition increases the oxygen self-diffusivity by about an order of magnitude.

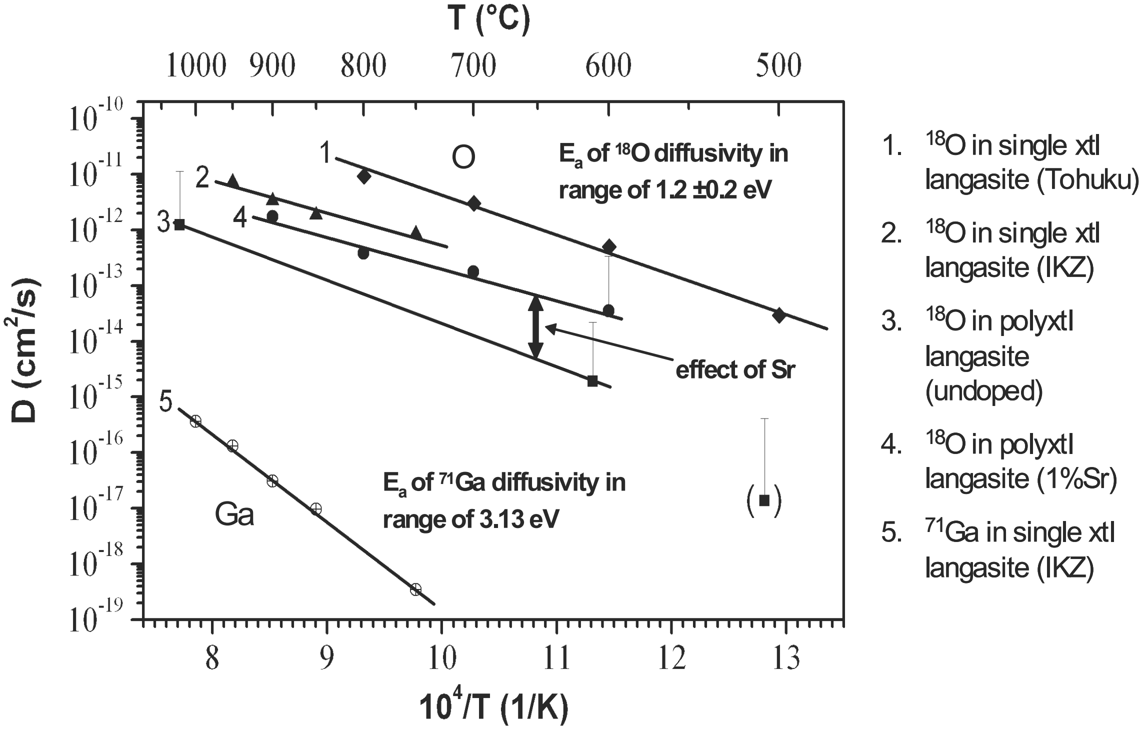

Figure 47: Oxygen and gallium self diffusion versus reciprocal temperature in a series of langasite specimens [146].

Gallium diffusion measurements were performed to alleviate the suspicion that gallium rather than oxygen could be the mobile ionic specie (Si is, in general, covalent and La is large, making both species unlikely to easily migrate within the structure). One observes in Figure 47 that the gallium self-diffusivity, with an activation energy of 3.13eV, is many orders of magnitude lower than that of oxygen. This confirms our assumption that oxygen is the most mobile ion.

4.3 Sensor Studies

4.3.1 Sensor Utilizing Bulk Based Film

The Y-cut langasite resonator coated with a PCO active film had a resonant frequency, f_r, of 4.08266MHz, following annealing at 600°C for one day in a pO_2 of 1atm. The resonant frequency was recorded as a function of temperature and plotted in Figure 48. The temperature coefficient of resonant frequency, df_r/dT, as a function of temperature, was also calculated. The determined df_r/dT in Figure 48 show the increased temperature dependence of f_r as temperature increased.

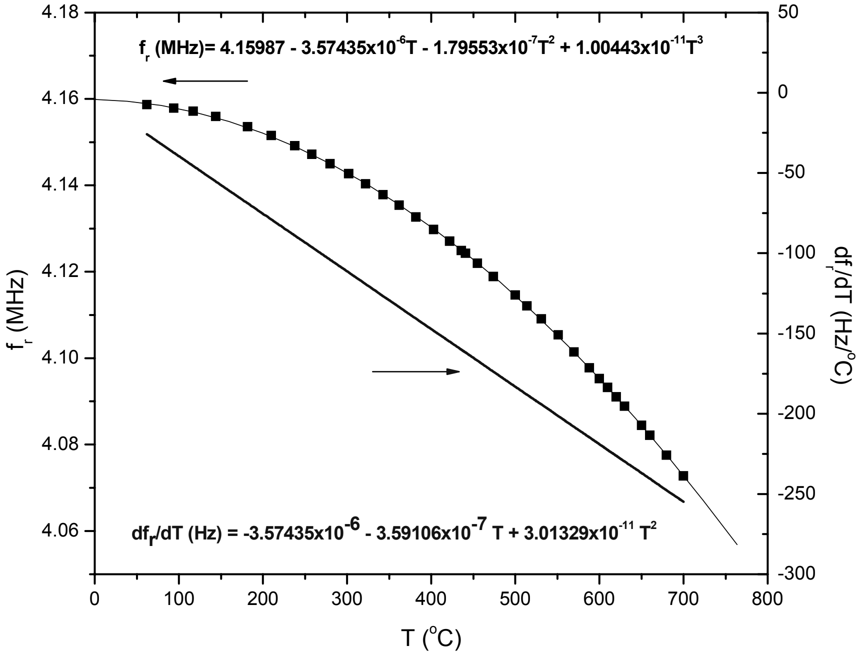

Figure 48: Temperature dependence of resonant frequency of Y-cut langasite resonator.

The changes in resonant frequency Δf (averaged over 10 6-second readings) with time, as pO_2 was varied, are plotted in Figure 49. The time dependent temperature fluctuations are also presented. As there is little correlation between the temperature and the frequency change, we can conclude that the temperature compensation was effective in compensating out most temperature effects.

The frequency shift Δ*f* is replotted as a function of oxygen partial pressure in Figure 50. The smoothed first derivative of that response is also plotted in Figure 50, which shows that the sensitivity of the sensor drops to nearly zero at or below $pO_2=10^{-3}$atm.

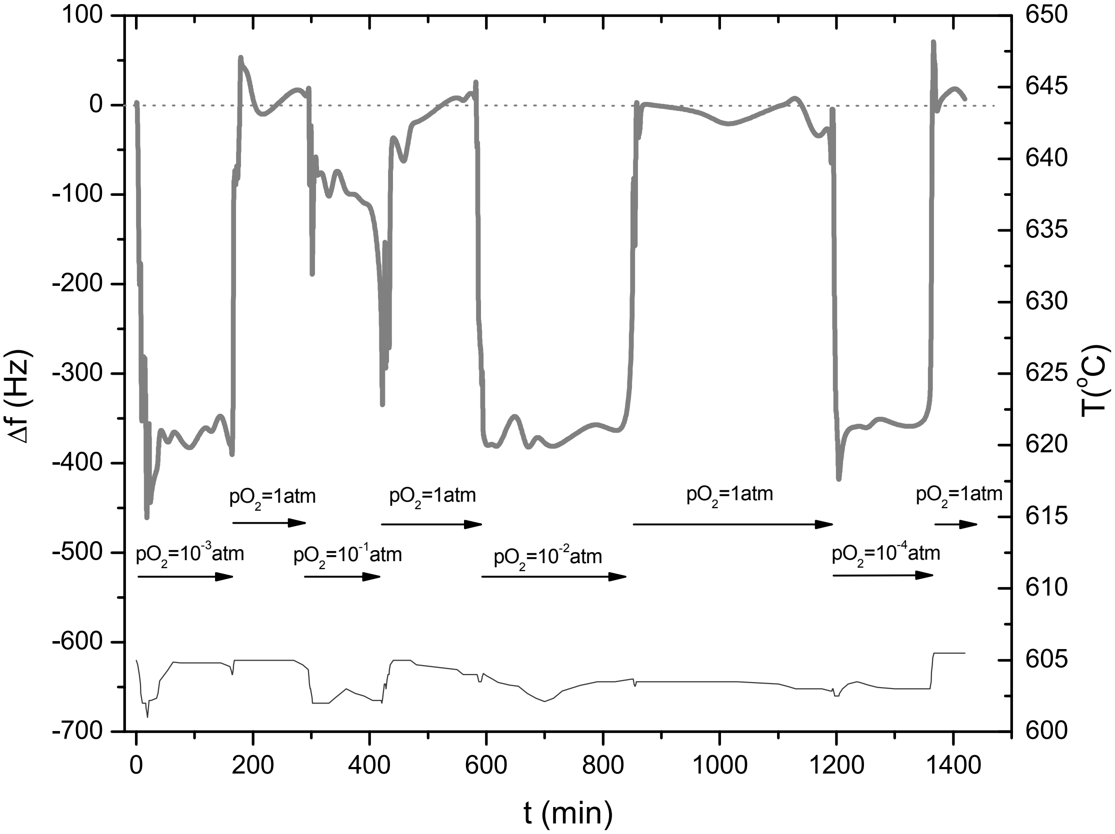

Figure 49: PCO active film on langasite resonator response to oxygen partial pressures. The bottom graph shows that variations in temperature.

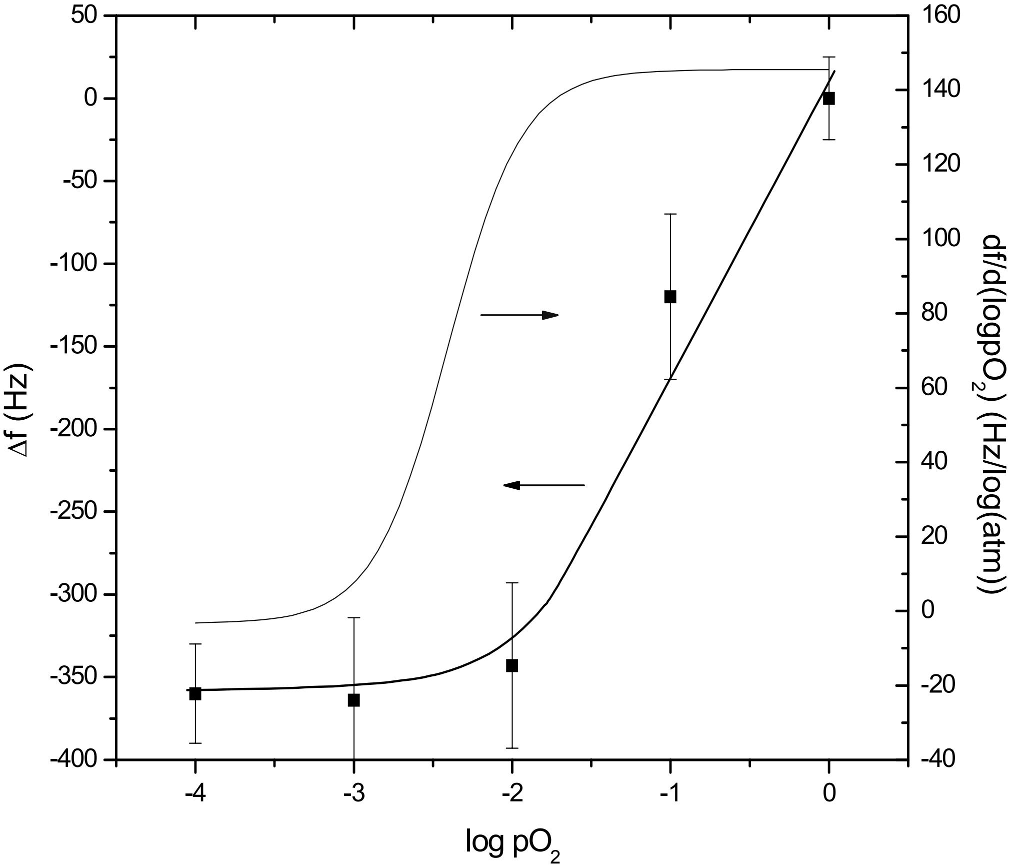

Figure 50: Frequency response of PCO/langasite sensor to pO_2 in the environment.

4.3.2 Sensor Utilizing Reaction Based Film

5MHz AT-cut QCM

Porous active films of $BaCO_3$ were prepared from two different PMMA templates (800 and 400nm diameter PMMA microspheres) on 5MHz AT-cut QCMs. Sensitivity to NO_2 was tested with two different NO_2 concentration (50ppm and 100ppm NO_2 in Ar), with subsequent recovery in a 50/50 CO/CO_2 gas mixture.

The frequency shifts induced in resonators coated with $BaCO_3$ active films (prepared with the 800nm PMMA template) by exposure to 50ppm and 100ppm NO_2 are recorded in Figure 51 and Figure 52 respectively. The corresponding frequency shifts for films prepared using the 400nm PMMA template are shown in Figure 53 and Figure 54, for 50ppm and 100ppm NO_2 respectively. For all sets of data, no frequency shifts are observed below 300^{o}C. The response to a given concentration of NO_2 increases with increasing temperature, up to the maximum test temperature of 400^{o}C. Figure 55 summarizes the temperature dependence of the frequency shifts and incremental sensitivity for the different film microstructures and NO_2 levels. The incremental sensitivity of the sensor between 50 and 100ppm NO_2 as function of temperature was calculated using the following methodology:

1. Sensor response (Δf vs T in Figure 55) for 50 and 100ppm NO_2 concentration was fitted and shown as solid and dotted lines respectively. The Δf for 400nm and 800nm templated films at each NO_2 concentration were fitted as an average.
2. The response curve fit (solid line in Figure 55) of 50ppm NO_2 was subtracted from that of 100ppm NO_2 (dotted line in Figure 55), giving $\Delta f(T)$ per 50ppm NO_2.
3. Dividing that difference, $\Delta f(T)$ per 50ppm NO_2, from (2) with the concentration difference (50ppm), gives incremental sensitivity of the sensor between 50 and 100ppm NO_2, $\Delta f/\Delta[ppm]$.

The negative sensitivity and frequency change observed at all temperatures and for all microstructures are consistent with weight increase as NO_2 reacts with the $BaCO_3$ films.

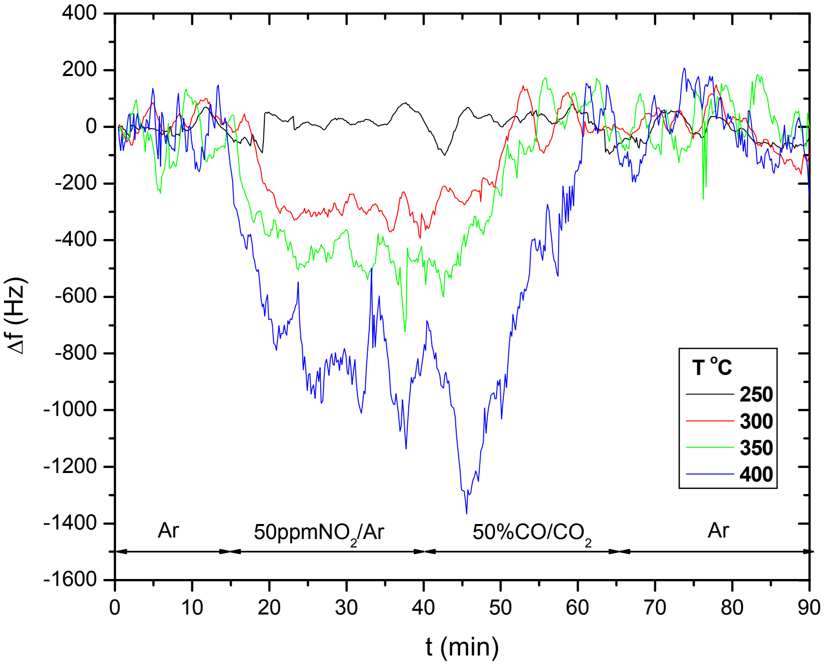

Figure 51: Response of $BaCO_3$ (prepared using 800nm PMMA template) to 50ppm NO_2 at temperatures from 250 to 400°C.

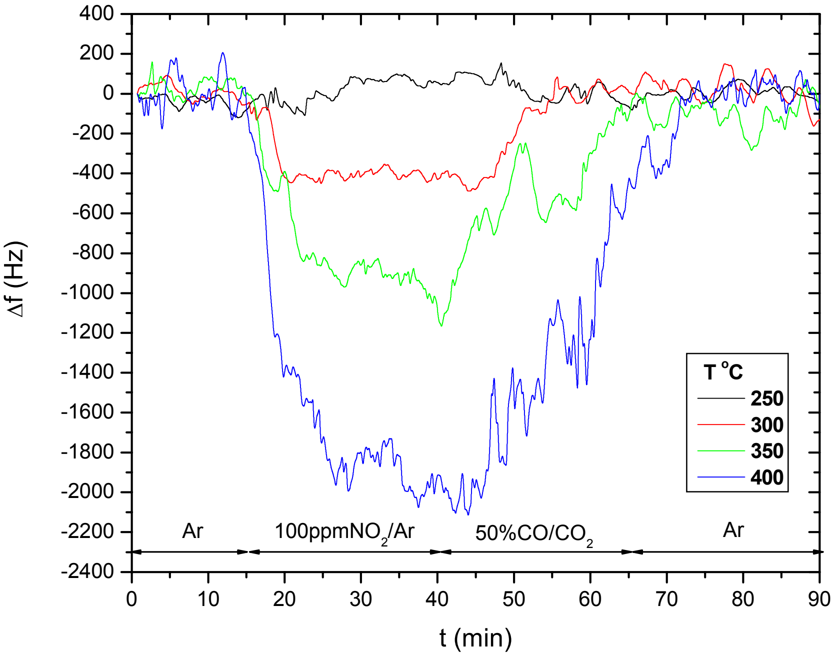

Figure 52: Response of $BaCO_3$ (prepared using 800nm PMMA template) to 100ppm NO_2 at temperatures from 250 to 400°C.

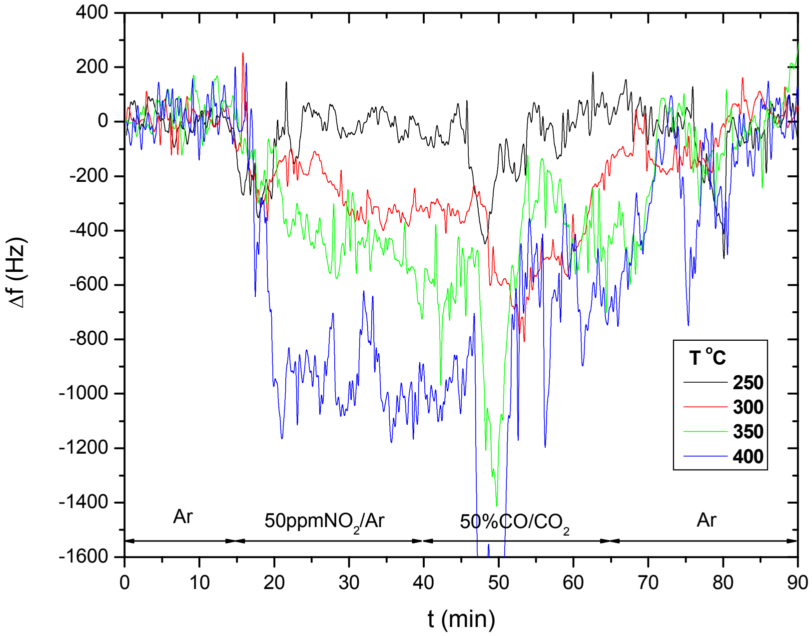

Figure 53: Response of $BaCO_3$ (prepared using 400nm PMMA template) to 50ppm NO_2 at temperatures from 250 to 400°C.

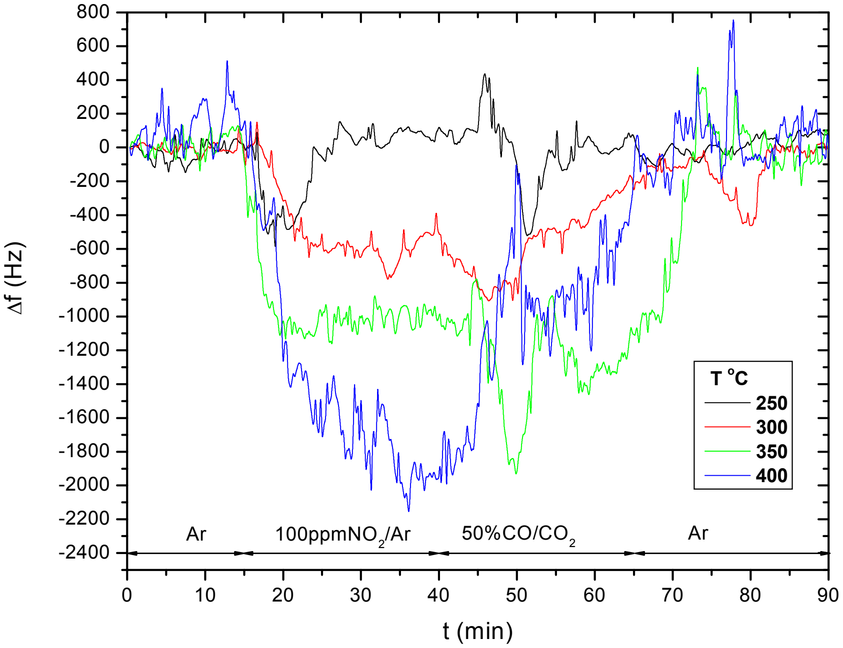

Figure 54: Response of $BaCO_3$ (prepared using 400nm PMMA template) to 100ppm NO_2 at temperatures from 250 to 400°C.

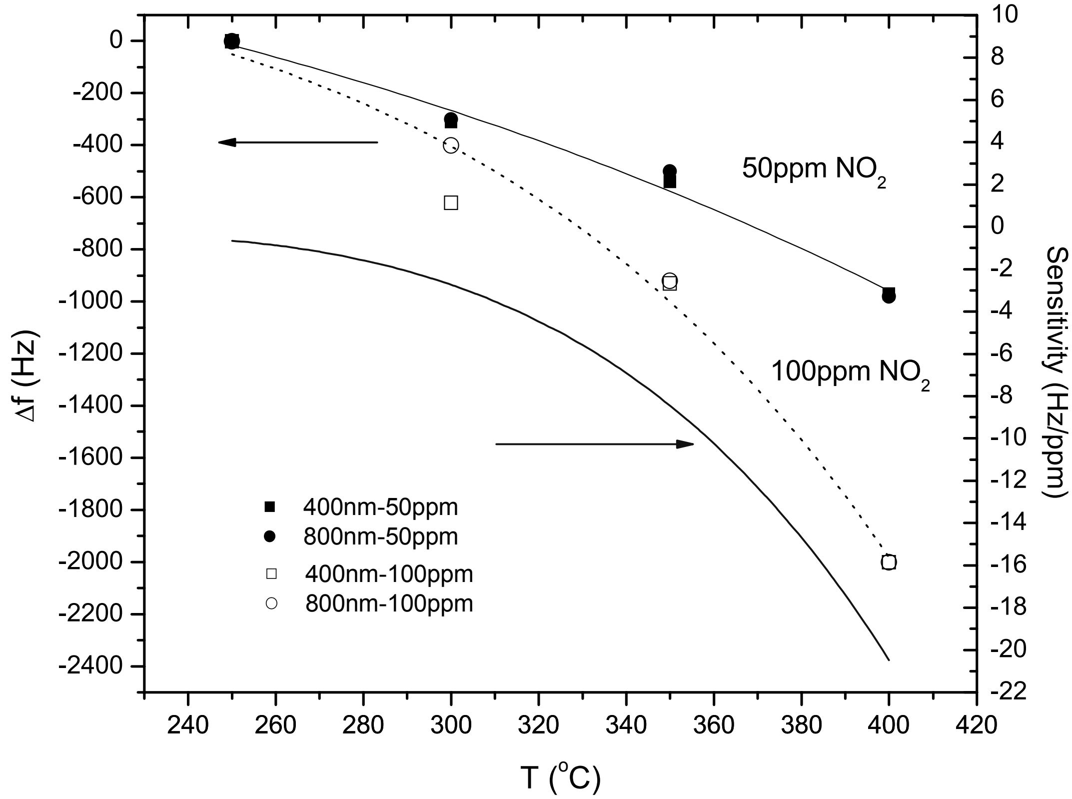

Figure 55: Summary of frequency shifts and incremental sensor sensitivity to NO_2 as function of temperature.

Y-cut Langasite Resonator

Porous active film of $BaCO_3$ was prepared from a 800nm PMMA template on 3.057MHz Y-cut langasite resonator crystal wafer. Sensitivity to NO_2 was tested with two different NO_2 concentrations (50ppm and 100ppm NO_2 in Ar), with subsequent recovery in 50/50 CO/CO_2 gas mixture.

The response of the sensor to 100ppm NO_2 at temperatures ranging from 250 to 750°C is shown in Figure 56. One observes that signal noise increases as temperature increases; at

750°C, the fluctuations in resonant frequency were about ±200Hz. As for the quartz based sensor, full recovery was achieved at all temperatures after exposure to the CO/CO_2 gas mixture. The frequency changes induced by exposure to 100ppm NO_2 are plotted as function of temperature in Figure 57, while the incremental sensitivity between 50 and 100ppm NO_2 (calculated using the same methodology as in the case of quartz resonator, presented previously, p.100) is plotted in Figure 58. Note the sharp increase in response and sensitivity in the vicinity of 400°C.

.

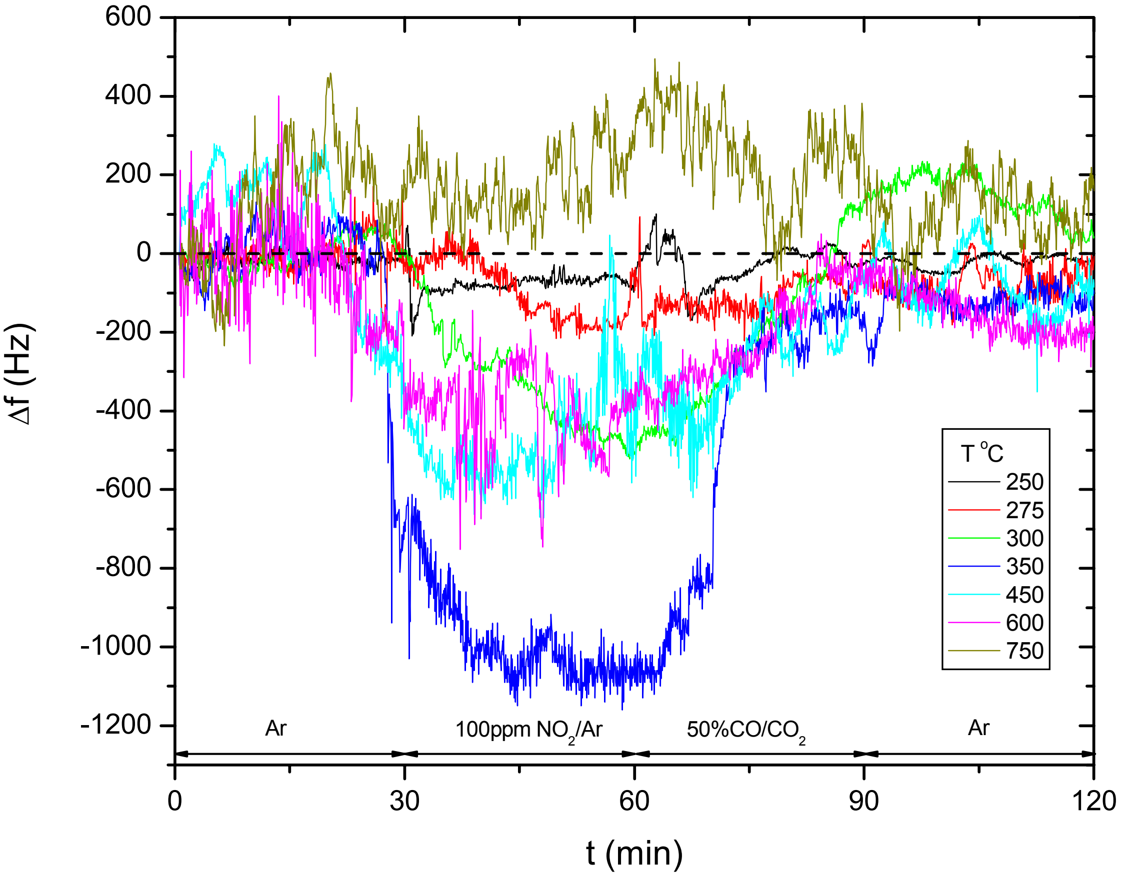

Figure 56: Response of $BaCO_3$ (prepared using 800nm PMMA template) on langasite resonator to 100ppm NO_2 at temperatures from 250 to 750°C.

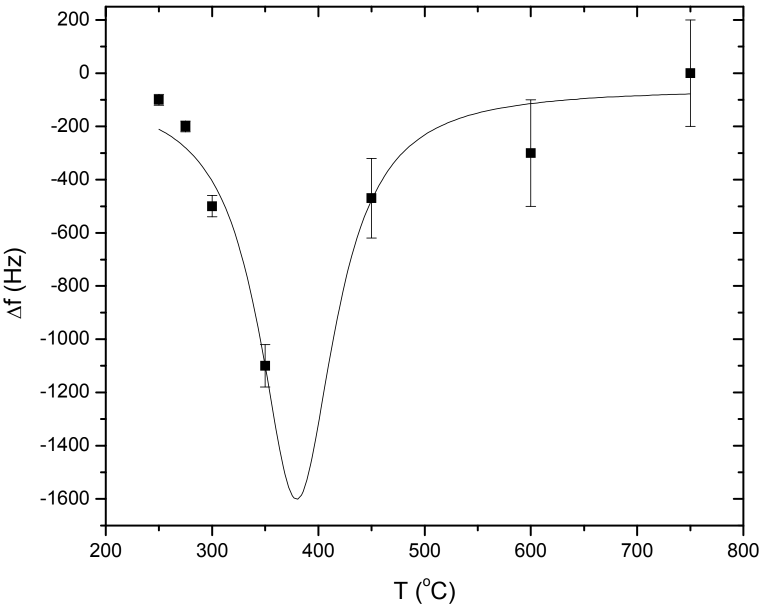

Figure 57: Sensor response to 100ppm NO_2 as function of temperature.

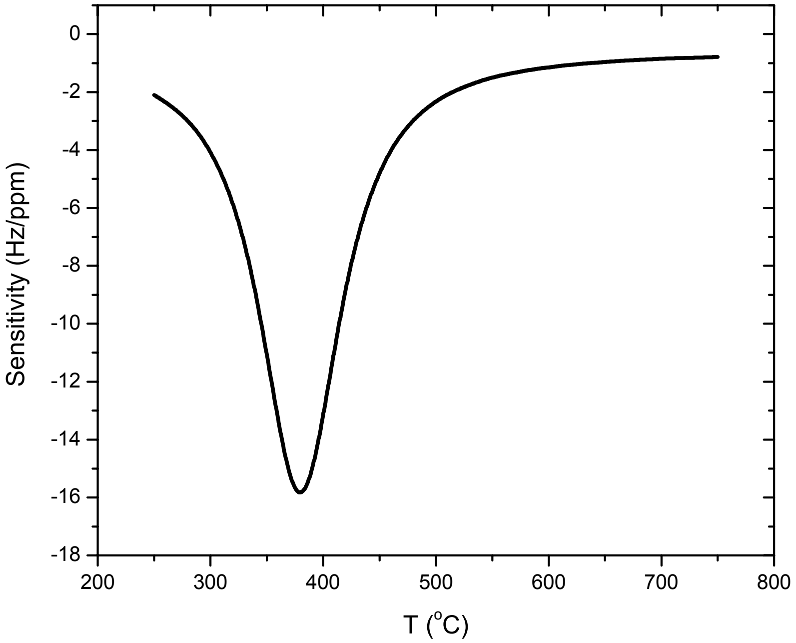

Figure 58: Sensitivity (calculated at 100ppm NO_2) versus temperature curve for the NO_2 sensor based on langasite resonator.

Chapter 5: Discussion

5.1 General

The transport properties of langasite have been systematically studied, within the defect chemistry framework, to provide insights into how temperature, oxygen partial pressure and dopants can affect them. In general, the transport property studies served to identify the dominant mobile electrically charged species for various conditions, and related these findings to the measured diffusion and electrical conductivity data. The model also demonstrated the influences that intentional dopants or unintentional impurities could have on these properties in langasite. This understanding will be applied towards developing a predictable approach for reducing the electrical losses of langasite resonator at high temperature.

The utility of high temperature resonator as mass sensitivity platforms for chemically selective films has been demonstrated. Three examples, representing three general categories of active films were presented, illustrating the possibilities afforded by extending the operating temperature of resonant sensors. The promising high-temperature sensor performance further emphasizes the need for understanding langasite’s defect and transport properties at extreme conditions.

In the following, we discuss results presented in Chapter 4. The transport property data is analyzed using the defect chemical framework, as outlined in Chapter 3. The major experimental findings will be summarized, and a predictive model, which computes electrical conductivity as function of temperature, oxygen partial pressure and dopant levels, will be presented. The impact of langasite’s transport properties on langasite resonator performance and stability will also be discussed.

The sensor data presented in Chapter 4 will be examined and explained in term of non-stoichiometry, surface area, and/or reaction kinetics/thermodynamics, depending on the type of active film. Other crucial issues, e.g. temperature cross-sensitivity, noise and stability, will also be discussed.

5.2 Transport Properties

5.2.1 Acceptor-doped Langasite

Nominally undoped langasite

The bulk electrical data of nominally undoped and 1%Sr-doped langasite, together with the concentration cell measurement, enable us to apply our developed defect model towards explaining the electrical transport properties of acceptor-doped langasite. Nominally undoped langasite exhibited a pO_2-independent conductivity at higher pO_2 and $pO_2^{-\frac{1}{4}}$-dependent electronic conductivity at lower pO_2. As discussed in Chapter 4, this is indicative of an acceptor-doped material in the ionic compensation regime (Region II, as shown in Figure 24 p.76). Using this model, the pO_2-independent conductivity is attributed to conduction by doubly-charged oxygen vacancies ($V_O^{\bullet\bullet}$), and the $pO_2^{-\frac{1}{4}}$-dependent conductivity is attributed to electrons (*e'*).

Therefore, the total conductivity in nominally undoped langasite is:

$$\sigma_{undoped} = 2q\left[V_O^{\bullet\bullet}\right]\mu_{Vo} + nq\mu_e \tag{69}$$

With the oxygen vacancy concentration fixed by the background acceptor, $2\left[V_O^{\bullet\bullet}\right] \approx \left[A'\right]$, we can rewrite Eq. (69):

$$\sigma_{undoped} = q\left[A'\right]\mu_{Vo} + nq\mu_e \tag{70}$$

The different oxygen partial pressure dependence of ions and electrons enabled the deconvolution of the contributions from electrons and oxygen vacancies. This in turn enabled the ionic transference number to be calculated by taking the ratio of the ionic conductivity to the total conductivity. Further confirmation of the defect model was provided by the close agreement obtained for the oxygen partial pressure dependence of the ionic transference number from an analysis of the conductivity measurements and the concentration cell measurements (see Figure 45, p.94).

The nominally undoped langasite is hence shown to be a mixed electronic-ionic conductor with background acceptor impurities. The activation energies for the ionic conductivity-temperature product and electronic conductivity, derived in Chapter 4 (Figure 25 and Figure 27), were found to be 0.91(±0.01) and 3.0(±0.02)eV respectively. These experimentally derived activation energies can now, with the assistance of the defect model, be readily correlated to enthalpies of defect generation and transport. For example, Table 3 (p.51) shows that in Region II of the defect model for acceptor-doped langasite, the activation energy for electron generation equals ½E_r (half of reduction enthalpy) plus electron migration energy E_{μ_e}, while that for oxygen vacancy generation is zero since the vacancy concentration is fixed by the acceptor level.

As activation energy of conductivity consists of both the defect formation and migration energies. Thus for the electronic conductivity (see Figure 27, p.78):

$$E_{\sigma_e} = \tfrac{1}{2}E_r + E_{\mu_e} = 3.0(\pm 0.02)eV \qquad (71)$$

Values for the migration energy for electrons were determined from measurements on Nb doped langasite in which E_{μ_e} was found to be 0.15(±0.01)eV (see Figure 40, p.89). Consequently, one derives a value for the reduction enthalpy of

$$E_r = 5.70(\pm 0.06)eV \qquad (72)$$

Since the formation enthalpy for vacancies in this defect regime is zero, then:

$$E_{\sigma_i T} = E_{\mu_{Vo}} = 0.91(\pm 0.01)eV \qquad (73)$$

where $E_{\mu_{Vo}}$ is the migration energy for oxygen vacancies.

Estimation of oxygen vacancy mobility

We now proceed to estimate the oxygen vacancy mobility. Na was determined to be a major impurity specie (with concentration of 1.5×10^{19} cm^{-3}, see Appendix B) in nominally undoped langasite. It acts as an acceptor on La site (see Appendix B) and, in ionic conductivity regime, should produce the same concentration of oxygen vacancy (according to Brouwer approximation $Na_{La}^{''} \approx V_O^{\bullet\bullet}$). The ionic conductivity of nominally undoped langasite, contributed by oxygen vacancy, was determined and presented in Figure 25 (p.77). With the ionic conductivity and information on oxygen vacancy concentration, oxygen vacancy mobility can be calculated. The oxygen vacancy mobility is plotted as function of temperature in Figure 59.

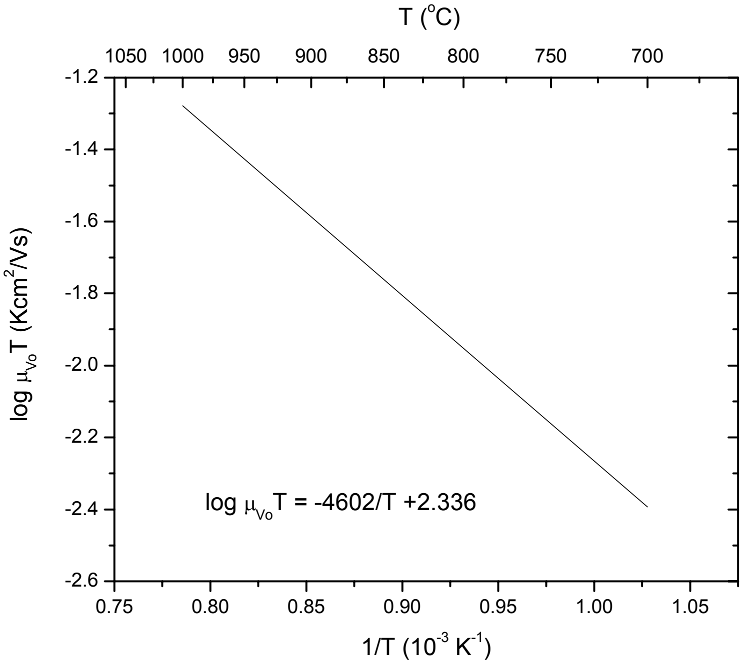

Figure 59: Oxygen vacancy mobility-temperature product plotted as function of temperature.

Figure 59 shows that the activation energy for the oxygen vacancy mobility-temperature product is 0.91(±0.01) eV (which is equal to ionic migration energy of nominally undoped langasite, Eq. (73), p.109). The calculated oxygen vacancy mobility equation is:

$$\mu_{Vo}(T) = \frac{217}{T}\exp\left(-\frac{0.91(\pm0.01)eV}{kT}\right) \quad cm^2/Vs \tag{74}$$

Sr-doped langasite

Acceptor doping by Sr increases the pO_2-independent conductivity and p-type $pO_2^{+\frac{1}{4}}$-dependent electronic conductivity at higher pO_2, while at the same time totally depressing the n-type $pO_2^{-\frac{1}{4}}$-dependent conductivity. This is consistent with the assertion that the electrical properties of undoped langasite are dominated by background acceptor impurities.

Like nominally undoped langasite, 1%Sr-doped langasite is found to be a mixed electronic-ionic conductor. The experimentally observed pO_2 dependence of the conductivity places it in the ionic acceptor compensation regime (Region II, as shown in Figure 24 p.76). Only in this case, the electronic conductivity comes from holes at high pO_2 rather than electrons at low pO_2. The total conductivity is therefore the sum of the ionic and hole conductivity:

$$\sigma_{doped} = q\left[Sr_{La}^{'}\right] \mu_{Vo} + pq\mu_h \tag{75}$$

In Chapter 4, the activation energies of the ionic conductivity-temperature product and hole conductivity are determined to be 1.27(±0.02)eV (Figure 30) and 1.09(±0.04)eV (Figure 32) respectively. The activation energy for hole conduction should equal half the oxidation enthalpy plus the hole migration energy:

$$E_{\sigma_h} = \tfrac{1}{2} E_o + E_{\mu_h} = 1.09(\pm 0.04) eV \tag{76}$$

Since we have no independent information, we will assume that holes move through the lattice in a nonactivated manner, and thus the oxidation enthalpy is given by:

$$E_o \cong 2.18(\pm 0.08) eV \tag{77}$$

Note that the activation energy of the ionic conductivity-temperature product in 1%Sr-doped langasite exceeds that in nominally undoped langasite by 0.36(±0.03)eV (1.27±0.02 vs 0.91±0.01eV). One possible explanation for the disparity between the activation energy of ionic conductivity-temperature product in 1%Sr-doped and undoped samples is defect association [142, 149], in which oppositely charged defects (i.e. $V_O^{\bullet\bullet}$ and $Sr_{La}^{'}$) form defect pairs such as $(Sr_{La}^{'} - V_O^{\bullet\bullet})^{\bullet}$. Under these circumstances, only the dissociated defects contribute to conduction. One can describe the dissociation reaction by:

$$(Sr_{La}^{'} - V_O^{\bullet\bullet})^{\bullet} \leftrightarrow Sr_{La}^{'} + V_O^{\bullet\bullet} \tag{78}$$

with the corresponding mass action relation given by[6]:

$$K_{assoc} = \frac{[Sr_{La}^{'}][V_O^{\bullet\bullet}]}{[(Sr_{La}^{'} - V_O^{\bullet\bullet})^{\bullet}]} = k_{assoc} \exp\left(-\frac{E_{assoc}}{kT}\right) \tag{79}$$

The following mass conservation law applies:

$$[Sr_{total}] = [Sr_{La}^{'}] + [(Sr_{La}^{'} - V_O^{\bullet\bullet})^{\bullet}] \tag{80}$$

The following electroneutrality also applies:

$$[Sr_{La}^{'}] = 2[V_O^{\bullet\bullet}] + [(Sr_{La}^{'} - V_O^{\bullet\bullet})^{\bullet}] \tag{81}$$

Substituting Eq.(80) into Eq.(79), gives:

$$K_{assoc} = \frac{[V_O^{\bullet\bullet}][Sr_{La}^{'}]}{[Sr_{total}] - [Sr_{La}^{'}]} = k_{assoc} \exp\left(-\frac{E_{assoc}}{kT}\right) \tag{82}$$

It is useful to examine the predictions of this model at the extremes of low and high temperature, i.e., very low dissociation and nearly full dissociation. For a high degree of association at low temperatures, based on Eq.(81):

$$[Sr_{La}^{'}] \cong [(Sr_{La}^{'} - V_O^{\bullet\bullet})^{\bullet}] \tag{83}$$

Substituting this expression into Eq.(79) results in the following expression for the unassociated oxygen vacancy concentration (see Regime III in Figure 60):

---

[6] Since the unit for concentration is cm^{-3} (used throughout this thesis), the dimension of k_{assoc} is cm^{-3}.

$$[V_O^{\bullet\bullet}] = k_{assoc} \exp\left(-\frac{E_{assoc}}{kT} \right) \qquad (84)$$

On the other hand, at high enough temperature, dissociation becomes nearly complete (Regime I in Figure 60) and then Eq. (81) becomes:

$$[Sr_{La}^{'}] = 2[V_O^{\bullet\bullet}] \cong [Sr_{total}] \qquad (85)$$

Thus, the vacancy concentration is predicted to shift from an activated process at low temperature to a constant value at high temperature. In the transition from the low to high temperature regime, one expects to observe curvature in the $\log[V_O^{\bullet\bullet}]$ vs 1/T plot (Regime II in Figure 60).

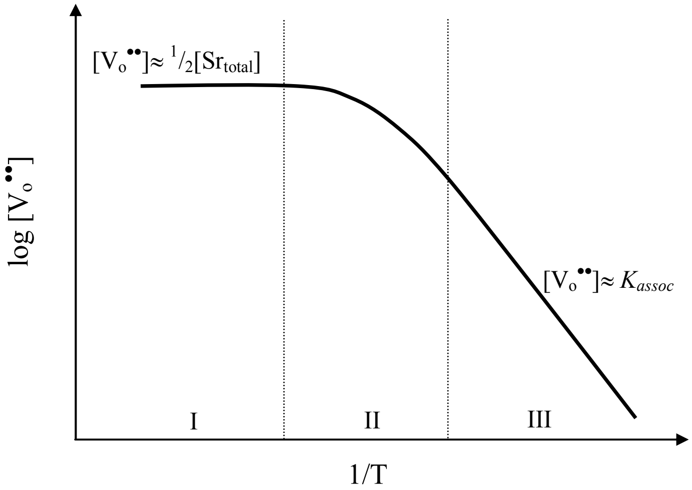

Figure 60: Dissociated oxygen vacancy concentration as function of reciprocal temperature. In Regime I, defects are nearly completely dissociated while in Regime III, defects are nearly fully associated.

The disparity between the activation energy of ionic conductivity-temperature product in 1%Sr-doped and undoped langasite (1.27±0.02 vs 0.91±0.01eV) could in principle be attributed to defect association as discussed above. Indeed, we can calculate the ionic conductivity of 1%Sr-doped langasite assuming that defect association is the correct explanation for the larger activation energy. To do that, we define x as:

$$x = \frac{[V_O^{\bullet\bullet}]}{[Sr_{total}]} \qquad (86)$$

Using Eq. (80) and (81):

$$x + \frac{1}{2} = \frac{[Sr_{La}^{'}]}{[Sr_{total}]} \tag{87}$$

Substituting Eq.(86) and (87) into Eq.(82):

$$K_{assoc} = \frac{x\left(x + \frac{1}{2}\right)}{\frac{1}{2} - x}[Sr_{total}] = k_{assoc} \exp\left(-\frac{E_{assoc}}{kT}\right) \tag{88}$$

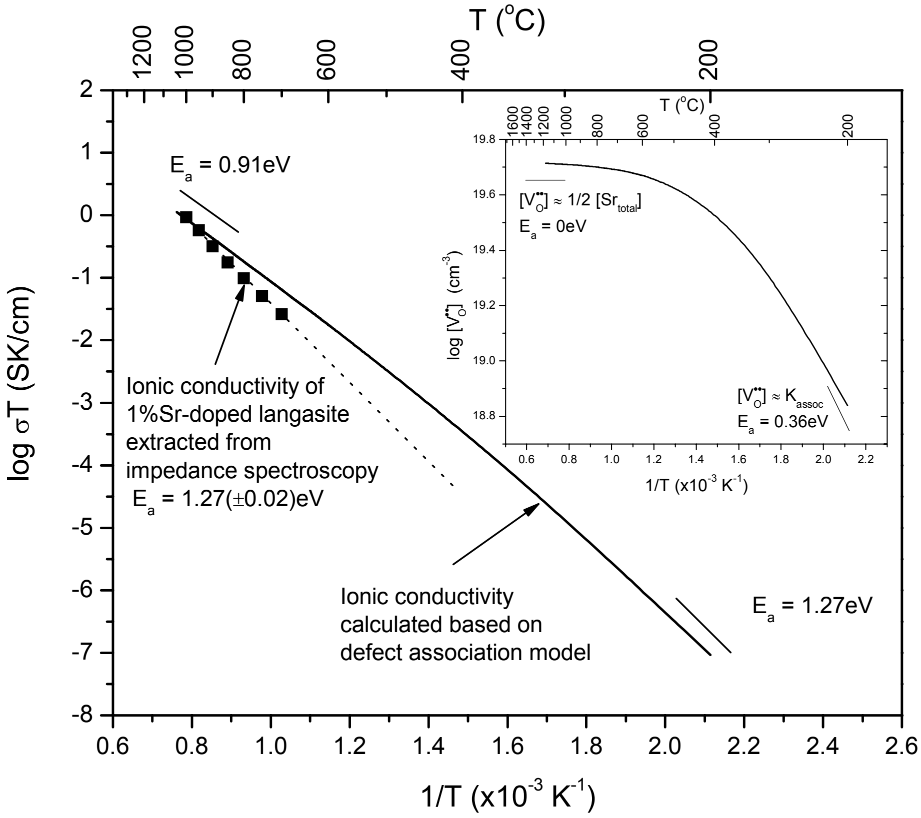

Figure 61: Ionic conductivity-temperature product plot of 1%Sr-doped langasite – comparison between extracted values from impedance spectroscopy and calculated values (with insert showing the calculated $[V_O^{\bullet\bullet}]$) assuming a defect association model.

The pre-exponential k_{assoc} is defined as the product of degree of freedom of the defect pair and the number of oxygen lattice sites in langasite (~1.7×10^{23}cm^{-3}) [141, 142, 149], and the E_{assoc} is 0.36(±0.03)eV (see Eq. (84)), which is the difference in activation energy for ionic conductivity-temperature product between 1%Sr-doped and nominally undoped langasite. Solving Eq. (88) gives us the concentration of unassociated oxygen vacancies (see insert, Figure 61) and, with the oxygen mobility derived in Eq. (74) (p.110), the ionic conductivity that is based on the defect association model can be calculated (Figure 61). From Figure 61, it can be seen that for the temperature range examined in the conductivity measurements (700-1000°C), the defect pairs would be largely dissociated (Regime I in Figure 60) and the activation energy should only reflect the oxygen vacancy migration energy (0.91eV). In order to observe E_{assoc} of 0.36eV (for a total activation energy of 1.27eV as seen in the case of 1%Sr-doped langasite), its conductivity would have to be measured at temperatures below 300°C. Therefore, defect association cannot explain the disparity between the activation energy of ionic conductivity-temperature product in 1%Sr-doped and undoped langasite.

The alternative explanation for the larger activation energy for oxygen ion conductivity in 1%Sr-doped langasite can be explained on the basis of the failure of the dilute solution approximation at the 1% Sr level. For concentrated solutions, long range defect interactions must be taken into account. Wang et al [150], for example, observed that the activation energy for oxygen ion conductivity in Y_2O_3 doped CeO_2 increased systematically as the yttrium content increased from 1 to 40 mol%. In this and other fluorite and pyrochlore systems [151-153] this has been attributed to long range defect ordering which serves to create deeper potential wells for the oxygen vacancies to overcome as they move through the lattice. This would explain the higher activation energy for ionic conductivity-temperature product (i.e. the $V_O^{\bullet\bullet}$ migration energy) in 1%Sr-doped langasite when compared to nominally undoped langasite which remains in dilute solution.

Diffusion studies on acceptor-doped langasite

The activation energy of oxygen vacancy mobility can be verified from the results of oxygen exchange diffusion studies. Schulz et al [146] measured the oxygen self diffusivity of 1%Sr-doped and undoped langasite and obtained activation energies of

1.1eV and 1.4eV respectively. The activation energy of the mobility- temperature product, $\mu_v T$, and the self-diffusivity, D, should be identical, as suggested by Nernst-Einstein equation [142]:

$$\frac{D}{kT} = \frac{\mu_v}{Zq} \tag{89}$$

The diffusivity is relation to self diffusivity through:

$$D = \frac{D_{self}}{M_v} \tag{90}$$

where M_v is the mole fraction of vacancy, and D_{self} is the diffusivity we observed in the oxygen exchange experiment.

Substituting Eq.(90) into (89):

$$\frac{D_{self}}{M_v kT} = \frac{\mu_v}{Zq} \tag{91}$$

In the case of 1%Sr-doped langasite, the activation energy for conductivity-temperature product of 1.27(±0.02)eV and the oxygen self-diffusion activation energy of 1.1eV are close indeed. The self-diffusion data also shows that oxygen diffusion in 1%Sr-doped langasite is about one order of magnitude higher than that of undoped langasite (Figure 47, p.96). However, for nominally undoped langasite, the disparity between the mobility-temperature (0.91±0.01eV) and self-diffusion activation energies (1.4eV) is about 0.5eV. However, it should be noted that the data for nominally undoped langasite consists only of two points[7]; the activation energy derived from these data should therefore be viewed as suspect.

Referring again to Figure 47, it is clear that the addition of Sr increases the oxygen diffusivity by an order of magnitude, similar to the effect on the electrical conductivity of

---

[7] Due to the existing pores in polycrystalline langasite, it was difficult to obtain good oxygen-18 profile. This also resulted in higher uncertainty in the oxygen diffusivity data for polycrystalline langasite.

adding Sr to nominally undoped langasite. One can express the ionic conductivity with the aid of the Nernst-Einstein equation (noting that $M_V = [V_o^{\bullet\bullet}]/[O_o^x]$):

$$\sigma_{Vo} = \frac{Zq^2}{kT}[O_o^x]D_{self} \tag{92}$$

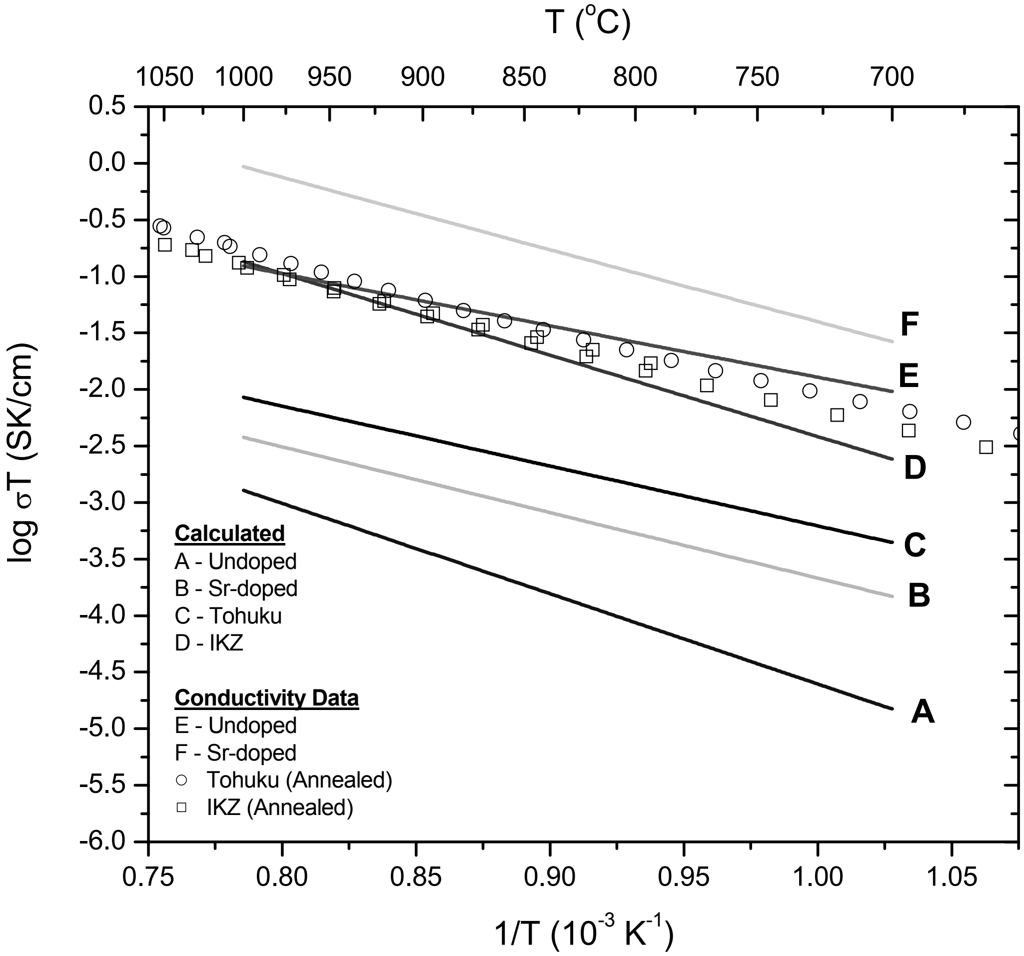

Figure 62: Ionic conductivity-temperature product plot of langasite (single crystals and polycrystalline samples). Calculated values (A-D) are derived from oxygen self diffusion measurements with the aid of Nernst-Einstein Equation. Ionic conductivity values for 1%Sr-doped and undoped langasite extracted from the impedance measurements are plotted for comparison. The measured conductivity values from [154] for single crystal samples are also included (represented by ○ and □).

The self diffusivity data is then converted to conductivity data by use of Eq. (92) ($[O_o^x] \approx 4.76\times10^{22}$ cm^{-3} from the langasite crystal structure) (see Figure 62). It can be seen that the calculated values using diffusion data for both 1%Sr-doped and nominally undoped langasite are systematically lower (by about 2 orders of magnitude) than the measured conductivity values. On the other hand, ionic conductivities derived from diffusion measurements performed on single crystal langasite (see curve D in Figure 62) are much closer to measured conductivity values. Furthermore, Fritze et al [154] measured the conductivity of single crystal samples after annealing at 1050°C for several hours; their conductivities were remarkably similar to the measured conductivity of nominally undoped polycrystalline langasite (see Figure 62, curve E). The large discrepancy in magnitude between measured and diffusion-derived conductivity data for polycrystalline specimens points to the difficulties in accurately fitting diffusion data for polycrystalline samples where grain boundaries and porosity interfere with the analyses.

While the experimental data (conductivity, concentration cell and oxygen diffusivity) are generally consistent with the ionic conductivity being largely due to the motion of oxygen ions, there remains the possibility of another charged mobile specie contributing to the ionic conductivity. Out of the 3 cations in the langasite crystal structure, Ga is suspected due to its smaller size and ionicity. Si is, in general, covalent and La is large, making both species unlikely to easily migrate within the structure. Ga diffusion measurements were also performed by Schulz et al. [146] on single crystal langasite. The results show that gallium diffusion is orders of magnitude lower than oxygen diffusion and so can be dismissed with respect to ionic conductivity contributions (Figure 47, p.96).

Stability of langasite

The reversibility of electrical measurements, low cation diffusion and reports in the literature suggest that langasite remains stable even at high temperature. To examine langasite's stability, particularly under highly reducing conditions, nominally undoped langasite powder, providing relatively high surface area, was annealed in 5%H_2/Ar at 1000°C for 2 days. No observable second phase could be observed by X-ray diffraction.

This further reinforces the notion that langasite remains stabile under extreme conditions (as described in section 1.3).

Reduction and oxidation constants: K_r and K_o

For nominally undoped langasite, electron density *n* at pO_2=1atm can be calculated from the electron mobility (Figure 43, p.92) and extrapolating its n-type electronic conductivity. The calculated *n* at pO_2=1atm as function of temperatures is shown in Figure 63.

K_r can be related to *n*, pO_2 and dopant level (Table 3, Region II, p.51) for acceptor-doped langasite. With calculated *n* at pO_2=1atm above and known dopant level (for nominally undoped langasite, the background acceptor is Na at 1.5×10^{19}cm^{-3}, see Appendix B), K_r function for acceptor-doped langasite is established:

$$K_r = 10^{67} \exp\left(-\frac{5.7 \pm 0.06eV}{kT}\right) \quad cm^{-9} atm^{0.5} \tag{93}$$

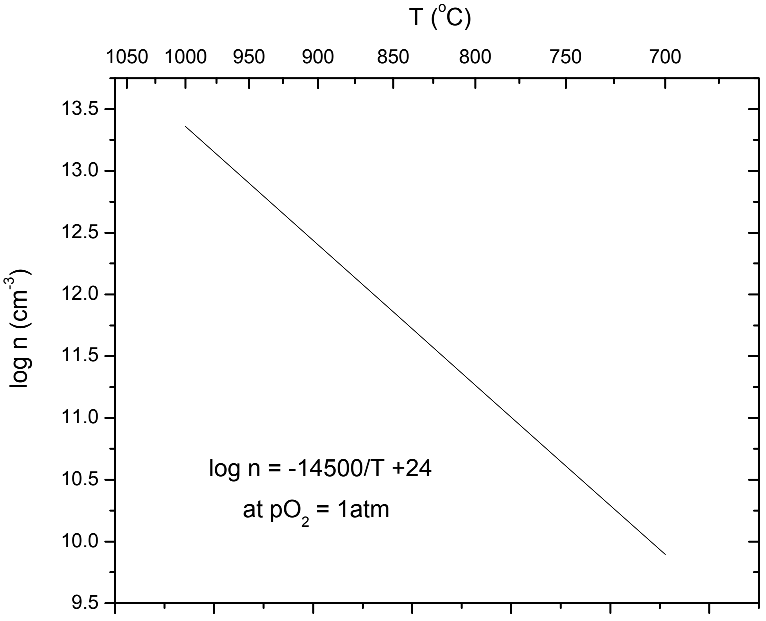

Figure 63: Electron density of nominally undoped langasite at pO_2=1atm as function of temperature.

By adding reduction and oxidation reactions, i.e. Eq.(39)+Eq.(41) (p.47), the resultant reaction would be simply twice of generation reaction, Eq.(37). The mass action laws relationship will be $K_e = (K_r K_o)^{0.5}$. And as k_r is now known from Eq.(93) and k_e is simply $N_v N_c$, where N_v and N_c are the density of states for hole and electron respectively, k_o can be determined subsequently.

With the hole mobility assumed to be nonactivated, it follows that the semiconductor model for the density of states (as described in, for example, [155]) can be applied:

$$N_v = 2.5\left(m_h^* \frac{T}{300K} \right)^{\frac{3}{2}} \times 10^{19} cm^{-3} \tag{94}$$

where m_h^* is the effective mass of hole (which is usually 2-10 in oxides [142]) and T is the temperature in kelvin. Using the equation, N_v can be estimated (assuming $m_h^* \approx 2$ and $T \approx 1000$) to be about 4×10^{20} cm^{-3}.

Electron mobility in langasite is activated and is described by polaron hopping. The density of state for electron is, therefore, the lattice site density. In order to decide which cation lattice site electrons utilized during activated hopping, the bandgaps of the individual constituent oxides were examined. The bandgaps of La_2O_3, Ga_2O_3 and SiO_2 are reported to be 5.5eV[156], 4.9eV[157] and 9.0eV[158] respectively. The most likely cation lattice sites the electrons utilize for hopping is the one with the lowest energy level, which is the Ga lattice in this case. The density of states for electron, N_c, in langasite is therefore:

$$N_c = Ga - sites = 1.7 \times 10^{22} cm^{-3} \tag{95}$$

The value for k_e ($=N_c N_v$) is calculated to be 6.8×10^{42} cm^{-6} and k_o can be estimated to be 4.6×10^{18}cm^{-3}atm$^{-0.5}$. The K_o function for acceptor-doped langasite is then:

$$K_O = 4.6 \times 10^{18} \exp\left(-\frac{2.18 \pm 0.08 eV}{kT} \right) \quad cm^{-3} atm^{-0.5} \tag{96}$$

Estimation of hole mobility

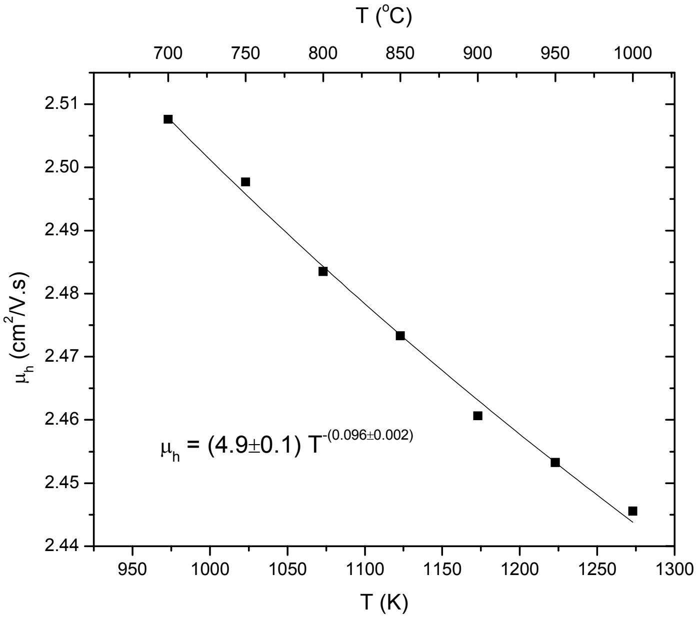

Figure 64: Hole mobility as function of temperature.

The hole density, *p*, can be determined using the equation given in Table 3, Region II (p. 51). Since the hole conductivity of 1%Sr-doped langasite is known (Figure 31, p.82), hole mobility can be calculated and is plotted in Figure 64. The decrease in hole mobility with temperature is due to increased scattering at higher temperatures. If the log of hole mobility is plotted vs 1/T, the activation energy would be very small and negative (about -0.01eV), which is consistent with the assumption made above that hole mobility is nonactivated.

5.2.2 Donor-doped Langasite

Nb-doped langasite

The bulk electrical conductivity data of 5%Nb-doped langasite, together with the TEP and concentration cell measurements, enable us to apply a defect model in explaining the electrical transport properties of donor-doped langasite. As briefly discussed in Chapter 4, the conductivity data for 5%Nb-doped langasite falls within defect Regions I and II of donor-doped langasite, with the electronic conductivity (electrons) dominating throughout. The dominant electronic conductivity is confirmed also by concentration cell measurements, which confirm that $t_i \approx 0$ (Figure 46, p.95).

The activation energy at the pO_2-independent regime of Figure 33 (p.83) is found to be 0.91(±0.01) eV (Figure 35). According to Table 4 (p.54), n is fixed by the ionized donor concentration. Due to the high activation energy, it was deemed highly unlikely that the electron mobility migration energy would be the sole contributor to that activation energy. Alternatively, if the donor level is deep and therefore are not fully ionized, then the activation energy would represent the sum of electron migration energy and half the donor ionization energy[8] (Eq. (46), p.48). This hypothesis was confirmed by the TEP results, which demonstrated that n ($n \approx [D^{\cdot}]$) is a strong function of temperature even in the pO_2 plateau region.

The donor ionization energy can be obtained from TEP measurements (Figure 39, p.89). The ionization reaction is presented in Eq. (45) (p.48), with the mass action law in Eq. (46). The activation energy (0.76±0.03 eV) from Figure 39 therefore represents half the donor ionization energy; the donor ionization energy is 1.52(±0.06)eV, indicating Nb as a deep donor. With the ionization energy, the electron mobility energy is calculated to be 0.15(±0.01)eV, a value which is typically associated with polaron hopping. The electron mobility is shown to be independent of pO_2 and only dependent on temperature as shown in Figure 43 (p.92); the calculated n from conductivity (using electron mobility values in air) as function of pO_2 fit well with n obtained from TEP measurements taken over a range of pO_2.

The $pO_2^{-\frac{1}{6}}$-dependent regime is dominated by the reduction reaction (Eq.(39), p.47) and the activation energy in this regime represents the electron migration energy plus 1/3 of the reduction enthalpy (see Region I in Table 4, p.54). Note that the activation energy was calculated far from the transition to ensure that ionization process was not a significant source of electrons, and the activation energy of conductivity at that regime is

---

[8] It is half the donor ionization energy because of the Brouwer approximation, $n \approx [D^{\cdot}]$.

2.34(±0.07)eV (Figure 36, p.86). The reduction enthalpy for donor-doped langasite is therefore calculated to be 6.57(±0.24)eV, larger than the value obtain for acceptor-doped langasite of 5.7(±0.06)eV. Such difference is not surprising as the high concentrations of added dopants means that deviation from dilute solution approximation is expected. Similar change in reduction enthalpy was observed by Tuller and Nowick [144]. They reported that doping CeO_2 with 5mol% Y_2O_3 (acceptor) decreased the reduction enthalpy from 4.7eV (of undoped ceria) to 4.0eV.

<u>*Calculating K_r for donor-doped langasite*</u>

Given our knowledge of the electron mobility, *n* can be determined from the conductivity data which in turn allows us to check for consistency in the calculation $K_r(T)$. In Figure 36 (p.86), the extrapolated conductivity at $pO_2=10^{-35}$atm is presented as function of temperature. This data is converted into $n(T, pO_2=10^{-35}atm)$, and with the equation in Table 4 (p.54) relating *n* with pO_2, K_r(T); the calculated values of $K_r(T)$ are plotted in Figure 65.

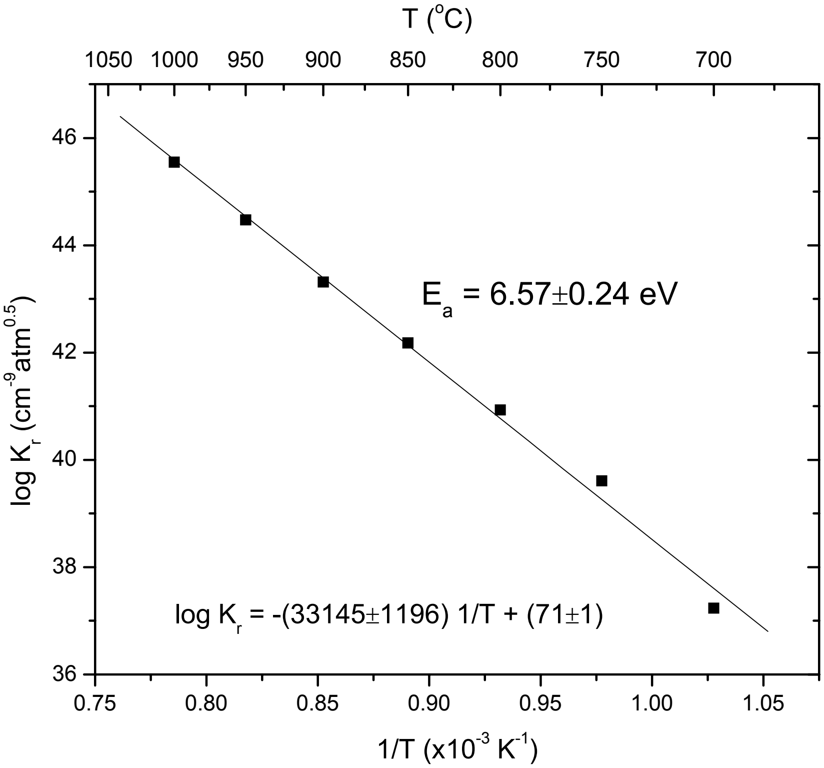

Figure 65: K_r as function of temperature for langasite.

The activation energy for K_r is the reduction enthalpy (Eq. (40), p.47), E_r = 6.57(±0.24)eV, which is identical with result calculated above (E_r = 6.57(±0.24)eV); this was expected since both calculations used the same set of data (i.e. electron mobility and electronic conductivity).

In Chapter 4, we did not describe the process we used to fit the donor electrical conductivity as it involves references to defect model and is more suitable to discuss here after the model has been established. The fitted conductivity curves (dotted lines) in Figure 33 (p.83) are obtained using the following defect analysis:

1. Neutrality equation for the major defects for donor-doped langasite is:

   $$\left[V_o^{\bullet\bullet}\right] = \tfrac{1}{2}\left(n - \left[Nb^{\bullet}\right]\right) \qquad (97)$$

2. The neutrality equation is substituted into the mass action law for reduction process (Eq. (40), p.47), giving:

   $$n^3 - \left[Nb^{\bullet}\right]n^2 - 2K_r pO_2^{-\frac{1}{2}} = 0 \qquad (98)$$

3. In Figure 39, the equation for the electron density of the Nb-doped langasite in air is given. Since in air, $n \approx [Nb^{\cdot}]$, that equation can be rewritten to give the concentration of ionized Nb as function of temperature (and independent of pO_2):

   $$\left[Nb^{\bullet}\right] = k_{Dn}^{\frac{1}{2}} \exp\left(\frac{-E_{D\_ion}}{2kT}\right) = 2.75\times10^{20}\exp\left(-\frac{1.52eV}{2kT}\right) \qquad (99)$$

   $k_{Dn}^{\frac{1}{2}}$ is defined as total donor concentration, Nb_{total}, and is equal to 8.5×10^{20}cm^{-3}, the amount of Nb added. This value is comparable to the pre-exponential, 2.75×10^{20}cm^{-3}, of Eq. (99).

4. With K_r and $[Nb^{\cdot}]$, Eq. (98) allows us to fit the bulk conductivity of donor doped langasite. The reason for not using the simplifying Brouwer approximations (in Table 4, p.54) is that the conductivity data overlaps the transition between the two

defect regions; the Brouwer approximations cannot adequately address the transition region from Region I to II.

The defect models for acceptor and donor-doped langasite presented earlier in the chapter has been verified using independent means such as TEP and concentration cell measurements. This section discusses a few other calculations performed to ensure consistency within the model.

Transition pO₂ for 5%Nb-doped langasite

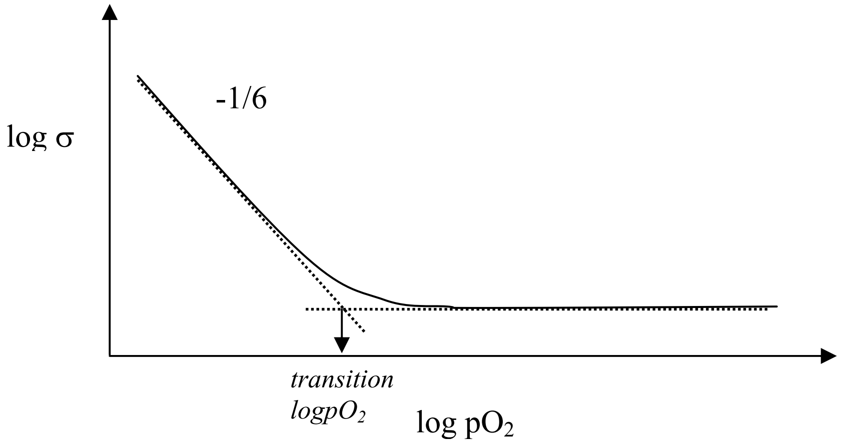

Figure 66: Definition of transition pO₂ for donor doped material.

For the donor doped material, the pO_2 at which the material goes from Region I to II can be used to verify the reduction enthalpy. The transition pO_2 is defined in Figure 66, and it can be viewed as the point at which the contributions to conductivity from the reduction reaction and donors are equal, i.e. electron densities in Region I and II (in Table 4, p.54) are equal:

$$2^{\frac{1}{3}} pO_{2,transition}^{-\frac{1}{6}} k_r^{\frac{1}{3}} \exp\left(\frac{-E_r}{3kT}\right) = k_{Dn}^{\frac{1}{2}} \exp\left(\frac{-E_{D\_ion}}{2kT}\right) \tag{100}$$

Rearranging:

$$\log pO_{2,transition} = -\frac{2E_r - 3E_{D\_ion}}{kT\log e} + \log\left(4k_{Dn}^{-3}k_r^{\ 2}\right) \tag{101}$$

The transition pO_2 for 5%Nb-doped langasite are determined and the values are plotted in Figure 67 as function of reciprocal temperature. The derived activation energy from the plot is 8.62(±0.38)eV, which should correspond to $2E_r$-$3E_{D\_ion}$. As calculated previously, E_r=6.57(±0.24)eV (donor-doped) and E_{D_ion}=1.52(±0.06)eV, giving the value of 8.64(±0.66)eV for $2E_r$-$3E_{D\_ion}$ which is essentially identical to the activation energy obtained in Figure 67.

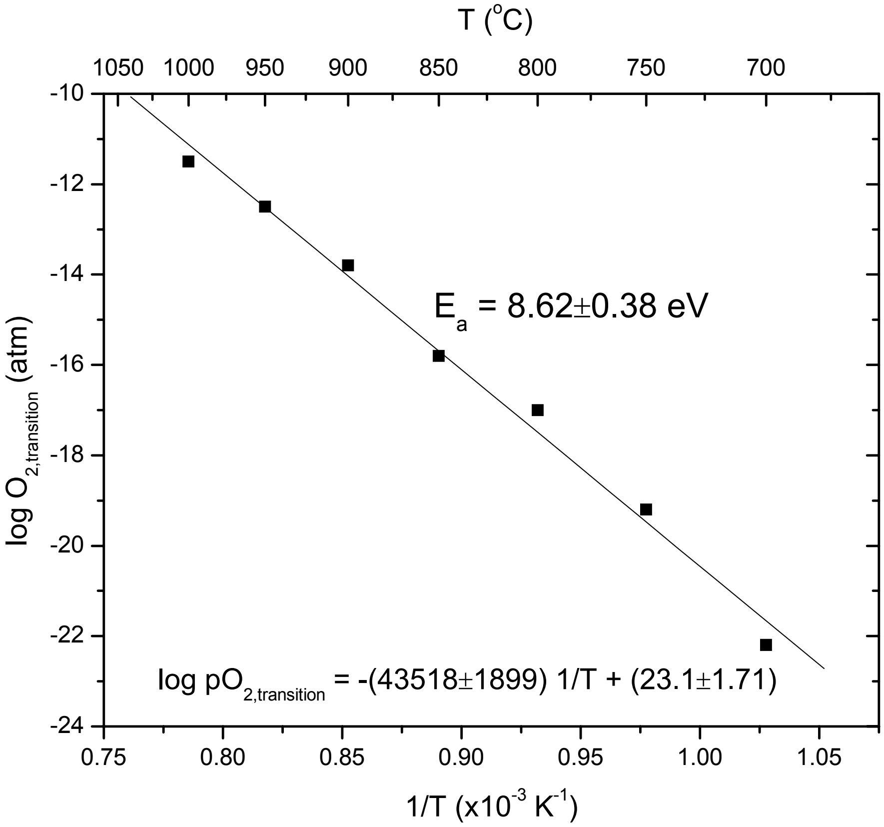

Figure 67: Transition pO_2 at which 5%Nb-doped langasite switches between Defect Region I and II.

We can also verify the consistency of k_r with the intercept of Figure 67 that represents $\log\left(4k_{Dn}^{-3}k_r{}^2\right)$. The $k_{Dn}^{\frac{1}{2}}$ given in Eq.(99) (p.124) is about 10^{20}cm^{-3}, and the log k_r obtained in Figure 65 (p.123) is 71(±1), giving the $\log\left(4k_{Dn}^{-3}k_r{}^2\right)\approx 22$, which is comparable with the intercept value of 23.1 obtained in Figure 67.

Relationship between E_g, E_r and E_o

If the reduction and oxidation reactions are added together, i.e. Eq.(39)+Eq.(41) (p.47), they gave:

$$null \rightarrow 2h^{\bullet} + 2e^{'} \tag{102}$$

which suggests that the sum of enthalpies of reduction and oxidation is equal to twice the thermal bandgap of the material, i.e.:

$$E_r + E_O = 2E_g \tag{103}$$

We have derived the reduction and oxidation enthalpy of langasite, E_r=5.7(±0.06)eV (acceptor) or 6.57(±0.24)eV (donor) and E_o=2.18(±0.08)eV, which an estimated E_g (thermal bandgap) that ranges from 4.0 to 4.4eV.

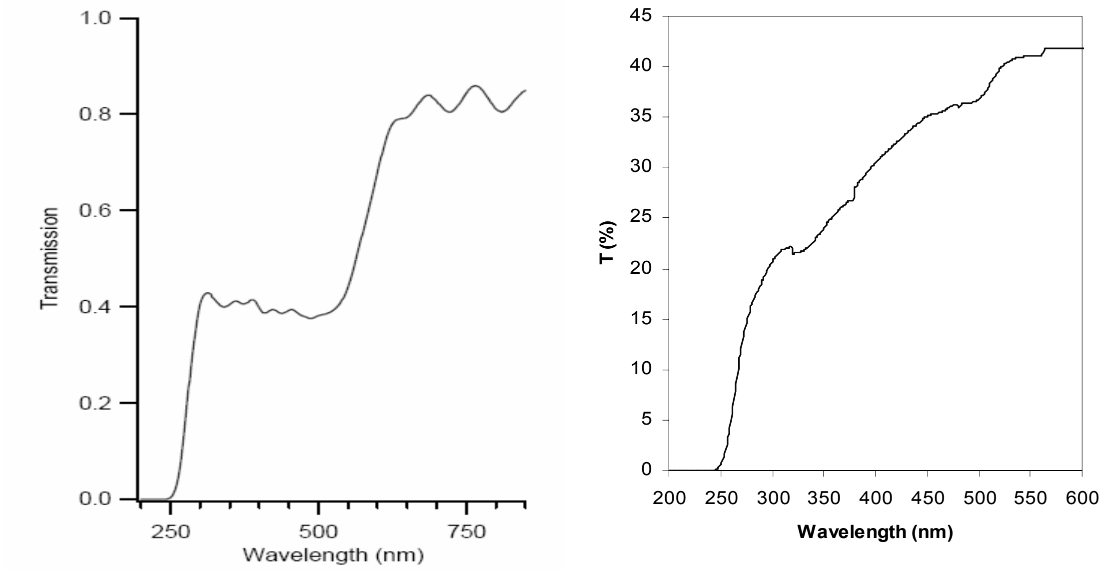

Figure 68: Transmission spectra of single crystal langasite (left:Tohuku, right:IKZ).

The optical bandgap of various single crystal langasite samples obtained from optical transmission measurements done by Dubovik et al [89] was about 4.1-4.9eV. Optical transmission experiment has also been performed on double-side polished thin disc of single crystal langasite (from two sources, Tohuku and IKZ) and the optical bandgaps of the two crystals appear to be 4.1eV (Figure 68). The close correlation of thermal and optical bandgap reinforces the credibility of the defect model used.

On electron and oxygen vacancy mobility

In the 5%Nb-doped material, it has been determined that the conductivity across the entire range of pO_2 is electronic (electrons) in nature. We have obtained expressions for *n* and K_r as function of temperature. This should allow us to determine oxygen vacancy concentrations using Eq. (40) (p.47) as function of temperature and pO_2. The concentrations of these two major defect species at 1000°C are plotted as a function of pO_2 in Figure 69. From it, it can be observed that at the pO_2-dependent regime (Defect Region I), the concentration of oxygen vacancy approaches that of electrons. Hence, in an electronic-dominant conductivity of 5%Nb-doped langasite, for this defect model to be valid, the oxygen vacancy mobility must be order of magnitude lower.

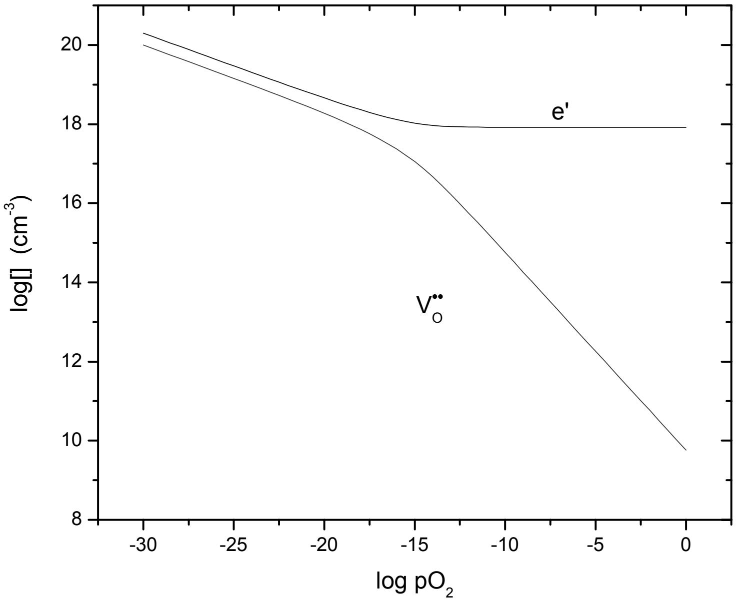

Figure 69: Concentration of major defect species of 5%Nb-doped langasite at 1000°C.

As shown in Figure 70, the electron mobility is several orders of magnitude higher that of oxygen vacancy. And thus at the pO_2-dependent regime (Defect Region I), even as the concentration of oxygen vacancy approaches that of electron, the conductivity remains predominantly electronic (as confirmed by concentration cell measurements, Figure 46, p.95).

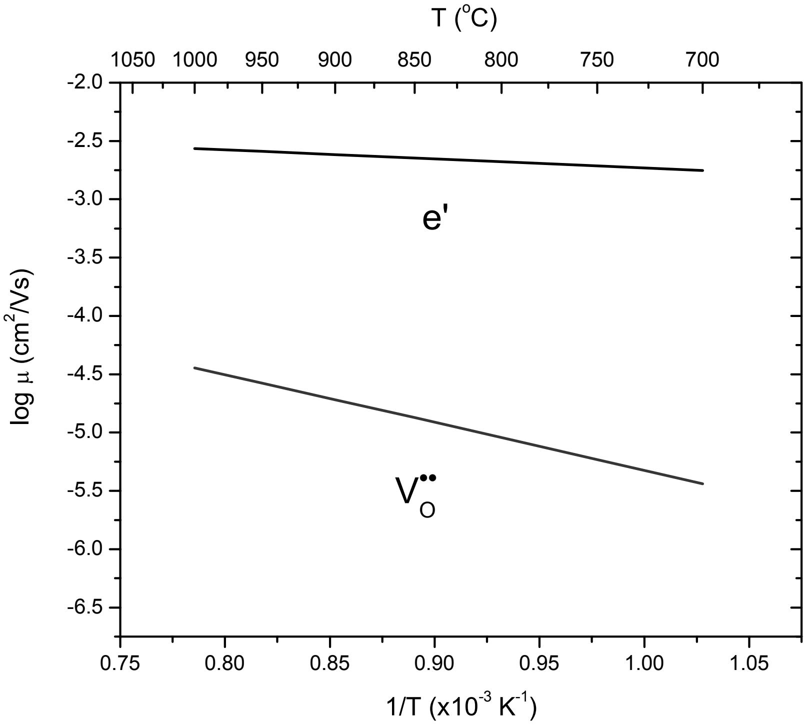

Figure 70: Comparison of V_o (Eq.(74), p.110) and e′ mobilities (Figure 40, p.89).

5.2.3 *Brouwer Diagrams*

With the defect models (Table 3 and Table 4), the conductivity data, and the previously derived expressions for mobility of different electrical species, the Brouwer diagrams for nominally undoped, 1%Sr-doped and 5%Nb-doped langasite can be calculated, which show the concentrations of defect species in those materials. The Brouwer diagrams for nominally undoped, 1%Sr-doped and 5%Nb-doped langasite at 1000°C were plotted in Figure 71, Figure 72 and Figure 73 respectively. Concentrations of oxygen interstitials was not calculated as we did not have the pre-exponential and the activation energy for K_F (Eq.(36), p.47).

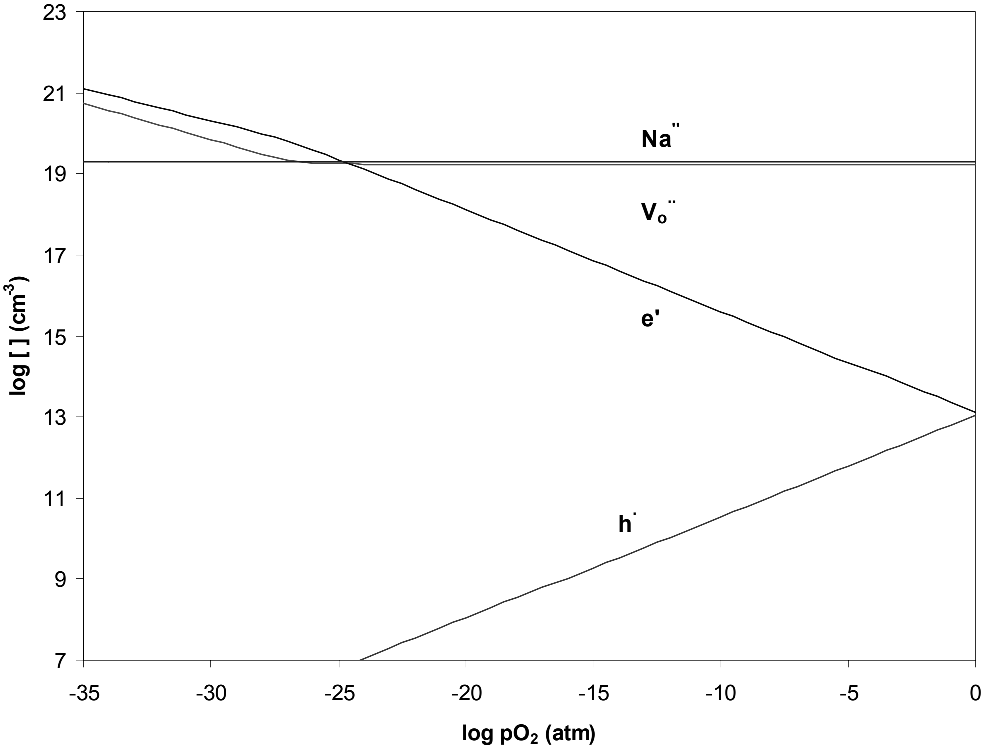

Figure 71: Brouwer diagram for nominally undoped langasite at 1000°C.

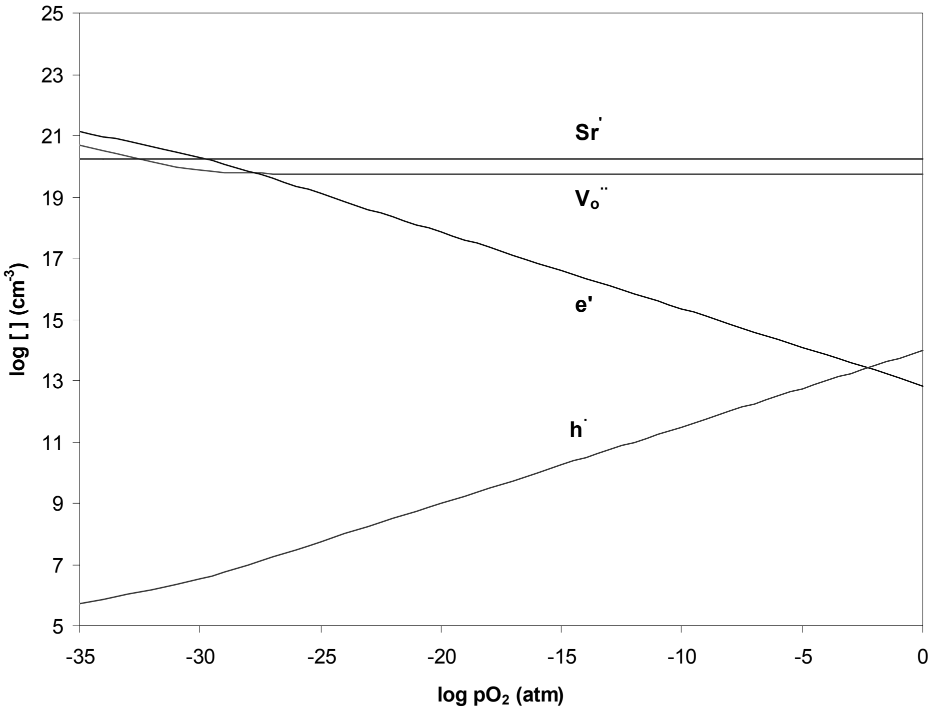

Figure 72: Brouwer diagram for 1%Sr-doped langasite at 1000°C.

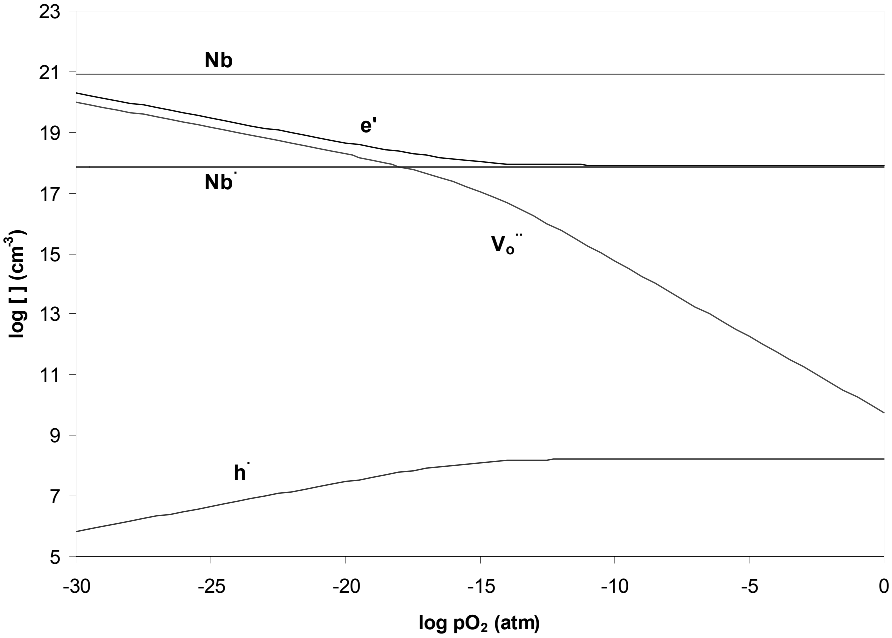

Figure 73: Brouwer diagram for 5%Nb-doped langasite at 1000°C.

5.2.4 Bulk Conductivity Prediction of Langasite

Summary of defect model of langasite

The defect model was successfully applied to acceptor and donor-doped langasite and allowed the extraction of valuable parameters which permit the prediction of the bulk conductivity properties of langasite. The summary of the defect model parameters is given in Table 6. The functions listed will be used in the modeling of bulk conductivity of langasite. Note that distinct K_r functions are utilized for acceptor and donor doped langasite respectively.

Table 6: Summary of langasite defect model parameters

	Acceptor-doped	**Donor-doped**
K_r ($cm^{-9}atm^{0.5}$)	$K_r = 10^{67} \exp\left(-\frac{5.7 \pm 0.06eV}{kT}\right)$	$K_r = 10^{71} \exp\left(-\frac{6.57 \pm 0.24eV}{kT}\right)$
K_o ($cm^{-3}atm^{-0.5}$)	$K_O = 4.6 \times 10^{18} \exp\left(-\frac{2.18 \pm 0.08eV}{kT}\right)$	N/A
K_e (cm^{-6})	$K_e = 6.8 \times 10^{42} \exp\left(-\frac{3.94 \pm 0.07eV}{kT}\right)$	N/A
Dopant Ionization	N/A	$\left[D^{\bullet}\right] = k_{Dn}^{1/2} \exp\left(-\frac{1.52 \pm 0.06eV}{2kT}\right)$
μ_e (cm^2/Vs)	N/A	$\mu_e = 0.011 \exp\left(-\frac{0.15 \pm 0.01eV}{kT}\right)$
μ_h (cm^2/Vs)	$\mu_h = (4.9 \pm 0.1)\, T^{-(0.096 \pm 0.002)}$	N/A
μ_{Vo} (cm^2/Vs)	$\mu_{Vo} = \frac{217}{T} \exp\left(-\frac{0.91 \pm 0.01eV}{kT}\right)$	N/A

Bulk conductivity prediction for acceptor doped langasite

As acceptor doped langasite is a mixed ionic-electronic conductor, its total bulk conductivity is the sum of electronic and ionic conductivity:

$$\sigma_{total} = \sigma_{ionic} + \sigma_{electronic} \tag{104}$$

$$\sigma_{total} = 2q\left[V_o^{\bullet\bullet}\right] \mu_{Vo} + nq\mu_e + pq\mu_h \tag{105}$$

And since the acceptor-doped langasite is in Region II and the Brouwer approximation $2\left[V_O^{\bullet\bullet}\right] \approx \left[A_c^{'}\right]$ can be applied, Eq.(105) can be written as:

$$\sigma_{total} = q\mu_{Vo}\left[A^{'}\right] + q\mu_e\sqrt{2}\left[A^{'}\right]^{-\frac{1}{2}} pO_2^{-\frac{1}{4}} K_r^{\frac{1}{2}} + q\mu_h\sqrt{\tfrac{1}{2}}\left[A^{'}\right]^{\frac{1}{2}} pO_2^{\frac{1}{4}} K_O^{\frac{1}{2}} \tag{106}$$

Using parameters in Table 6, σ_{total} can be predicted as function of temperature, pO_2, and acceptor concentration. In all predictions, we assume no defect association or ordering (dilute solution assumption). We also assume that the cation stoichiometry is perfect (i.e. no intrinsic defect compensation).

Bulk conductivity prediction for donor doped langasite

As for donor doped langasite which is dominantly electronic, the total conductivity is simply the electronic conductivity:

$$\sigma = qn\mu_e \tag{107}$$

The following showed the widely-known method for obtaining closed form solution for cubic equation. From Eq. (98) (p.124):

$$n = v - u + \tfrac{1}{3}\left[D^{\bullet}\right] \tag{108}$$

where:

$$u = \sqrt[3]{\frac{q}{2} + \sqrt{\frac{q^2}{4} + \frac{p^3}{27}}} \tag{109}$$

$$v = \frac{p}{3u} \tag{110}$$

The p and q in Eq. (109) and (110) are defined by:

$$p = -\tfrac{1}{3}\left[D^{\bullet}\right]^2 \tag{111}$$

$$q = -2pO_2^{-\frac{1}{2}}K_r + \tfrac{2}{27}\left[D^{\bullet}\right]^3 \tag{112}$$

The electron density, n, can then be solved in closed-form. Using parameters in Table 6 (p.132), σ for donor doped langasite can be predicted as function of temperature, pO_2, and donor concentration (assumed ionization process is involved).

Examples of bulk conductivity prediction for langasite

The predictive model was built in Microsoft Excel using the defect chemistry framework, and a few examples are illustrated here to demonstrate the usefulness of the model in looking at how the bulk conductivity can be minimized as functions of different variables (i.e. acceptor concentration, temperature, pO_2). Figure 74 shows the effect of acceptor concentration on acceptor doped langasite at 1000°C, showing the expected depressed n-type conductivity, and enhanced p-type and ionic conductivity with increased acceptor concentration.

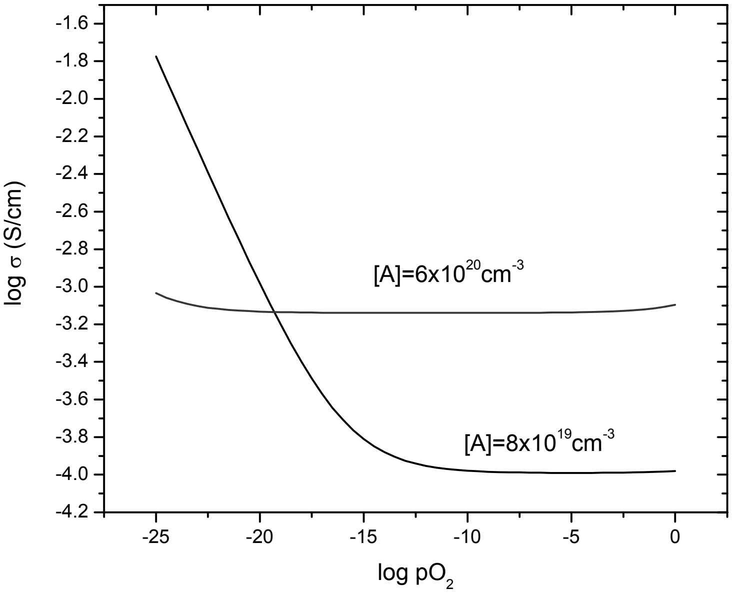

Figure 74: Conductivity of acceptor doped langasite with [A'] at 6×10^{20} and 8×10^{19} cm^{-3} at 1000°C.

Figure 75 shows that when T=1000°C and log pO_2 is set to 0, -10 and -20, the minimum conductivity (for minimizing electrical losses) depends on the operating pO_2. In this case, if a langasite resonator is fabricated for operation in air, the lower the acceptor concentration, the lower the conductivity. However, if the operation is in a reducing environment, for example when $\log pO_2 = -10$, the minimum conductivity will be at $\sim10^{18}$ cm^{-3} acceptor level. This will be valuable information when growing langasite crystals to achieve certain desired electrical properties.

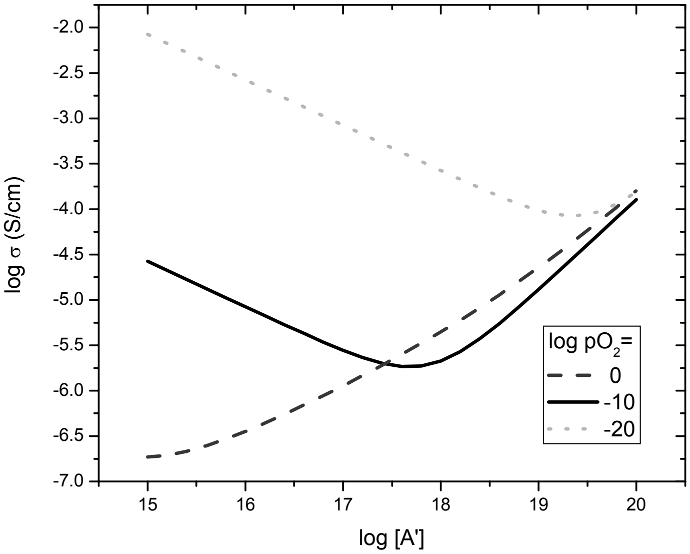

Figure 75: Conductivity of acceptor doped langasite as function of acceptor concentration at 1000°C.

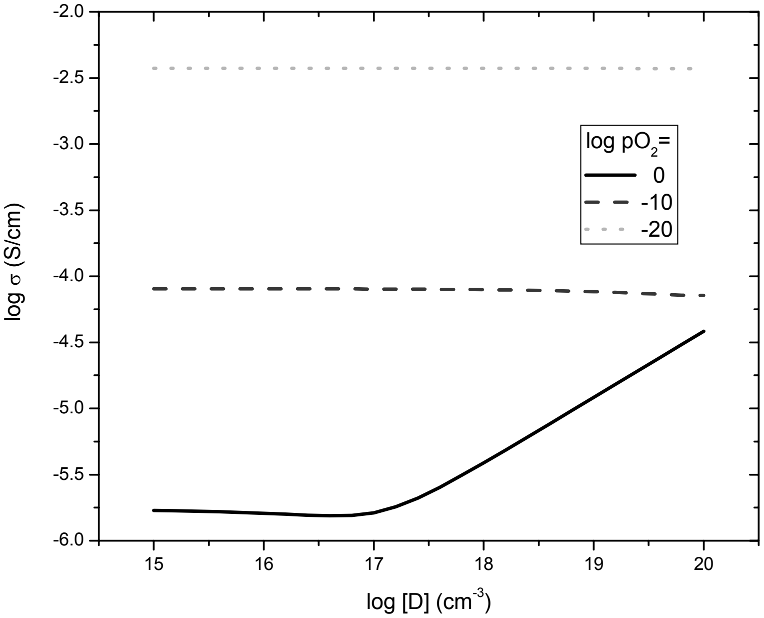

Figure 76: Conductivity of donor doped langasite as function of donor concentration at 1000°C.

In donor doped langasite, when T=1000^{o}C and log pO_2 were set to 0, -10 and -20, the conductivity of donor doped langasite with various donor levels can be calculated, as shown in Figure 76. In that plot, it can be observed, if langasite were to be used at pO_2=1atm, in order to achieve minimum conductivity (for minimizing electrical losses) donor concentration needs to be at 10^{17}cm^{-3} or lower, when the conductivity becomes reduction controlled; above 10^{17}cm^{-3}, the conductivity is controlled by donor concentration. Figure 76 also shows that for donor doped langasite, the donor concentration has little influence on the conductivity in more reducing environments, since they are reduction controlled at all pO_2's.

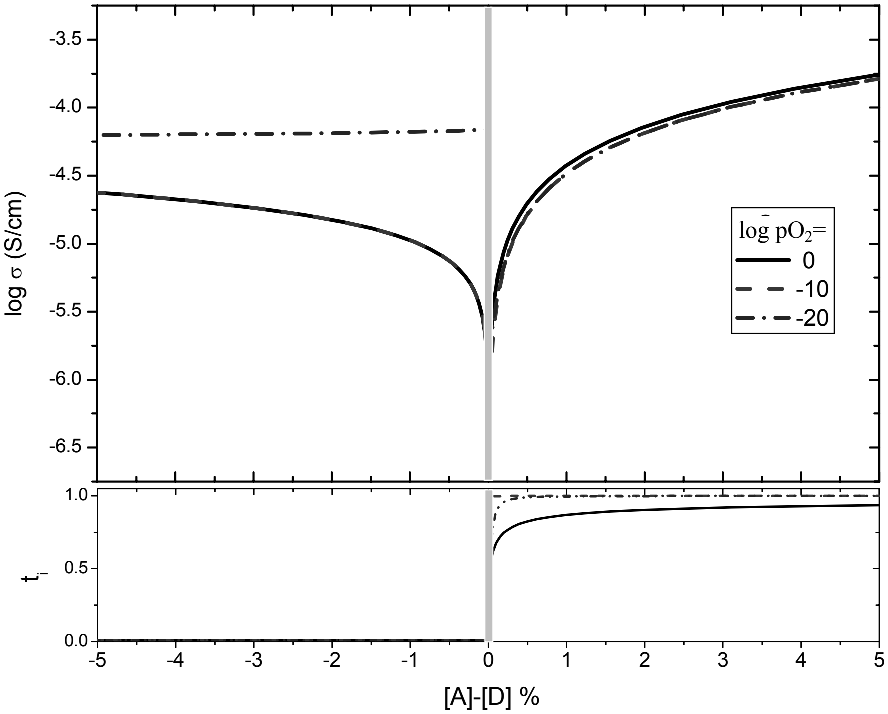

Figure 77: Conductivity and ionic transport number prediction for langasite at 3 different pO_2 and 800^{o}C as function of dopant level.

Figure 77 shows the prediction of langasite conductivity as function of dopant level, both acceptor and donor. It is possible to infer from the figure that the lowest conductivity can be obtained when langasite is intrinsic. However, to eliminate impurities totally from langasite, a large bandgap material, via dopant compensation will be difficult. Alternative doping strategies for langasite resonators operating at 800°C can be devised based on Figure 77. If langasite resonator is to be used in normal or slightly reducing environment (e.g. pO_2 from 1 to 10^{-10} atm), low concentration of donor doping will ensure a lower conductivity than using acceptor dopants. However, at extremely reducing environment ($pO_2=10^{-20}$ atm), low acceptor dopants ensure a lower conductivity than donor dopants.

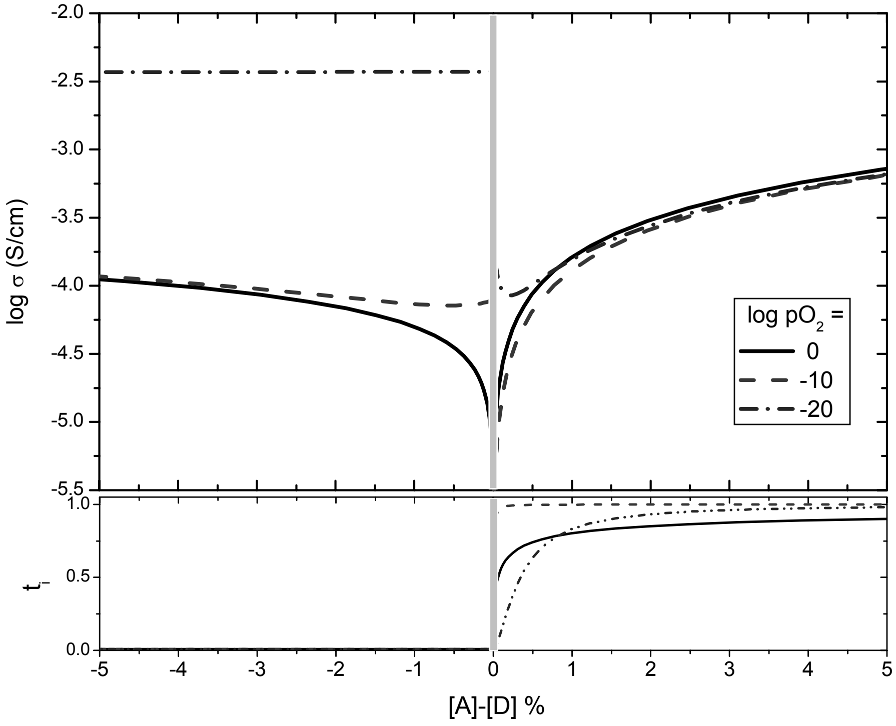

Figure 78: Conductivity and ionic transport number prediction for langasite at 3 different pO_2 and 1000°C as function of dopant level.

The situation changes when the temperature is increased to 1000°C (Figure 78). In air (pO_2 ~1atm), a low concentration of donor dopant will allow for low conductivity. At a reducing environment ($pO_2=10^{-10}$atm), a low acceptor dopant concentration will actually produce lower conductivity than donor doping. At extremely reducing environments ($pO_2=10^{-20}$atm), the minimum conductivity is produced with an acceptor doping level of about 0.2%. This ability to incorporate operating conditions (i.e. temperatures and pO_2) into processing considerations enables the design of langasite properties for improved operation performance (i.e. low electrical losses).

5.2.5 Mass Change Prediction for Langasite

The changing oxygen vacancy concentration with temperature or pO_2 will result in a corresponding mass change in a langasite resonator, and, if it is significant, can interfere with the frequency shifts induced in the active layer during sensor applications. Predicting the mass change will assist in delimiting the operating conditions of the resonator before excessive oxidation and reduction processes interfere with the sensing process.

In the defect model for acceptor doped langasite, Brouwer approximation was applied fixing the oxygen vacancy concentration to the acceptor level ($2\left[V_O^{\bullet\bullet}\right] \approx \left[A^{'}\right]$) in the ionic conduction regime. Nevertheless, it should be noted that reduction process still occurs at those pO_2's as apparent from the generation of electrons (see Region II of Figure 12, p.52). Brouwer approximations are reasonable for defect analysis since the generation of oxygen vacancies is negligible compared to the total oxygen vacancy concentration, but inadequate in the mass change prediction. In this case, the oxygen vacancy creation accompanying the generation of electron has to be taken into account.

In the ionic conduction regime of acceptor doped langasite, the neutrality condition is as follow:

$$n = 2\left[V_O^{\bullet\bullet}\right] - \left[A^{'}\right] \tag{113}$$

Substituting Eq.(113) into Eq.(40) (p.47) and rearranging gives:

$$\left[V_O^{\bullet\bullet}\right]^3 - \left[V_O^{\bullet\bullet}\right]^2 + \tfrac{1}{4}\left[A^{'}\right]^2\left[V_O^{\bullet\bullet}\right] - \tfrac{1}{4}\,pO_2^{-\frac{1}{2}}K_r = 0 \tag{114}$$

Using Eq.(114) and the K_r function listed in Table 6 (p.132), total oxygen vacancy concentration $\left[V_O^{\bullet\bullet}\right]$ can be calculated and n can then be determined as function of temperature, pO_2 and acceptor concentration using Eq. (40) (p.47). The change in oxygen vacancy concentration accompanying the generation of electrons is simply:

$$\Delta n = 2\Delta\left[V_O^{\bullet\bullet}\right] \tag{115}$$

The change in the vacancy concentration during operation (as temperature or pO_2 changes) can than be correlated to mass change.

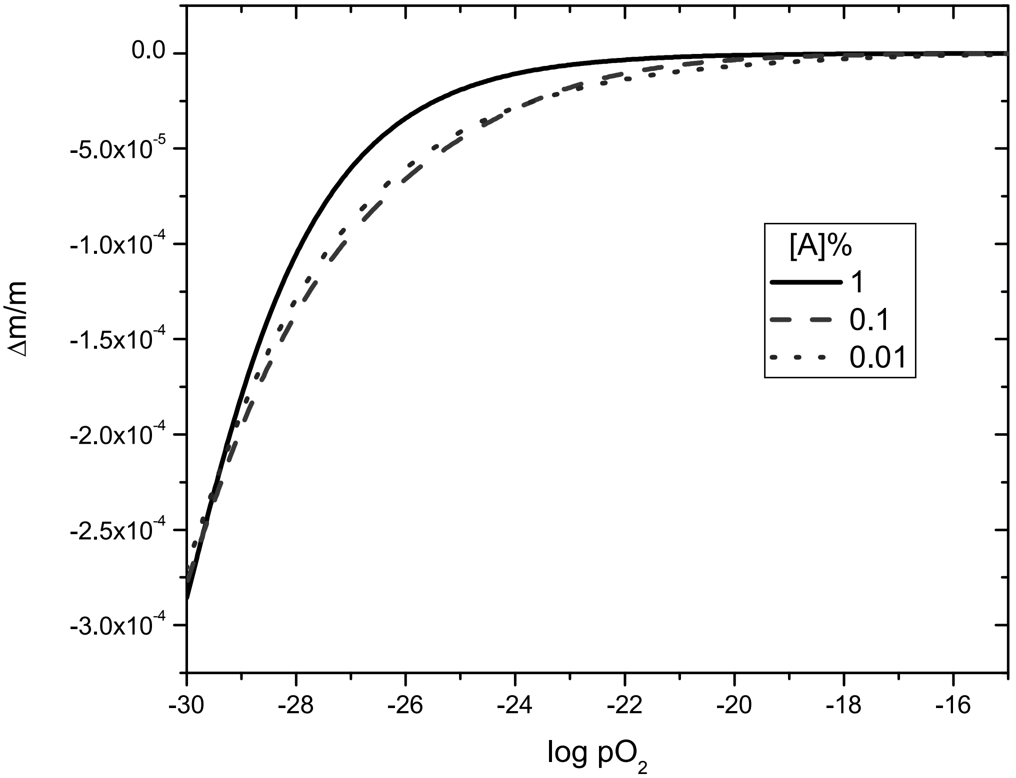

Figure 79: Fractional mass change (relatively to langasite in air) in langasite with 3 acceptor levels at 1000°C.

In Figure 79, the fractional mass change ($\Delta m/m$) in langasite (normalizing to pO_2=1atm) was predicted at 1000°C and at 3 different acceptor dopant levels. The fractional change with each order of magnitude of pO_2 was calculated in Figure 80. The fractional mass change can be related to fractional frequency change using Eq.(5)(p.27), which essentially states that $\Delta m/m = -\Delta f/f$. For a bulk acoustic wave resonator fabricated from a 0.1% acceptor doped langasite operating at a typical resonant frequency of 10 MHz, a Δf of 32Hz is expected if the oxygen partial pressure changes from pO_2=1atm to $pO_2=10^{-20}$atm due to generation of oxygen vacancies ($\Delta m/m=-\Delta f/f=-3.2\times10^{-6}$). This would theoretically limit the sensitivity limit and resolution of the resonator if it is to be used as a mass balance for investigating thin film oxygen stoichiometry which requires change in oxygen partial pressure of that magnitude, for example.

In Figure 79, it can also be observed that the level of acceptor have small effect on the magnitude of mass change occurs. Therefore, acceptor effects on both ionic and electronic conductivity, which are considerably higher, will having larger impacts on the resolution and mass sensitivity limit of the resonator (i.e. from electrical losses).

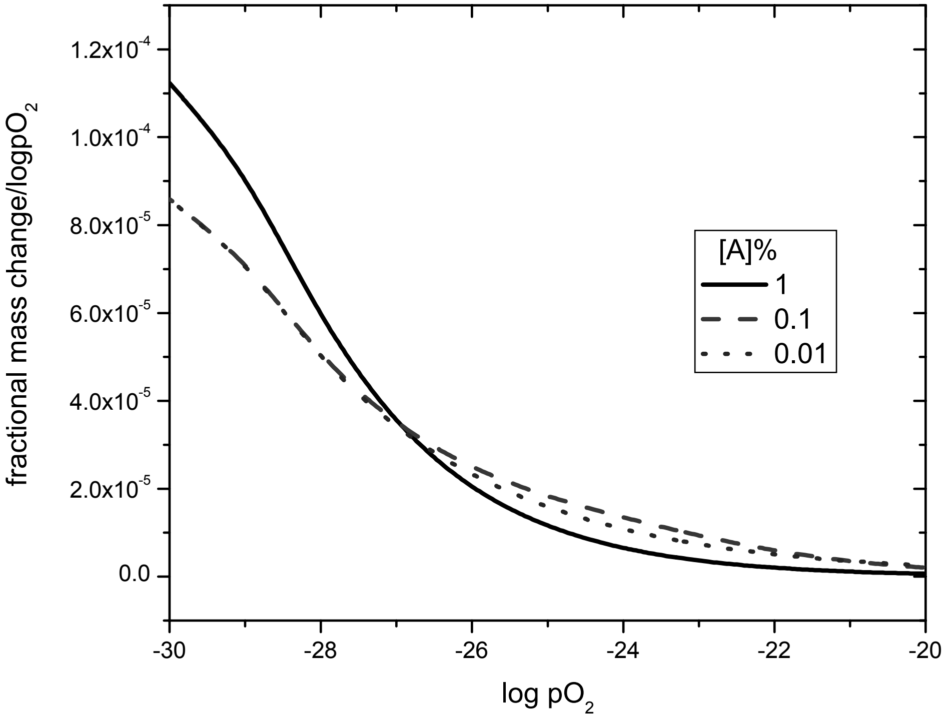

Figure 80: Fractional mass change/logpO$_2$ in langasite with 3 acceptor levels at 1000°C.

The donor doped langasite is electronically compensated and the oxygen vacancy concentration varies with pO_2, either with -1/4 or -1/6 power law depending on the defect region, Figure 69 (p.128). The mass change in donor doped langasite can be calculated using K_r (Table 6, p.132) and n (Eq.(108), p.133), which give oxygen vacancy concentration as function of temperature, donor level and pO_2. Figure 81 and Figure 82 show the fractional mass change of 3 different donor doped langasite at 1000°C as function of pO_2. The fractional change with each order of magnitude of pO_2 was also calculated and presented in Figure 83. When compared to the acceptor case, it can be observed that donor concentration has even lesser effect on the mass change (Figure 82). For a bulk acoustic wave resonator fabricated from donor doped langasite operating at 10MHz, Δf of 50Hz is expected if the oxygen partial pressure changes from pO_2=1atm to $pO_2=10^{-20}$atm due to generation of oxygen vacancies ($\Delta m/m=-\Delta f/f=-5\times10^{-6}$, irregardless of the dopant level). The frequency change in this case is comparable to the acceptor doped case.

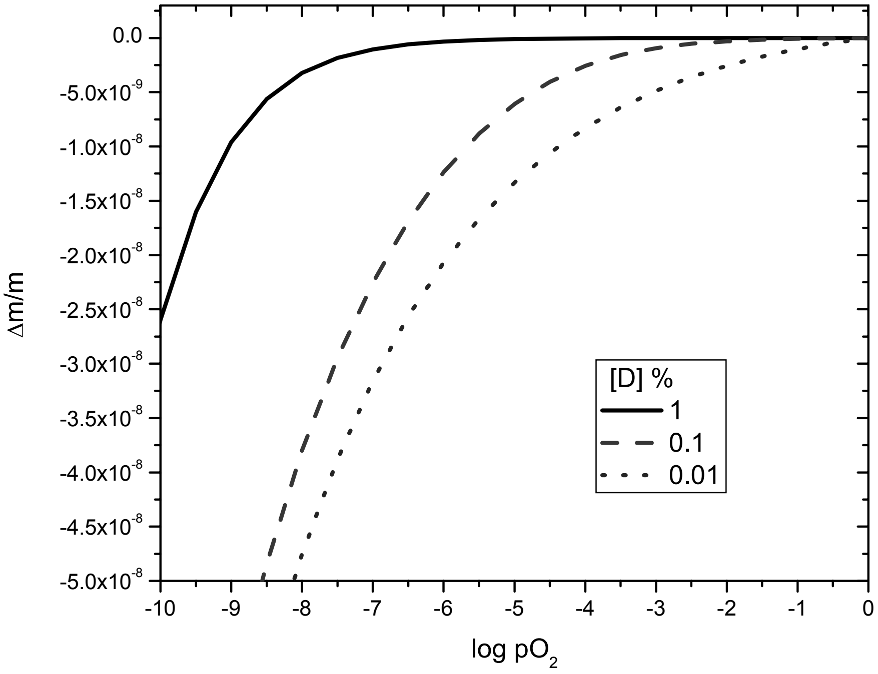

Figure 81: Fractional mass change (relatively to langasite in air) in langasite with 3 donor levels at 1000°C (high pO_2).

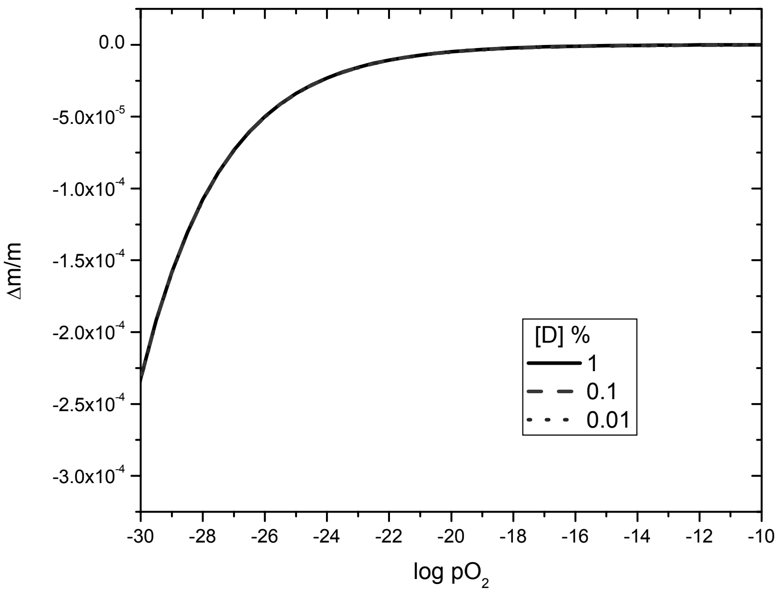

Figure 82: Fractional mass change (relatively to langasite in air) in langasite with 3 donor levels at 1000°C (low pO_2).

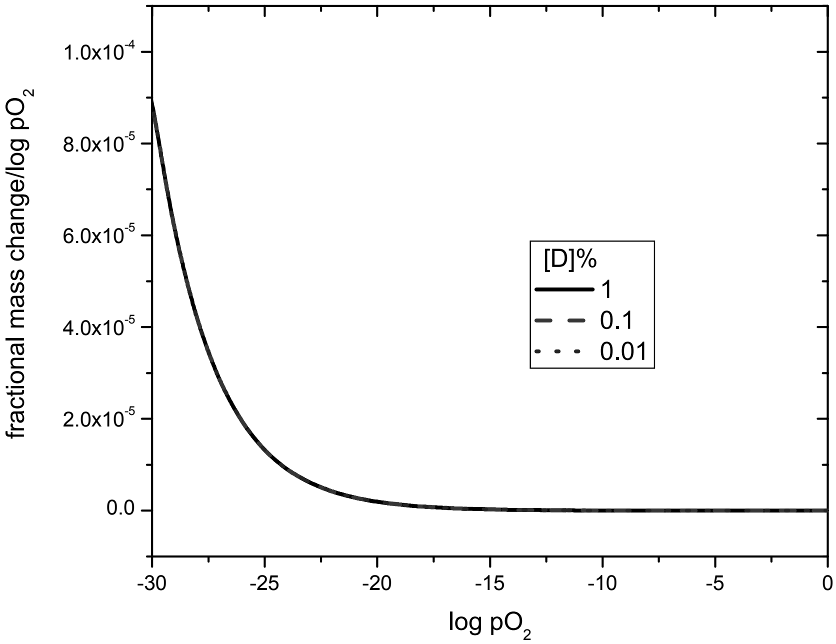

Figure 83: Fractional mass change/logpO_2 in langasite with 3 donor levels at 1000°C.

5.2.6 Impact of Transport Properties on Resonator

With the ability to predict bulk conductivity and intrinsic mass change in langasite as functions of temperature, dopant level and pO_2, it becomes possible to either define the acceptable operating range (temperature and pO_2) for a langasite resonator, or to intentionally dope langasite for operation within specific conditions.

One way to define the operating requirements is to state an acceptable Q value (Eq.(24), p.33) from which the required R_p and hence the required conductivity (depending on resonant frequency, Eq.(2), p.25) can be calculated. Using an isoconductivity plot, the possible conditions can be defined. For example, Figure 84 plots the isoconductivity lines of nominally undoped langasite (used in this work). If the required conductivity is 10^{-4} S/cm or lower and the required pO_2 is ~10^{-15}atm, the operating temperature must be 950°C or lower. In addition to electrical losses, significant mass change for nominally undoped langasite must be considered and could further restrict operating conditions.

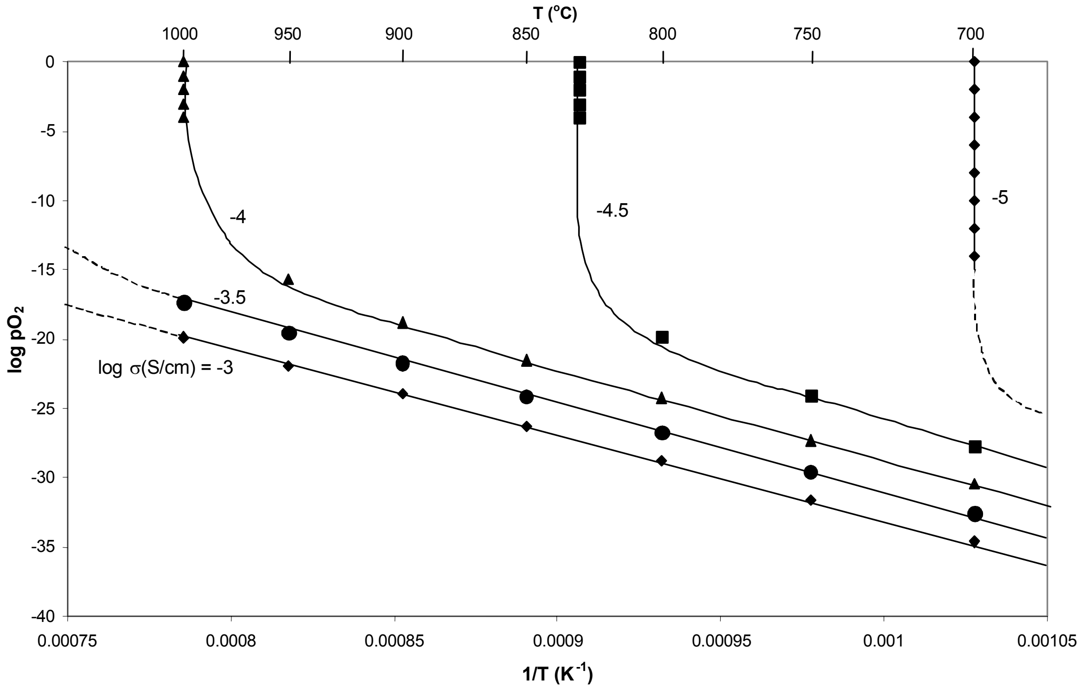

Figure 84: Isoconductivity plot for nominally undoped langasite.

The expression for *Q* (see Eq.(24), p.33) can also be used for examining the influence of decreasing resonator resistance on *Q*. As temperature increases, R_p decreases while R_s increases. At high temperature (at approximately 900°C or above for a 2MHz Y-cut langasite crystal resonator studied previously [48, 159]), the values of R_p and R_s converge. At those temperatures, R_p becomes smaller than R_s, making *Q* proportional to R_p. *Q* is also inversely proportional to the half-height-width (HHW) of the spectrum obtained by the network analyzer (Eq. (9), p.28), which can be equated to the uncertainty, δ, in resonant frequency of the resonator. Hence, R_p can be related and is inversely proportional to the uncertainty (δ). This relationship shows that increasing the conductivity by an order of magnitude (due to dopant or reduction/oxidation) can increase δ and thereby lower the sensitivity limit of the resonator by one order of magnitude at temperatures when electrical losses are high.

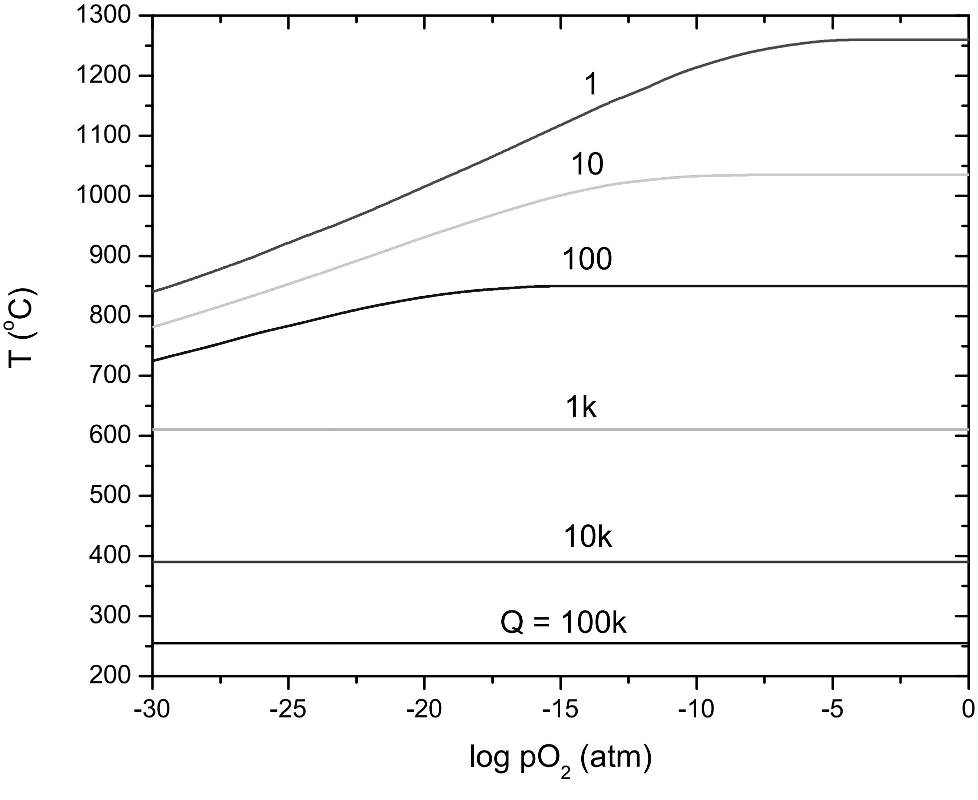

Figure 85: Iso-Q map of 2MHz langasite crystal (0.1% acceptor dopant) as function of temperature and pO_2.

In fact, for the abovementioned 2MHz Y-cut langasite crystal resonator (with electrode area of $2cm^2$ and assuming a 0.1% acceptor level), *Q* can be calculated as function of temperature and pO_2, and an iso-*Q* map can be derived (Figure 85). This map gives us the operating limits of the resonator for a certain *Q*. For example, if the *Q* is designed to be 1000, the resonator must operate below 611^oC, whereas if *Q* must be greater than 100, the temperature must be kept below 850^oC and 775^oC for $pO2=10^{-1}$ and 10^{-26} atm respectively.

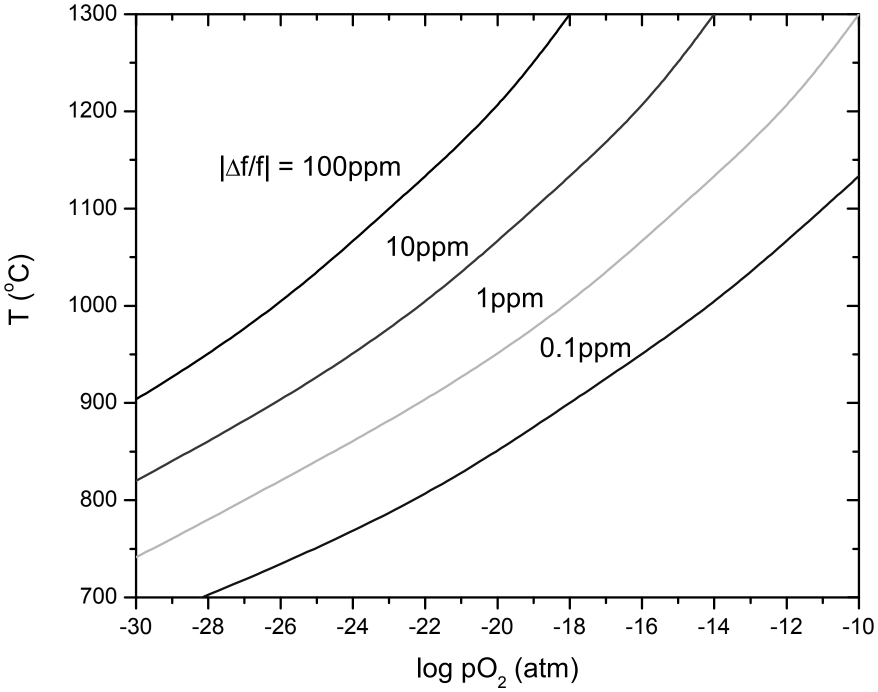

Figure 86: Resolution limits of langasite resonator as function of temperature and pO_2.

The fractional frequency change (*Δf/f*) due to change in oxygen vacancy concentration can also be related to the theoretical sensitivity limit for resonator. The fractional frequency change cause by decreasing pO_2 20 orders of magnitude from pure oxygen at 1000^oC is in the order of $\sim 10^{-6}$ (at 1000^oC for both acceptor and donor doped langasite), which translates to ~10Hz sensitivity limit in a 10MHz langasite resonator. It has been stated in previous section that, in theory, the frequency change would limit the resolution and sensitivity limit of the resonator. In practice, at high temperatures, the errors in resonant frequency measurements will be tens of hertz; the frequency change of a few tens of hertz due to intrinsic mass change in langasite will play insignificant role in limiting its resolution and sensitivity limit.

Figure 87 shows a map of resolution limit of langasite resonator. Since dopant levels play an insignificant role in the determination of $\Delta f/f$, this map can be used for all dopant level to estimate the operation limits (i.e. the temperature and pO_2) of the langasite resonator. For example, if the required $\Delta f/f$ is 1ppm (for around 10Hz change due to oxygen non-stoichiometry in a 10MHz crystal resonator), the operating condition must be below the 1ppm line in Figure 87.

5.3 Sensor Studies

5.3.1 Bulk Based Active Film

From Figure 50 (p.99), we observe that the response saturates below 1%O_2/Ar, with a frequency change of about -360Hz. In comparison to TiO_2 [48, 110], for which frequency change (~-500Hz) occurs at 6%H_2/Ar and no observable change at higher pO_2, the frequency shifts occur at much higher oxygen partial pressure for PCO on langasite. This confirms that the film controls the response to changes in oxygen partial pressure under oxidizing conditions.

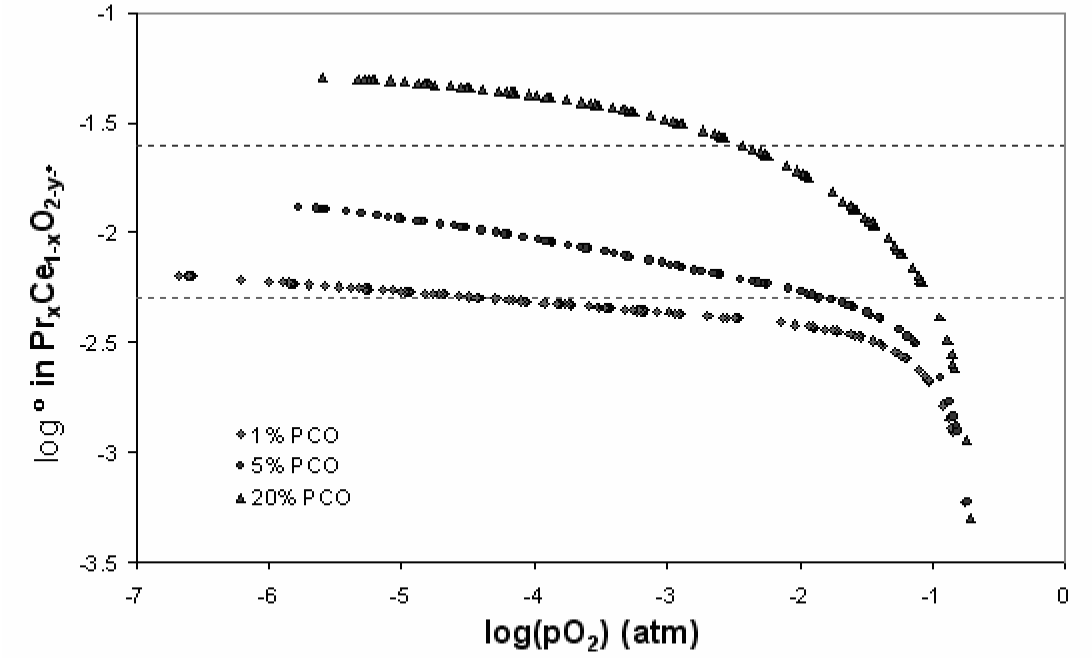

Figure 87: Oxygen nonstoichiometry of different PCO composition at 600°C [114].

Figure 87 shows a plot of the oxygen nonstoichiometry of PCO at 600°C; the measurements were performed by T.S. Stefanik [114] on bulk PCO samples. The PCO thin film on the langasite resonator was 15%PCO (i.e. $Pr_{0.15}Ce_{0.85}O_2$), expected to have similar oxygen nonstoichiometry behavior as the 20%PCO. As observed in Figure 87, the oxygen stoichiometry changes drastically from air to pO_2 of about 10^{-3}atm before reaching a plateau. The frequency change of the sensor was observed to plateau (Figure 50, p.99) at $pO_2=10^{-2}$atm, showing a close correlation to the oxygen nonstoichiometry of PCO.

Although there was good correlation in pO_2 at which frequency changes occurred, the sensitivity was found to be too high to be attributed to mass change alone. A similar resonator used in [50] had a mass sensitivity of approximately –21.9 cm^2 Hz μg^{-1} at 600°C. Based on that mass sensitivity, the areal mass density change for the sensor used in this study would be 16.4 $\mu g/cm^2$ at 1%O_2/Ar and lower oxygen partial pressure. The areal mass density of the PCO deposited, assuming a fully dense material (density at ~7.1 g/cm^3), would be ~320 $\mu g/cm^2$. This represents a 5% increase in mass of the PCO film. This could not be explained on the basis of mass change alone, since the magnitude is too large for oxygen non-stoichiometry, and the direction of frequency change indicates a mass increase (instead of a mass decrease during reduction of the PCO film).

Both the anomalous high frequency change and the direction of the shift suggest a cross effect not directly related to the mass change of the PCO film. Stress induced by the dilation of the PCO lattice upon reduction was suspected of being one of the likely sources of the sensor sensitivity. Another possible explanation for the anomalous high frequency change was put forward in Appendix C. It was suggested that the increase in conductivity of the thin film, which extended beyond the electrode onto the resonator, increases the effective electrode area, leading to a large decrease in apparent areal mass density of the active film and hence a large frequency change. However, this explanation cannot account for the direction of the frequency change in this case. Both explanations would be interesting to examine in future work; in Appendix C preliminary work examining the effect of electrode area on resonant frequency was described.

5.3.2 Reaction Based Active Film

<u>On quartz resonator</u>

Strong and reversible sensitivity to NO_2 is observed for temperatures of 300°C and above (Figure 55, p.103), with full recovery upon introduction of CO/CO_2. The large fluctuations around 15, 45 and 75 min in the response plots (Figure 51 to Figure 54) resulted from gas switching. Similar results were observed from sensor with $BaCO_3$ film prepared with 800nm PMMA templates. Two different PMMA templates were used with the expectation that they have different surface areas, and hence the amount of conversion to $Ba(NO_3)_2$ would be different. The similar responses between the two different microstructures were examined by investigating their surface areas.

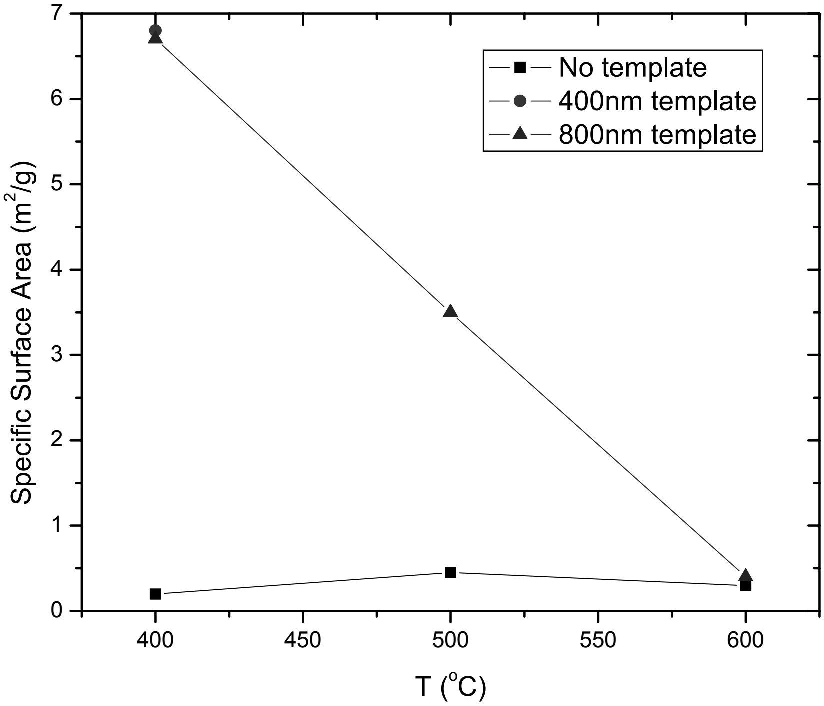

Figure 88: Specific surface area of $BaCO_3$ film prepared using different PMMA templates. The effects of annealing at higher temperature on the surface areas are shown; the high surface area of the templated preparation dropped to a value similar to that of an untemplated sample at 600°C.

Figure 88 shows that the surface areas of the two templated $BaCO_3$ films are nearly identical (surface areas were investigated for $BaCO_3$ films on Si/SiO_2 wafers, not quartz), and therefore the similar responses of two sensors is understandable. It also shows that the surface area of templated samples begin to decrease with increasing temperature; by 600°C, the surface area dropped an order of magnitude decrease to that of an untemplated sample. This instability of the templated $BaCO_3$ microstructure will be problematic if the sensor were to be utilized in diesel engines as the exhaust occasionally reaches such temperatures during rich burn conditions.

Since sensors based on quartz resonators were not heated beyond 400°C, the problem of instability was not apparent. Both quartz-based NO_2 sensors exhibit excellent sensitivity to NO_2, with sensitivity of ~10Hz/ppm NO_2 at 350°C (Figure 55, p.103). Hence we believe that the potential exists for low level detection of NO_2.

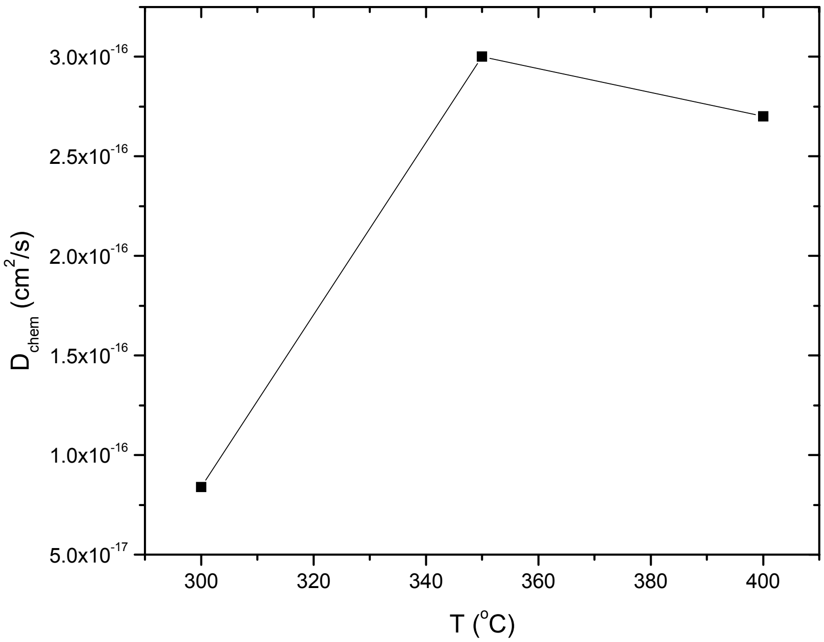

Figure 89: Chemical diffusivity extracted from Figure 52 (p.101).

We have also observed the kinetics of conversion to $Ba(NO_3)_2$ (Figure 51 to Figure 54) upon the introduction of NO_2 to be slow (several minutes to reach stabilization). Fitting the response curves of Figure 52 (p.101) and extracting the chemical diffusivity shows that the diffusivity has little thermal activation (Figure 89). The negligible thermal activation suggests that the experimental setup could be a limiting factor; the large sensor chamber means that gas exchange will take minutes and that will be observed as an apparent low chemical diffusion.

The kinetics of the recovery phase (during flow of 50/50 CO/CO_2 gas mixture), which represents the recovery of $BaCO_3$ from $Ba(NO_3)_2$, were found to be considerably slower than the kinetics characterizing the sensing phase, i.e., the kinetics relating to the conversion of $BaCO_3$ to $Ba(NO_3)_2$. If the kinetics of the sensing phase were limited by the apparatus, the recovery phase must be related to the slow conversion of $BaCO_3$ back to $Ba(NO_3)_2$. The recovery time, surprisingly, increased with increasing temperature (Figure 51 to Figure 54), most probably due to a need to convert a larger amount of reacted $Ba(NO_3)_2$ (formed at elevated temperatures due to more rapid kinetics as suggested by the larger Δf) back to $BaCO_3$.

On langasite resonator

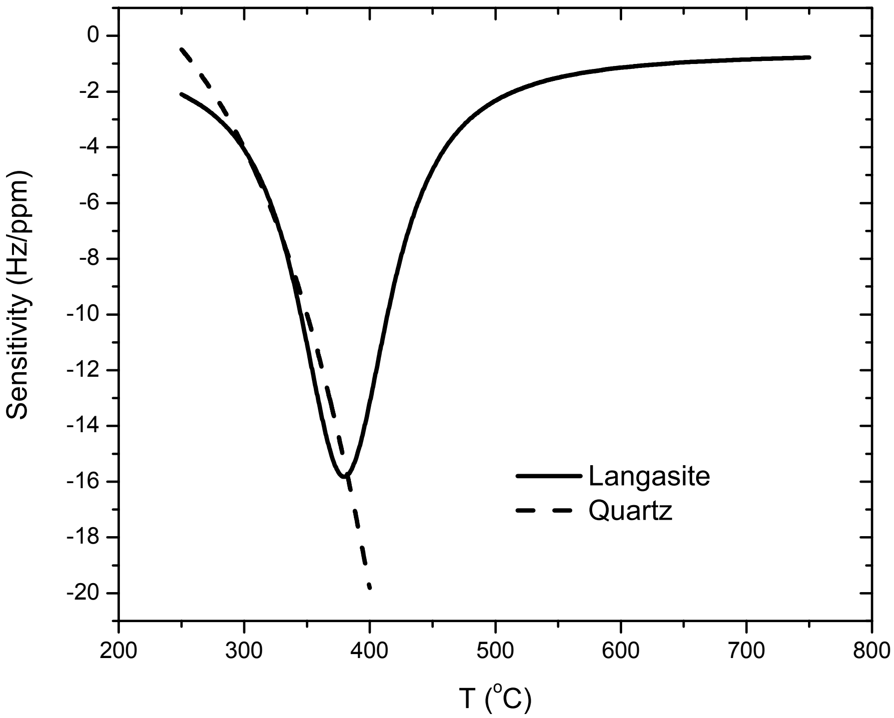

Figure 90: Comparison of sensitivity (calculated at 100ppm NO_2) of langasite and quartz-based NO_2 sensors.

The use of langasite resonator allowed us to investigate sensitivity of $BaCO_3$ towards NO_2 at higher temperature. The langasite-based sensor shows sensitivity to NO_2 at a lower temperature (~250°C) (Figure 57, p.105). Similar to the quartz-based sensor, the sensitivity increases as temperature increases, reaching a maximum at around 400°C. However, beyond that the sensitivity starts to drop reaching close to zero at around 650°C. If the sensitivity of the quartz and langasite-based sensors (both calculated at 100ppm NO_2) are compared (Figure 90), they appear similar and it seems that the Pt catalyst added to the $BaCO_3$ film in the langasite-based sensor had little effect. However, Eq.(25) (p.38) states that the mass sensitivity of a resonator is proportional to the square of the resonant frequency. As the quartz resonator was 5MHz and the langasite resonator was 3.6MHz, the sensitivity values have to be normalized; Figure 90 is replotted by recalculating the sensitivity of quartz as if it was 3.6MHz.

In Figure 91, it appears that the Pt increases the sensitivity, shifting the maximum sensitivity towards lower temperature (~350°C). Interestingly, [123] showed that maximum storage of a NO_x trap occurred at 350°C, with storage capacity dropping quickly down to zero at around 500°C. This is consistent with our observations of langasite-based NO_2 sensor.

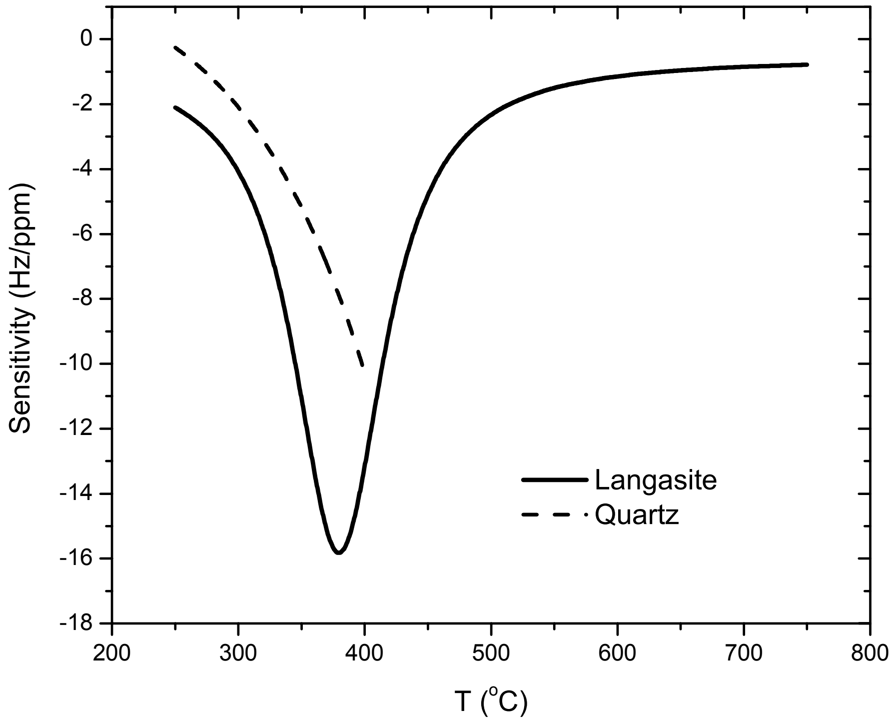

Figure 91: Normalized sensitivity (to resonant frequency of 3.6MHz) at 100ppm NO_2 of langasite and quartz-based NO_2 sensors

However, the Pt catalyst seems to have little effect on the kinetics during the sensing phase and recovery phase. The slow kinetics at the sensing phase has been hypothesized to be due to the limits imposed by the experimental setup. Efforts were made to improve the kinetics of the recovery phase by heating the sensor up to 700°C. However, it was not successful as the $BaCO_3$ films began to peel off after some time at that temperature.

Signal noise

Signal noise during the NO_2 sensor operation posed a major challenge especially at higher temperatures, where errors of ±100-200Hz were common. This was not compensated out completely using the reference resonator. One source of the noise was the small temperature fluctuations near the sensor, causing larger resonant frequency shifts as temperature increased due to the higher temperature-dependence of resonant frequency. Alternative methods to negate the temperature effect are needed for such sensors to be commercially utilized.

The quality and stability of the $BaCO_3$ film were other possible sources of signal noise. The acoustic phase shift due to the relatively thick film (~1μm) (Eq. (7), p.27) and structural instability (Figure 88, p.149) of the film could result in additional energy loss, resulting in a lower Q when compared to an uncoated resonator (Figure 92). As the uncertainty (δ) of resonant frequency measurement is inversely proportional to Q, a lower Q leads to a higher uncertainty and therefore a corresponding increase in signal fluctuations. A dense film deposited using thin film techniques (e.g. sputtering or pulsed laser deposition) should be considered in future work to reduce damping from the film.

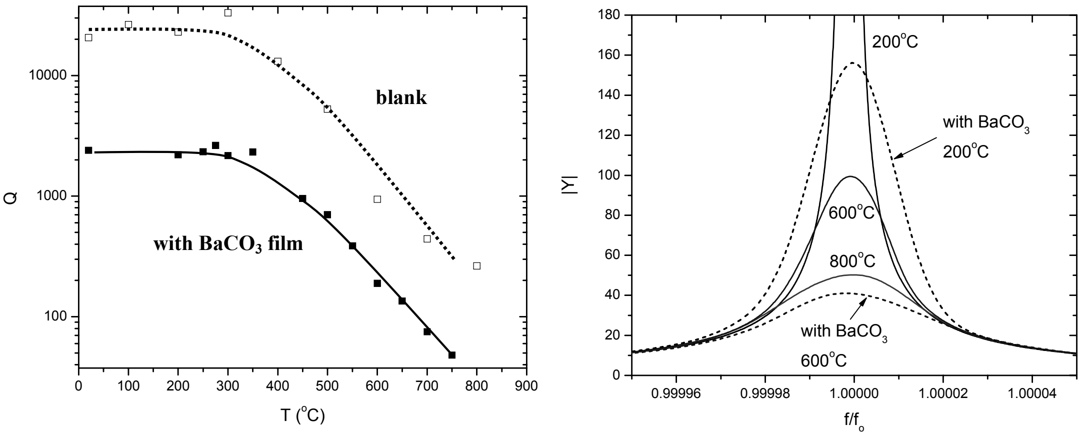

Figure 92: *Q* of langasite resonator, both blank and with $BaCO_3$ film, as function of temperature (right). The corresponding |*Y*| vs *f*/*f*$_o$ (*f*$_o$: peak frequency) of selected temperatures are also shown (left). The lower *Q*'s of $BaCO_3$ coated langasite resonator resulted in greater uncertainty in measurements.

Chapter 6: Conclusion

6.1 Summary

The transport properties of langasite were investigated at temperatures ranging from 700 to 1000^oC, and at pO_2's of 1 to 10^{-25}atm. Acceptor and donor doped langasite samples were examined using 2-point impedance, concentration cell and thermoelectric power measurements. The high temperature annealing of langasite shows the material to be chemically stable at high temperatures, under reducing as well as oxidizing conditions. A defect model was developed and used to describe the electrical properties as functions of temperature, dopant levels and pO_2, and provides a framework for explaining the observed transport properties and the underlying physical processes.

Acceptor doped langasite exhibits mixed ionic-electronic conductivity behavior. At high pO_2, nominally undoped (with background acceptors) langasite was predominantly an ionic conductor due to mobile oxygen vacancies. The ionic conductivity was pO_2-independent and was essentially fixed by background acceptors. At low pO_2, the conductivity becomes increasingly n-type electronic dominated by electrons generated by the reduction process. Increasing acceptor levels increase the ionic and p-type electronic conductivity, while depressing the n-type electronic conductivity – observations consistent with predictions of the defect model. In the Sr-doped langasite, defect ordering leads to in deeper potential wells for the oxygen vacancies resulting in the higher oxygen vacancy migration energy (0.91±0.01 versus 1.27±0.02eV for nominally undoped and 1%Sr-doped langasite respectively).

In donor doped langasite, the conductivity was electronic at all examined temperatures and pO_2's, as confirmed by concentration cell measurements that showed negligible ionic transference numbers. The electrons dominated the conductivity, leading to a donor compensated regime at high pO_2 and a reduction dominated regime at low pO_2. Nb was found to be a deep donor with ionization energy of 1.52(±0.06)eV, as confirmed by thermoelectric power measurements.

The electronic mobilities of langasite for both electrons and holes were also determined. The electron mobility of langasite was found to be activated (polaron hopping) with an activation energy of 0.15(±0.01)eV, whereas the holes were assumed to be quasi free carriers.

Using the defect model, a number of important constants were derived. The oxidation enthalpy was determined to be 2.18(±0.08eV) for acceptor doped langasite. The reduction enthalpy was determined to be 5.70(±0.06)eV and 6.57(±0.24)eV for acceptor and donor doped langasite respectively. The reliability of the reduction and oxidation enthalpies was reinforced given the consistency with values of the optical bandgap obtained independently through optical transmission experiments.

The derived defect model was utilized in building a predictive model for langasite. This model was used to calculate the bulk electrical conductivity and intrinsic mass change of langasite due to oxygen vacancy generation as functions of temperature, dopant level and pO_2. The establishment of defect specie concentrations and their mobilities as function of pO_2 and temperature allowed us to define the acceptable operating range and/or design the properties of langasite for minimum resistive loss and intrinsic mass change, which affect the resolution and sensitivity limit of the resonator. At high temperature (900°C or higher for 2MHz langasite resonator), the electrical loss of langasite became significant. With the bulk resistance proportional to Q, this leads to increased uncertainty in the measurements, δ, of the resonator (i.e. lower resolution). On the other hand, it was also demonstrated that langasite exhibits only very small mass change due to oxygen stoichiometric change, and, even at 1000°C, $\Delta f/f$ is 5ppm or less for a pO_2 change of as much as 20 decades.

Two high temperature resonant-based sensors were studied. Oxygen partial pressure detection was performed using a bulk-based film (praseodymium-cerium oxide), and NO_2 detection was performed using a reaction-based film (barium carbonate). The processes controlling sensitivity in each instant were discussed. For the sensor using the bulk-based film, in order for it to be useful for measuring stoichiometric changes in thin films, the anomalous frequency shift has to be understood. Even though frequency changes were shown to be related to stoichiometric changes, mass change alone could not explain the large observed frequency shifts. For the reaction-based NO_2 sensor, high temperature operation posed major challenges, i.e. instability of microstructure and high signal noise. It is crucial to overcome these limitations since NO_2 sensors will have to survive the extreme conditions of engine exhausts while performing precise measurements down to parts-per-million level of NO_2. Future work to address the above sensor performance issues and additional work on sensor packaging will be required.

6.2 Recommendations for Future Work

Listed below are some recommendations for future work, both as extensions of the work presented here and as general recommendations for a better understanding of transport properties of langasite-type materials:

- Examine langasite with more dopant levels (both acceptor and donor) allowing for better understanding of defect association/ordering effects, if any. Varying dopant types will allow the examination of dopant size on transport properties. This series of studies will provide refinement on the predictive model, giving a better estimation on the effects of dopants on transport properties.

- Growth of doped single crystal langasite allows the examination of effect of doping on the piezoelectric properties of langasite. Complete substitution of a cation will also provide interesting transport and piezoelectric properties to be studied. Other members of langasite family can also be examined in the same fashion.

- Each sensor application has potentials for further studies. The frequency change in bulk-based type film was not entirely understood– stress effect studies should be undertaken. The reaction-based film can be studied for cross-sensitivity to other interfering species or effects. More systematic studies on the effects of microstructures, catalysts, and temperature cycling on sensitivity and kinetics can be carried out. A better temperature compensation scheme using harmonics can be implemented, especially at higher temperature, to reduce noise. Miniaturization of the resonator for use in a sensing array can be examined for better selectivity and lower power requirements.

- Barium carbonate film (for NO_2 sensing) should be deposited onto langasite resonator with thin film technique so as to obtain a better control over film adhesion and thickness uniformity. This might lead to a lowering of noise, which will be essential if it is to be used for NO_2 monitoring.

- The possibility of growing epitaxial langasite thin films can be examined. Such thin films can form a basis for surface acoustic wave devices with higher resonant frequencies (higher sensitivity) and remote control capability. Sensor array miniaturization and fabrication using thin film piezoelectric materials will potentially be simpler than using single crystals.

Appendix A

DMMP sensing with SiO_2 active film

Experimental

SiO_2 was used as the active film on a 10MHz AT-cut QCM (Elchema). SiO_2 films were deposited using the PMMA templating technique [148] onto 10MHz (Elchema) AT-cut quartz resonators. The first step of this technique is to create a 3-D array of PMMA microspheres. About 0.20g (800nm in diameter) of PMMA microspheres (Soken Chem. & Eng. Co., Ltd.) was dispersed in 10 ml deionized water using ultrasonicator for 10min. The suspension was then dripped by pipette onto one electrode face of quartz resonators and allowed to dry at room temperature over night.

Tetraethoxysilane (TEOS) was then permeated (using a pipette) into the interstices of the 3-D array of PMMA microspheres, in vacuo, at room temperature. Thereafter, the film was treated consecutively for 2 days at room temperature and 1 day at 50°C (controlled using hotplate) in HCl atmosphere. HCl atmosphere was created by enclosing the film in a beaker together with concentrated HCl, without the film or the resonator coming in contact with the acid. After the HCl treatment, the film was thermally treated at 80°C for 12hr for the formation of SiO_2 film. Further heat treatment at 400°C for 2hr remove the PMMA microspheres, creating a porous SiO_2 film. The resultant SiO_2 microstructure is shown in Figure 93, in which the highly porous nature of the structure can be observed.

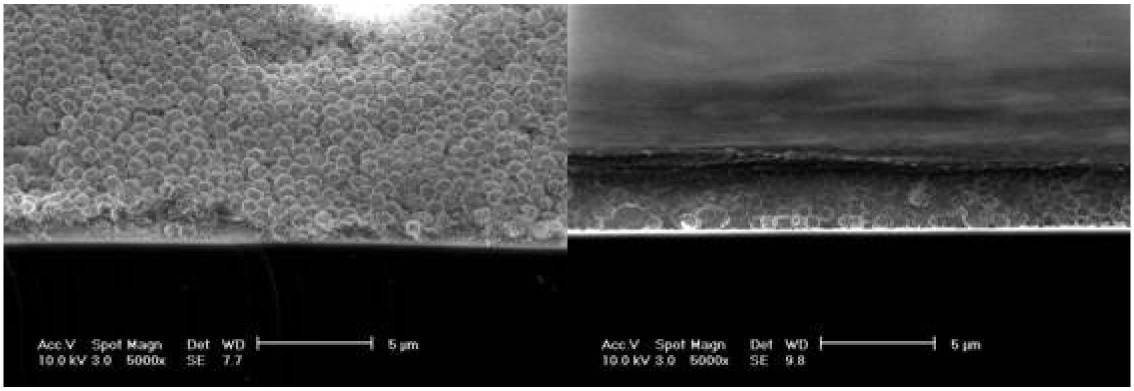

Figure 93: Microstructure of SiO_2 film prepared from 800nm PMMA microspheres.

The sensor was tested at temperatures ranging from room temperature (~20°C) to 100°C. After equilibrating at the test temperature in dry air, different concentrations of DMMP were introduced. The DMMP concentration was varied by flowing dry air over DMMP under controlled temperature (controlling its vapor pressure) and then mixing that with pure dry air. The total flow rate was controlled at 100sccm. The test setup used was identical to that used for the thesis work (see Experimental for further details).

Results

Quartz resonators coated with SiO_2 active films were exposed to a fixed concentration of DMMP vapor at various temperatures. The sensor was equilibrated in dry air for 1hr before being exposed to DMMP for 1hr. The concentration of DMMP was controlled by fixing the temperature of a DMMP bath at 20°C with dry air being flowed over it. The calculated concentration of DMMP in this case is about 920ppm. The sensor temperature was varied to observe the effect on response. The frequency response to DMMP is shown in Figure 94.

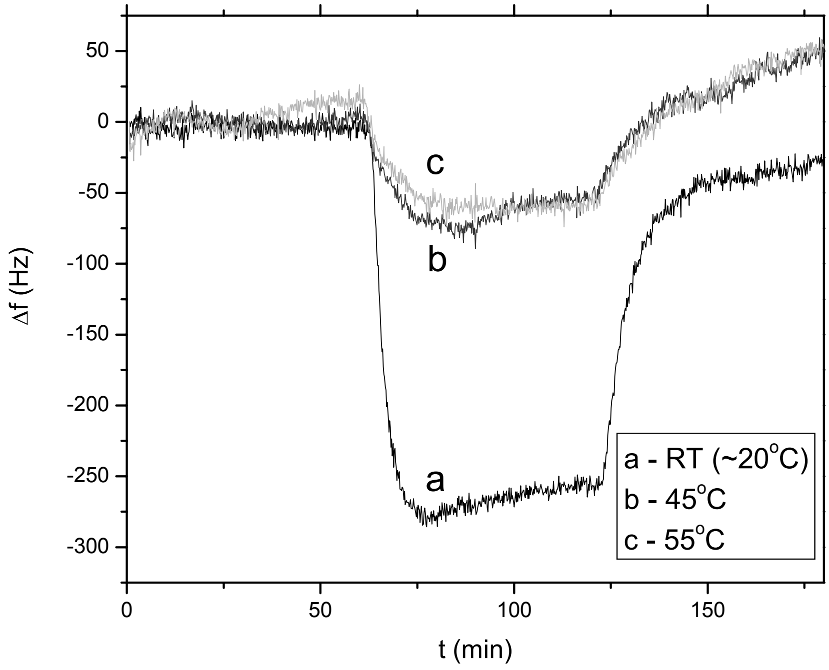

Figure 94: Response of SiO_2 coated QCM sensor to 920ppm DMMP at various sensor temperatures.

The SiO_2 coated QCM sensor was then exposed to a lower concentration of DMMP, at around 170ppm. This concentration was obtained by fixing the DMMP temperature at 0°C while dry air was flowed over the DMMP fluid bath. The sensor was evaluated at two sensor temperatures (RT and 55°C) and the frequency response to 170ppm DMMP is shown in Figure 95. The two data sets allow us to see that DMMP sensitivity varied drastically between 20 and 45°C.

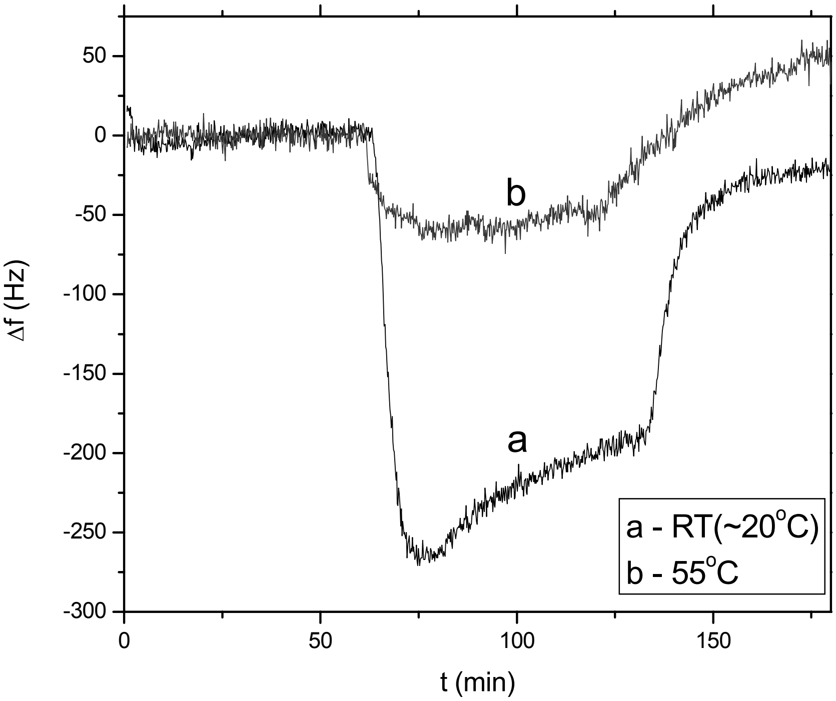

Figure 95: Response of QCM/SiO_2 sensor to 170ppm DMMP at various sensor temperatures.

The temperature of the sensor was then fixed at room temperature (where sensor sensitivity is high as suggested by Figure 94 and Figure 95) and its response to varying concentration of DMMP was examined. The frequency changes measured as a function of DMMP concentration are plotted in Figure 96.

The first derivative of the response curve, which gives the sensitivity of the sensor, is also plotted in Figure 96 and illustrates that the sensor begins to saturate at about 500-600ppm of DMMP.

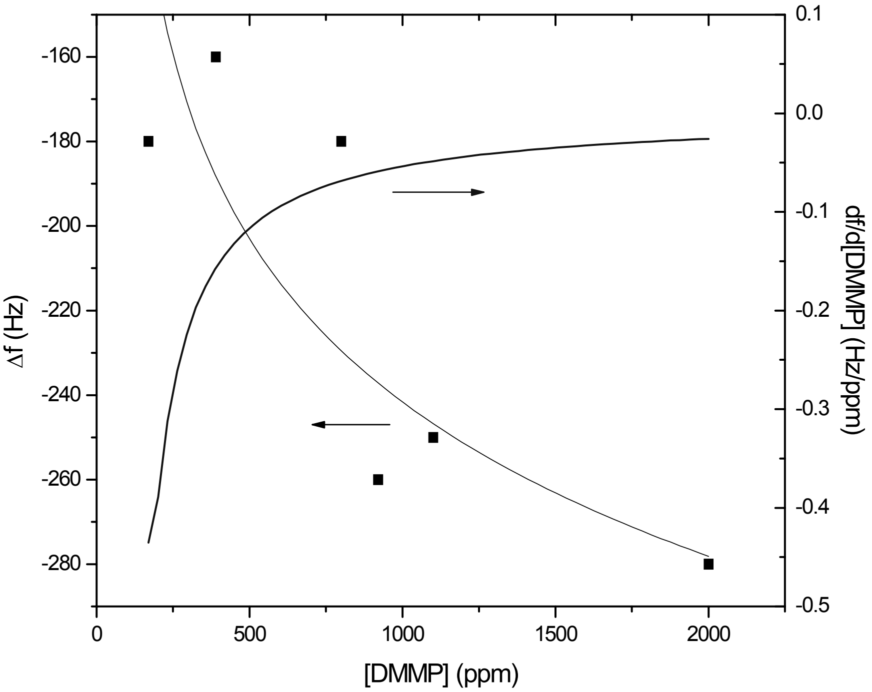

Figure 96: Response of QCM/SiO$_2$ sensor at RT to different concentrations of DMMP.

The temperature sensitivity of the sensor was examined in greater detail by examining its response to 920ppm DMMP for temperatures between 20 and 100°C. The results, shown in Figure 97, confirm that there is a decrease in response as the temperature of the sensor increases; at 100°C, the response goes practically to zero. The right axis shows the sensitivity normalized to sensitivity at 20°C. At around 30°C, the sensitivity of the sensor is already halved from 20°C demonstrating the highly temperature dependent nature of the sensitivity towards DMMP.

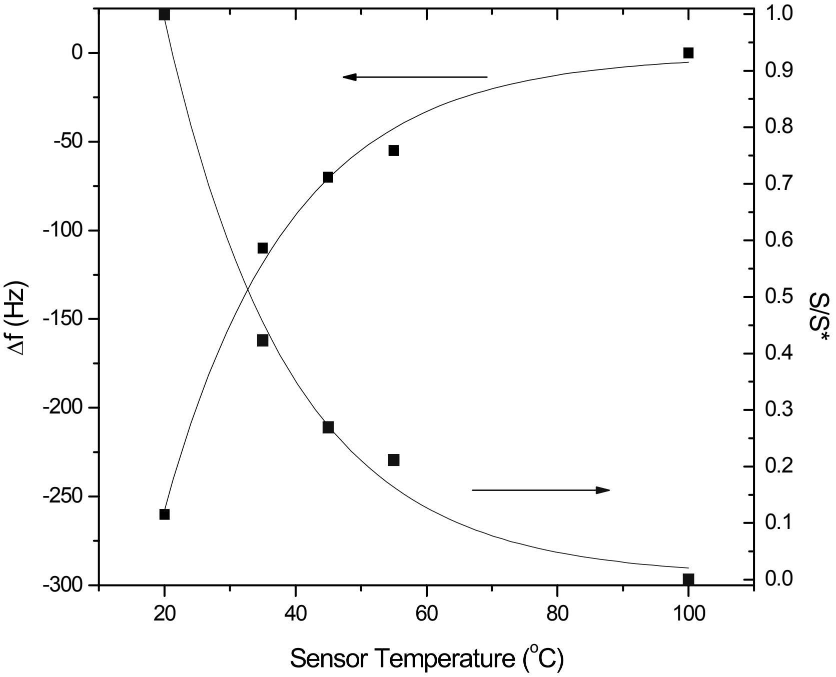

Figure 97: Influence of sensor temperature on the frequency response to 920ppm DMMP (left axis) and on sensitivity (normalized to sensitivity at 20°C, right axis)

Discussion

The decrease in resonant frequency is indicative of a mass increase caused by adsorption of DMMP on the surface of the silicon dioxide film. The sensor responds very quickly after exposure, although, at 500-600ppm DMMP and above, the sensor response seems to have saturated (Figure 96). In addition, recovery at room temperature, in air, seems incomplete.

The sensor tests at room temperature also show that as temperature increases, the sensor sensitivity to DMMP drops (Figure 97). This could be explained by the adsorption-desorption process which is highly sensitive to temperature. At low temperatures, adsorption is favored and more DMMP molecules stay on the surface of the SiO_2 film; which is also the reason why recovery process was incomplete. At higher temperature, the desorption is favored and less DMMP can be adsorbed on the surface of SiO_2, resulting in weaker frequency shift. Figure 97 also provides an estimation for the operation temperature of DMMP resonant sensors. From the plot, the sensor should be operating at room temperature or even lower for maximum sensitivity. However, for recovery, the sensor should be heated to around 100^{o}C for almost complete desorption (i.e. zero sensitivity to DMMP).

The logical next question will then be what advantage would a high temperature piezoelectric like langasite have over a cheaper alternative like quartz. One reason is that if the adsorbate is not as volatile as DMMP, a higher temperature might be needed for complete regeneration. Complete regeneration is necessary for ensuring that the maximum number of adsorption sites is available for the next sensing cycle. Furthermore, having a high temperature piezoelectric might be necessary for adsorption process measurements done at high temperature. Another reason is that utilization of a high temperature piezoelectric without destructive phase transformation removes restrictions on process conditions used to deposit and anneal the active films (e.g. allowing higher temperature treatments).

Appendix B

Glow Discharge Mass Spectroscopy

Results and Discussion

The nominally undoped and 1%Sr-doped langasite samples were analyzed for trace elements using glow discharge mass spectroscopy. The analyses were performed by Northern Analytical Laboratory, Inc (23 Depot St, Merrimack, NH 03054) with proprietary procedures and software. The results for the two samples are tabulated below.

Table 7: Trace elements in nominally undoped langasite.

ANALYSIS	ppmw	ANALYSIS	ppmw	ANALYSIS	ppmw
~~H~~		Zn	1.2	Pr	1.2
Li	0.30	Ga	Major	Nd	0.05
Be	<0.1	Ge		Sm	0.20
B	9.2	As	≤0.1	Eu	<0.05
~~C~~		Se		Gd	<0.5
~~N~~		Br		Tb	<0.05
O	Major	Rb		Dy	0.25
F	<1	Sr	0.20	Ho	<0.05
Na	100	Y	1.4	Er	<0.05
Mg	1.3	Zr	40	Tm	<0.05
Al	12	Nb	1.1	Yb	<0.05
Si	Major	Mo	0.10	Lu	<0.05
P	1.1	Ru		Hf	<0.05
S	2.0	Rh		~~Ta~~	
Cl	0.59	Pd		W	<0.1
K	1.2	Ag	<1	Re	
Ca	16	Cd		Os	
Sc	0.02	In		Ir	
Ti	0.25	Sn		Pt	0.65
V	0.037	Sb		Au	
Cr	≤0.5	Te		Hg	
Mn	0.070	I		Tl	
Fe	6.0	Cs		Pb	1.0
Co	<0.01	Ba	0.45	Bi	<0.05
Ni	0.15	La	Major	Th	<0.01
Cu	1.5	Ce	1.7	U	<0.01
All other elements <0.1ppmw * Major >1wt%					

Table 8: Trace elements in 1%Sr-doped langasite.

ANALYSIS	ppmw	ANALYSIS	ppmw	ANALYSIS	ppmw
~~H~~		Zn	0.45	Pr	1.6
Li	0.45	Ga	Major	Nd	0.05
Be	<0.1	Ge		Sm	0.25
B	1.3	As	≤0.1	Eu	<0.05
~~C~~		Se		Gd	<0.5
~~N~~		Br		Tb	<0.05
O	Major	Rb		Dy	<0.05
F	<1	Sr	~3000	Ho	<0.05
Na	25	Y	7.0	Er	<0.05
Mg	1.0	Zr	150	Tm	<0.05
Al	11	Nb	<0.1	Yb	<0.05
Si	Major	Mo	0.25	Lu	<0.05
P	1.6	Ru		Hf	
S	2.0	Rh		~~Ta~~	
Cl	0.60	Pd		W	<0.1
K	0.62	Ag	<1	Re	
Ca	115	Cd		Os	
Sc	0.090	In		Ir	
Ti	0.40	Sn	<0.1	Pt	0.3
V	0.045	Sb	0.12	Au	
Cr	≤0.5	Te		Hg	
Mn	0.085	I		Tl	
Fe	6.2	Cs		Pb	0.20
Co	≤0.01	Ba	2.0	Bi	<0.05
Ni	0.15	La	Major	Th	<0.01
Cu	≤0.2	Ce	3.0	U	<0.01
All other elements <0.1ppmw * Major >1wt%					

First of all, in the trace element analysis of 1%Sr-doped langasite, the Sr concentration was found to be ~3000ppmw (i.e. 0.3wt%), with approximate error of ±1000ppmw, close to the intended Sr doping level of 1mol% or 0.4wt% (see Table 5, p.61). In addition, we can see that the concentrations of background impurities in the 1%Sr-doped sample were orders of magnitude lower, indicating that Sr was indeed controlling the langasite transport properties.

In nominally undoped langasite, the major background impurity was Na at 100ppmw. Na is found to go into the Thomson cube site [54], i.e. substituting for La, and therefore acted as an acceptor $Na_{La}^{''}$. In principle, langasite can have cation nonstoichiometry for which the cation deficiency can also act as acceptor. However, we have no evidence for cation nonstoichiometry in langasite, and therefore assume that the extrinsic dopant dominates the defect properties.

In the ionic conduction regime, the Brouwer approximation $Na_{La}^{''} \approx V_O^{\bullet\bullet}$ is applicable. If we convert the Na impurity in nominally undoped langasite from ppmw to #/cm^3, we obtain 1.5×10^{19} cm^{-3}, and therefore expect the oxygen vacancy concentration for nominally undoped langasite to be 1.5×10^{19} cm^{-3}. The oxygen vacancy mobility can then be calculated (see Discussion).

Appendix C

ZnO Film on QCM

Experimental

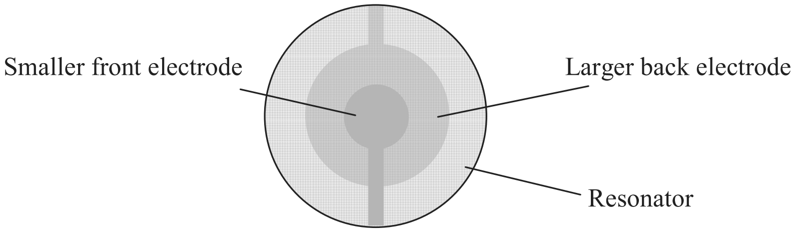

Figure 98: Resonator with asymmetric electrodes. The two electrodes are of different surface area, with the back electrode larger than the front.

This appendix describes preliminary work to examine the effect of change in electrode area on resonant frequency. For the active film material, we used ZnO, normally insulating at room temperature, but becomes conductive with UV irradiation as electrons are excited to its conduction band (ZnO optical bandgap is 3.3 eV [160]). The ZnO films were sputtered onto AT-cut quartz resonators (5MHz, Maxtek Inc, Part #149211-2) with asymmetric Au electrodes, as shown in Figure 98. Two different thicknesses of sputtered ZnO films, 150 and 200nm, were fabricated. The surface area of ZnO was identical to that of the larger electrode on the quartz resonator, so when it became conductive, the area of the smaller electrode increased to that of the larger electrode.

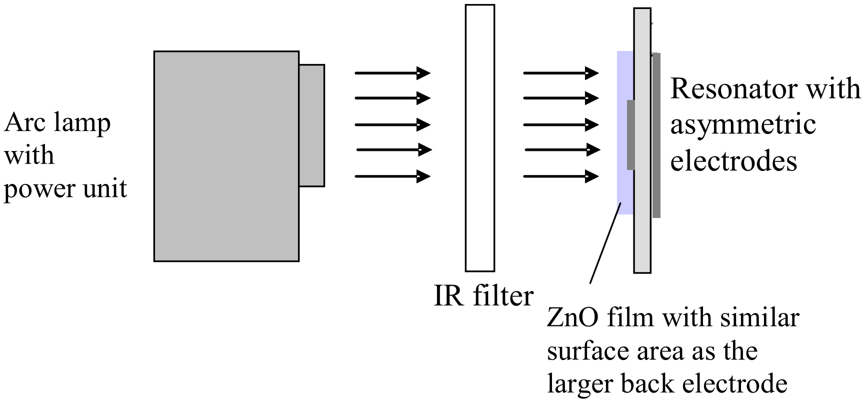

Figure 99: Experimental setup for ZnO-Quartz sensor.

The sensor was placed in the optical path of an arc lamp (set at 15A 20V) (Schoeffel Instrument Corporation, LH-151N/2 with power supply LPS-225HR), with an IR filter (Newport Corporation, #20HMS-0) placed in the light path between the lamp and the sensor to block IR radiation that heats up the sensor (see Figure 99). The experiment was performed in dark, with only light from the lamp. Resonant frequency shifts (labeled ‘ZnO-side’, Figure 100) were observed when the arc lamp was turned on, irradiating the ZnO film and making it conductive. When the same experiment was performed with the larger electrode facing the light path, effectively blocking the light on the ZnO film, a much smaller shift was observed (labeled ‘Blank-side’, Figure 100). The net frequency changes of ZnO films of different thicknesses, obtained by subtracting frequency change on ‘Blank-side’ from ‘ZnO-side’, were also shown in Figure 100 (labeled ‘Net change’).

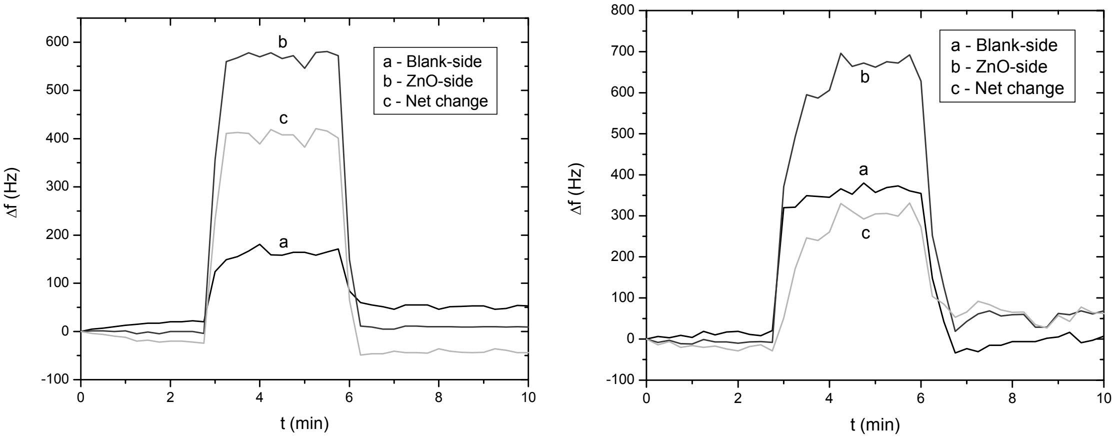

Figure 100: Resonant frequency change of ZnO active film, 120nm(left) and 200nm(right), on 5MHz AT-cut quartz resonator.

Discussion

One explanation for those observations was proposed by H. Fritze, our collaborator at University of Clausthal in Germany. He explained that the increase in frequency was due to an apparent decrease in effective areal mass density. The mass of the film remained constant, but as the film became conductive, it became part of the electrode, effectively increased the electrode area and therefore the areal mass density (ρ_s) decreased. The

Sauerbrey equation (Eq.(6), p.27) shows that $\Delta f \propto -\rho_s$, and a decrease in areal mass density will translate to an increase in resonant frequency of the resonator.

In our experiment, the effective electrode area tripled (0.49π to $1.5\pi \text{cm}^2$) once ZnO became conductive, effectively reducing the areal mass density of ZnO film on the resonator by two-third. As ZnO has density of 5.6g/cm^3 [161], the values of areal mass density of the active films were around 670ng/cm^2 and 1120ng/cm^2 for 120nm and 200nm thick ZnO films respectively. Two-third reduction of areal mass density translates to frequency shifts of around +447Hz and +747Hz for 120nm and 200nm ZnO films respectively (sensitivity of $1\ \text{Hz.cm}^2/\text{ng}$).

The results in Figure 100 show net frequency shifts of 400 and 350Hz for 120nm and 200nm thick ZnO film respectively. The frequency change in 120nm ZnO film was close to the expected frequency change due to two-third reduction in areal mass density. However, for the 200nm ZnO film, the frequency change was much lower than the expected frequency change. To understand this interesting phenomenon, it should be studied in greater details in future work.

Appendix D

Setting up Agilent E5100A

The correct use of the network analyzer (Agilent E5100A) is important for precise frequency measurements. This appendix section lists the procedures for setting up the analyzer for measurement.

Initialization

The network analyzer has an internal frequency standard (heated quartz resonator) which should be allowed to warm up and equilibrate before any measurements are performed. This initialization period is about 15-30min depending on room temperature.

Calibration

When a new sensor holder or new wiring is used, calibration should be performed on the network analyzer. Before calibration, a calibration standard has to be defined; a resistor is usually used. To define the calibration standard, select 'CAL', follow by 'Modify Cal Kit'. Select 'LOAD' to define the standard.

The calibration procedures are initiated by pressing the 'CAL' button, and selecting the three-term calibration. The calibration involved measuring 'SHORT' – when a piece of copper wire is connected in place of a resonator, 'OPEN' – when the holder is left empty, and 'LOAD' – when the calibration standard (e.g. a resistor with known resistance) is placed in the holder. After calibration is completed, the calibration data can be saved and recalled whenever a measurement needs to be performed.

Periodic calibration should be performed to ensure that the holder or the wiring has not changed. Before each measurement, one should check that the correction is applied.

Measurement Parameters

The following parameters were found to work well at high temperature (i.e. lower noise to signal ratio):

Power: 1mW
Point-per-scan: >1000
IF Bandwidth: <1kHz

Setting a high point-per-scan and low IF bandwidth will slow down each scan. With the above parameters, the analyzer can make about 1 reading per second.

Extracting f_r

There is two basic way of extracting f_r. The first is to let the analyzer fit the spectrum using the build-in equivalent circuit model. The second is to record each spectrum and analyze them off-line. At low temperature where Q is generally high, letting the machine fit the spectrum seems to be a fast way of measurement. However, as Q drops, the machine fitting gets noisier. The second method should be used for reliable f_r measurements at high temperature.

Bibliography

[1] Nanto, H., Y. Douguchi, K. Yokoi, T. Mukai, E. Kusano, and A. Kinbara. *Smart electronic nose using polymer-film-coated quartz resonator gas sensor for identification of harmful gases*. in *Internal Standardization and Calibration Architectures for Chemical Sensors*. 1999. Boston, MA, USA: SPIE-Int. Soc. Opt. Eng, USA. p. 317-327.

[2] Spassov, L., D.Y. Yankov, A.N. Mogilevski, and A.D. Mayorov, *Piezoelectric sorption sensor for mercury vapors in air using a quartz resonator.* Review of Scientific Instruments, 1993. **64**(1): p. 225-227.

[3] Benes, E., M. Gröschl, W. Burger, and M. Schmid, *Sensors based on piezoelectric resonators.* Sensors and Actuators A, 1995. **48**: p. 1-21.

[4] Frye, G.C., S.J. Martin, and R.W. Cernosek, *Portable acoustic wave sensor systems.* Ultrasonic Symposium, 1991: p. 311-316.

[5] Mandelis, A. and C. Christofides, *Piezoelectric quartz crystal microbalance sensors*, in *Physics, chemistry and technology of solid state gas sensor devices*. 1993, Wiley: New York, NY. p. 179-217.

[6] Reibel, J., U. Stahl, T. Wessa, and M. Rapp, *Gas analysis with SAW sensor systems.* Sensors and Actuators B, 2000. **65**: p. 173-175.

[7] Schramm, U., D. Meinhold, S. Winter, C. Heil, J. Muller-Albrecht, L. Wachter, H. Hoff, C.E.O. Roesky, T. Rechenbach, P. Boeker, P.S. Lammers, E. Weber, and J. Bargon, *A QMB-based temperature-modulated ammonia sensor for humid air.* Sensors and Actuators B, 2000. **67**(3): p. 219-226.

[8] Drafts, B., *Acoustic wave technology sensors.* Sensors, 2000. **17**(10): p. 68-71.

[9] Rabe, J., V. Seidermann, and S. Buettgenbach. *Monolithic fabrication of wireless miniaturized quartz crystal microbalance (QCM-R) array for biochemical sensing*. in *IEEE International Solid-State Sensors and Actuators Conference*. 2003. Boston, MA, USA: IEEE, Piscataway, NJ, USA. p. 1875-1876.

[10] Li, L., T. Abe, and M. Esashi. *High sensitive, miniaturized plano-convex quartz crystal microbalance fabricated by reactive ion etching and melting photoresist*. in *IEEE International Solid-State Sensors and Actuators*. 2003. Boston, MA, USA: IEEE, Piscataway, NJ, USA. p. 508-511.

[11] Casalnuovo, S.A., E.J. Heller, V.M. Hietala, A.G. Baca, R. Kottenstette, S.L. Hietala, J.L. Reno, and G.C. Frye-Mason. *Acoustic wave chemical microsensors in GaAs*. in *Micromachined Devices and Components IV*. 1998. Santa Clara, CA, USA: SPIE-Int. Soc. Opt. Eng, USA. p. 103-110.

[12] Rabe, J., S. Buttgenbach, J. Schroder, and P. Hauptmann, *Monolithic miniaturized quartz microbalance array and its application to chemical sensor systems for liquids.* IEEE Sensors Journal, 2003. **3**(4): p. 361-368.

[13] Schneider, T.W., G.C. Frye-Mason, S.J. Martin, J.J. Spates, T.V. Bohuszewicz, G.C. Osbourn, and J.W. Bartholomew. *Chemically selective coated quartz crystal microbalance (QCM) array for detection of volatile organic chemicals*. in *Chemical Microsensors and Applications*. 1998. Boston, MA, USA: SPIE-Int. Soc. Opt. Eng, USA. p. 85-94.

[14] Zhang, C. *A micro-acoustic wave sensor for engine oil quality monitoring*. in *IEEE International Frequency Control Symposium*. 2003. Tampa, Fl, USA: IEEE, Piscataway, NJ, USA. p. 971-977.

[15] Bell, J., T. Koehler, and D. Woermann, *Change of the resonance frequency of a quartz crystal microbalance in contact with an aqueous dispersion of solid particles.* Physical Chemistry Chemical Physics, 1997. **101**(6): p. 879-883.

[16] Clayton, L.D. and E.P. Eernisse. *Application of finite element analysis to the design of quartz thickness-shear mode pressure sensors*. in *IEEE International Frequency Control Symoposium*. 1996. Honolulu, HI, USA. p. 541-549.

[17] Azcondo, F.J. and J. Peire. *Quartz crystal oscillator used as temperature sensor*. in *International Conference on Industrial Electronics, Control and Instrumentation*. 1991. Kobe, Japan. p. 2580-2585.

[18] Muramatsu, H., K. Kimura, T. Ataka, R. Homma, Y. Miura, and I. Karube, *Quartz crystal viscosity sensor for monitoring coagulation reaction and its application to a multichannel coagulation detector.* Biosensors & Bioelectronics, 1991. **6**(4): p. 353-358.

[19] Thalhammer, R., S. Braun, B. Devcic-Kuhar, M. Groschl, F. Trampler, E. Benes, H. Nowotny, and M. Kostal, *Viscosity sensor utilizing a piezoelectric thickness shear sandwich resonator.* IEEE Transactions on Ultrasonics, Ferroelectrics and Frequency Control, 1998. **45**(5): p. 1331-1339.

[20] Cheeke, J.D.N. and Z. Wang, *Acoustic wave gas sensors.* Sensors and Actuators B (Chemical), 1999. **B59**(2-3): p. 146-53.

[21] Cernosek, R.W., J.R. Bigbie, M.T. Anderson, J.H. Small, and P.S. Sawyer. *High-temperature hydrocarbon gas sensing with mesoporous SiO_2 thin films on TSM resonators*. in *Solid-State Sensor and Actuator Workshop*. 1998. Hilton Head Island, South Carolina. p. 375-378.

[22] Avramov, I.D. *The RF-powered surface wave sensor oscillator - a successful alternative to passive wireless sensing*. in *Proceedings of the 2003 IEEE International Frequency Control Symposium and PDA Exhibition. Jointly with the*

17th European Frequency and Time Forum, 4-8 May 2003. 2003. Tampa, FL, USA: IEEE. p. 911-17.

[23] Schmidt, F., O. Sczesny, C. Ruppel, and V. Magori, *Wireless interrogator system for SAW-identification-marks and SAW-sensor components.* IEEE International Frequency Control Symposium, 1996: p. 208-215.

[24] Hollinger, R.D., A.R. Tellakula, C.-T. Li, V.V. Varadan, and V.K. Varadan, *Wireless surface acoustic wave-based humidity sensor.* Proceedings of the SPIE - The International Society for Optical Engineering, 1999. **3876**: p. 54-62.

[25] Springer, A., R. Weigel, A. Pohl, and F. Seifert. *Wireless identification and sensing using surface acoustic wave device*. in *Proceedings of Mechatronics '98, 9-11 Sept. 1998*. 1998. Skovde, Sweden: Elsevier Science. p. 559-64.

[26] Dong, Y., W. Cheng, S. Wang, Y. Li, and G. Feng, *A multi-resolution passive SAW chemical sensor.* Sensors and Actuators B (Chemical), 2001. **B76**(1-3): p. 130-3.

[27] Haines, J., O. Cambon, D.A. Keen, M.G. Tucker, and M.T. Dove, *Structural disorder and loss of piezoelectric properties in alpha -quartz at high temperature.* Applied Physics Letters, 2002. **81**(16): p. 2968-70.

[28] Dolino, G., *The alpha-beta transitions of quartz: a century of research on displacive phase transitions.* Phase Transitions, 1990. **A21**(1): p. 59-72.

[29] Gouhara, K., Y.H. Li, and N. Kato, *Studies on the alpha - beta transition of quartz by means of in situ X-ray topography.* Journal of the Physical Society of Japan, 1983. **52**(11): p. 3821-8.

[30] Ferris, J.E. and J.J. Martin. *High-temperature acoustic loss of AT-cut quartz crystals*. in *Proceedings of the 1994 IEEE 48th Annual Symposium on Frequency Control, Jun 1-3 1994*. 1994. Boston, MA, USA: IEEE, Piscataway, NJ, USA. p. 115-121.

[31] Yoon, D.-H., I. Yonenaga, T. Fukuda, and N. Ohnishi, *Crystal growth of dislocation-free* $LiNbO_3$ *single crystals by micro pulling down method.* Journal of Crystal Growth, 1994. **142**: p. 339-343.

[32] Ozawa, M. and S. Suguki, *Conductive characteristics of* $LiNbO_3$ *longitudinal resonator at elevated temperatures.* Journal of Materials Science Letters, 1995. **14**(6): p. 396-397.

[33] Kuznetsova, I.E., B.D. Zaitsev, S.G. Joshi, and I.A. Borodina, *Investigation of acoustic waves in thin plates of lithium niobate and lithium tantalate.* IEEE Transactions on Ultrasonics, Ferroelectrics and Frequency Control, 2001. **48**(1): p. 322-328.

[34] Martin, F., M.I. Newton, G. McHale, K.A. Melzak, and E. Gizeli, *Pulse mode shear horizontal-surface acoustic wave (SH-SAW) system for liquid based sensing applications.* Biosensors & Bioelectronics, 2004. **19**(6): p. 627-632.

[35] Sato, T. and H. Abe, *SAW device applications of longitudinal leaky surface waves on lithium tetraborate.* IEEE Transactions on Ultrasonics, Ferroelectrics and Frequency Control, 1998. **45**(6): p. 1506-1516.

[36] Shestopalov, K.V., V.A. Nefedov, and B.I. Zadneprovsky. *Lithium tetraborate as a promising material for BAW filters*. in *IEEE International Frequency Control Symposium*. 1994. p. 301-307.

[37] Damjanovic, D., *Materials for high temperature piezoelectric tranducers.* Current Opinion in Solid State & Materials Science, 1998. **3**: p. 469-473.

[38] Moseley, P.T. and B.C. Tofield, eds. *Solid-state gas sensor*. 1987, A Hilger. 245.

[39] Ballantine, D.S., R.M. White, S.J. Martin, A.J. Ricco, E.T. Zellers, G.C. Frye, and H. Wohltjen, *Acoustic wave sensors: theory, design, and physico-chemical applications*. Applications of modern acoustics. 1997, San Diego: Academic Press. 436.

[40] Gopel, W. and K.D. Schierbaum, *SnO_2 sensors: current status and future prospects.* Sensors and Actuators B, 1995. **26**(1-3): p. 1-12.

[41] Sasaki, I., H. Tsuchiya, M. Nishioka, M. Sadakata, and T. Okubo, *Gas sensing with zeolite-coated quartz crystal microbalances-principal component analysis approach.* Sensors and Actuators B, 2002. **86**: p. 26-33.

[42] Martin, S.J., G.C. Frye, J.J. Spates, and M.A. Butler. *Gas sensing with acoustic devices*. in *1996 IEEE Ultrasonics Symposium. Proceedings, 3-6 Nov. 1996*. 1996. San Antonio, TX, USA: IEEE. p. 423-34.

[43] Laik, B., P. Poizot, and J.-M. Tarascon, *The electrochemical quartz crystal microbalance as a means for studying the reactivity of Cu_2O toward lithium.* Journal of the Electrochemical Society, 2002. **149**(3): p. A251-A255.

[44] Schramm, U., C.E.O. Roesky, S. Winter, T. Rechenbach, P. Boeker, P.S. Lammers, E. Weber, and J. Bargon, *Temperature dependence of an ammonia sensor in humid air based on a cryptophase-coated quartz microbalance.* Sensors and Actuators B, 1999. **57**: p. 233-237.

[45] Topart, P.A., *Applications of the quartz crystal microbalance to the characterization of thin conducting polymer films used for vapor detection*, in *Fakultät für Elektrotechnik, Institut für Physik*. 1993, Universität der Bundeswehr München: München, Germany. p. 111.

[46] Zelenka, J., *Piezoelectric Resonators and their Applications*. 1986, New York: Elsevier.

[47] Fritze, H., H.L. Tuller, G. Borchardt, and T. Fukuda, *High temperature properties of langasite.* Materials Research Society Symposium Proceedings, 1999. **604**: p. 65-70.

[48] Fritze, H., H.L. Tuller, H. Seh, and G. Borchardt, *High temperature nanobalance sensor based on langasite.* Sensors and Actuators B, 2001. **76**: p. 103-107.

[49] Fritze, H., H. Seh, O. Schneider, H.L. Tuller, and G. Borchardt, *High temperature properties of langasite and gallium orthophosphate and their relevance to sensor applications.* Proceedings of MRS Symposium, 2003. **756**: p. 181-186.

[50] Fritze, H., O. Schneider, H. Seh, H.L. Tuller, and G. Borchardt, *High temperature bulk acoustic wave properties of langasite.* Physical Chemistry and Chemical Physics, 2003. **5**(23): p. 5207-5214.

[51] Thiele, J.A. and M.P.d. Cunha. *High temperature SAW gas sensor on langasite*. in *IEEE Sensors*. 2003. Toronto, Canada: IEEE. p. 769-772.

[52] Cunha, M.P.D. and J.A. Thiele, *High temperature surface acoustic wave devices: fabrication and characterisation.* Electronics Letters, 2003. **39**(10): p. 818-819.

[53] Honal, M., R. Fachberger, T. Holzheu, E. Riha, E. Born, P. Pongratz, and A. Bausewein, *Langasite surface acoustic sensors for high temperatures.* IEEE International Frequency Control Symposium, 2000: p. 113-118.

[54] Mill, B.V. and Y.V. Pisarevsky, *Langasite-type materials: from discovery to present state.* IEEE/EIA International Frequency Control Symposium and Exhibition, 2000: p. 133-144.

[55] Smythe, R.C., R.C. Helmbold, G.E. Hague, and K.A. Snow, *Langasite, langanite and langatate resonators: recent results.* Joint Meeting EFTF-IEEE IFCS, 1999. **2**: p. 816-820.

[56] Smythe, R.C., *Material and resonator properties of langasite and langatate: a progress report.* IEEE International Frequency Control Symposium, 1998: p. 761-765.

[57] Smythe, R.C., R.C. Helmbold, G.E. Hague, and K.A. Snow, *Langasite, langanite and langatate: bulk-wave y-cut resonators.* IEEE Transactions on Ultrasonics, Ferroelectrics and Frequency Control, 2000. **47**(2): p. 355-360.

[58] Ruffieux, D., M.A. Dubois, and N.F.d. Rooij. *AlN piezoelectric microactuator array*. in *IEEE MEMS*. 2000. p. 662-667.

[59] Benetti, M., D. Cannata, F.D. Pietrantonio, and E. Verona. *Growth of AlN piezoelectric films on diamond for high frequency SAW devices*. in *IEEE Ultrasonics Symposium*. 2003. p. 1738-1741.

[60] Zhong, F., C. Huang, and G.W. Auner. *AlN acoustic wave sensors using excimer laser micromachining techniques*. in *Materials Research Society Symposium*. 2001. Boston, MA, USA. p. G11.28.1-G11.28.6.

[61] Pettersen, S.V., T. Tybell, A. Ronnekleiv, S. Rooth, V. Schwegler, and J.K. Grepstad. *Surface acoustic wave resonator from thick MOVPE-grown layers of GaN(001) on sapphire*. in *Materials Research Society Symposium*. 2002. Boston, MA, USA. p. 461-466.

[62] Cunha, M.P.D., T.B. Pollard, H. Whitehouse, and P.M. Worsch. *$GaPO_4$ SAW devices: measured and predicted propagation properties*. in *IEEE Ultrasonic Symposium*. 2003. p. 110-113.

[63] Krempl, P.W. *Quartz homeotypic gallium orthophosphate - a new high tech piezoelectric material*. in *IEEE Ultrasonics Symoposium*. 1994. p. 949-954.

[64] Krempl, P., G. Schleinzer, and W. Wallnofer, *Gallium phosphate: a new piezoelectric crystal material for high-temperature sensorics.* Sensors and Actuators A, 1997. **61**(1-3): p. 361-363.

[65] Thanner, H., P.W. Krempl, W. Wallnofer, and P.M. Worsch, *$GaPO_4$ high temperature crystal microbalance with zero temperature coefficient.* Vacuum, 2002. **67**: p. 687-691.

[66] Worsch, P.M., P.W. Krempl, and W. Wallnofer, *$GaPO_4$ crystals for sensor applications.* Proceedings of IEEE Sensors, 2002: p. 589-593.

[67] Krispel, F., H. Thanner, P.W. Krempl, C. Reiter, P.M. Worsch, and W. Wallnofer, *$GaPO_4$ resonators with Q factors of some millions in the fundamental mode.* Proceedings of IEEE International Frequency Control Sumposium, 2002: p. 342-346.

[68] Hornsteiner, J., E. Born, G. Fischerauer, and E. Riha, *Surface acoustic wave sensors for high temperature applications.* Proceeding IEEE Frequency Control Symposium, 1998: p. 615-620.

[69] Chani, V.I., H. Takeda, and T. Fukuda, *Liquid phase epitaxy of films with langasite structure.* Materials Science and Engineering, 1999. **B60**: p. 212-216.

[70] Uda, S. and O. Buzanov, *Growth of a 3 inches langasite crystal with clear faceting.* Journal of Crystal Growth, 2000. **211**(1): p. 318-324.

[71] Uda, S., S.Q. Wang, N. Konishi, H. Inaba, and J. Harada, *Growth habits of 3 and 4-inch langasite single crystals.* Journal of Crystal Growth, 2002. **237-239**(1-4): p. 707-713.

[72] Sakharov, S.A., A.N. Zabelin, O.A. Buzanov, A.V. Medvedev, V.V. Alenkov, S.N. Kondratiev, and S.A. Zhgoon. *Nondestructive investigation of 4-inch langasite wafer acoustic homogeneity*. in *IEEE Ultrasonics Symposium*. 2002. p. 227-230.

[73] Cunha, M.P.d., E.L. Adler, and D.C. Malocha, *BAW temperature sensitivity and coupling in langanite.* IEEE Ultrasonics Symposium, 1999: p. 883-886.

[74] Sakharov, S.A., I.M. Larionov, and A.V. Medvedev, *Application of langasite crystals in monolithic filters operating in shear modes.* IEEE Frequency Control Symposium, 1992: p. 713-723.

[75] Sakharov, S., P. Senushenov, A. Medvedev, and Y. Pisarevsky, *New data on temperature stability and acoustical losses of langasite crystals.* IEEE International Frequency Control Symposium, 1995: p. 647-652.

[76] Silvestrova, I.M., V.V. Bezdelkin, P.A. Senyushenkov, and Y.V. Pisarevsky, *Present Stage of* $La_3Ga_5SiO_{14}$ *- Research.* IEEE International Frequency Control Symposium, 1993: p. 348-350.

[77] Grouzinenko, V.B. and V.V. Bezdelkin, *Piezoelectric resonators from* $La_3Ga_5SiO_{14}$ *(langasite) - single crystals.* IEEE Frequency Control Symposium, 1992: p. 707-712.

[78] Kaminskii, A.A., B.V. Mill, G.G. Khodzhabagyan, A.F. Konstantinova, A.I. Okorochkov, and I.M. Silvestrova, *Investigation of Trigonal* $(La_{1-x}Nd_x)_3Ga_5SiO_{14}$ *crystals: I. Growth and optical properties.* Physica Status Solidi A, 1983. **80**: p. 387-398.

[79] Kumatoriya, M., H. Sato, J. Nakanishi, T. Fujii, M. Kadota, and Y. Sakabe, *Crystal growth and electromechanical properties of Al substituted langasite* $(La_3Ga_{5-x}Al_xSiO_{14})$*.* Journal of Crystal Growth, 2001. **229**: p. 289-293.

[80] Chai, B.H.T., A.N.P. Bustamante, and M.C. Chou, *A new class of ordered langasite structure compounds.* IEEE International Frequency Control Symposium, 2000: p. 163-168.

[81] Chai, B., H. Qiu, Y.Y. Ji, and J.L. Lefaucheur. *Growth of high quality single domain crystals of langasite family compounds*. in *Joint Meeting EFTF - IEEE IFCS*. 1999. p. 821-828.

[82] Chai, B., J.L. Lefaucheur, Y.Y. Ji, and H. Qiu, *Growth and evaluation of large size LGS* $(La_3Ga_5SiO_{14})$*, LGN* $(La_3Ga_{5.5}Nb_{0.5}O_{14})$ *and LGT* $(La_3Ga_{5.5}Ta_{0.5}O_{14})$

single crystals. IEEE International Frequency Control Symposium, 1998: p. 748-760.

[83] Takeda, H., T. Kato, V.I. Chani, H. Morikoshi, K. Shimamura, and T. Fukuda, *Effect of (Sr, Ba) substitution in $La_3Ga_5SiO_{14}$ and $La_3M_{0.5}Ga_{5.5}O_{14}$ ($M=Nb^{5+}$, Ta^{5+}) crystals on their synthesis, structure and piezoelectricity.* Journal of Alloys and Compounds, 1999. **290**: p. 79-84.

[84] Zarka, A., B. Capelle, J. Detaint, and D. Cochet-Muchy, *New results on high perfection langasite crystals: studies of crystalline defects and modes shapes.* IEEE International Frequency Control Symposium, 1995: p. 629-637.

[85] Buzanov, O.A., A.V. Naumov, V.V. Nechaev, and S.N. Knyazev, *A new approach to the growth of langasite crystals.* IEEE International Frequency Control Symposium, 1996: p. 131-136.

[86] Fukuda, T., H. Takeda, K. Shimamura, H. Kawanaka, M. Kumatoriya, S. Murakami, J. Sato, and M. Sato. *Growth of new langasite single crystals for piezoelectric applications*. in *11th IEEE International Symposium on Applications of Ferroelectrics*. 1998. Piscataway, NJ. p. 315-319.

[87] Jung, I.H. and K.H. Auh, *Crystal growth and piezoelectric properties of langasite crystals.* Materials Letters, 1999. **41**: p. 241-246.

[88] Gotalskaya, A.N., D.I. Drezin, V.V. Bezdelkin, and V.N. Stassevich, *Pecularities of technology, physical properties and applications of new piezoelectric material langasite ($La_3Ga_5SiO_{14}$).* IEEE International Frequency Control Symposium, 1993: p. 339-347.

[89] Dubovik, M.F., K.A. Katrunov, and T.I. Korshikova, *The nature of langasite crystal's coloration.* IEEE International Frequency Control Symposium, 1995: p. 638-641.

[90] Dubovik, M.F., Y.A. Zagoruiko, and T.I. Korshikova, *Influence of thermal treatment and radiation on some electrophysical parameters of langasite crystals.* IEEE International Frequency Control Symposium, 1996: p. 84-89.

[91] Saitoh, A., Y. Asari, and T. Nomura. *Study of Gas Sensor based on Adsorption Heat Measurement Using Y-cut Quartz Crystal Microbalance*. in *First IEEE International Conference on Sensors - IEEE Sensors 2002, Jun 12-14 2002*. 2002. Orlando, FL, United States: Institute of Electrical and Electronics Engineers Inc. p. 435-438.

[92] Vig, J.R., R.L. Filler, and Y. Kim, *Chemical sensor based on quartz microresonators.* Journal of Microelectromechanical Systems, 1996. **5**(2): p. 138-140.

[93] Thornell, G., F. Ericson, C. Hedlund, J. Ohrmaim, J.-A. Schweitz, and G. Portnoff, *Residual stress in sputtered gold films on quartz measured by the cantilever beam deflection technique.* IEEE Transactions on Ultrasonics, Ferroelectrics and Frequency Control, 1999. **46**(4): p. 981-92.

[94] Benjaminson, A. and S.C. Stallings. *A microcomputer-compensated crystal oscillator using a dual-mode resonator*. in *Proceedings of the 43rd Annual Symposium on Frequency Control 1989 (Cat. No.89CH2690-6), 31 May-2 June 1989*. 1989. Denver, CO, USA: IEEE. p. 20-6.

[95] Kusters, J.A., M.C. Fischer, and J.G. Leach. *Dual model operation of temperature and stress compensated crystals*. in *Proceedings of the 32nd Annual Symposium on Frequency Control 1978, 31 May-2 June 1978*. 1978. Atlantic City, NJ, USA: Electronic Industries Assoc. p. 389-97.

[96] Abramson, I.V. *Two-mode quartz resonators for digital temperature compensated quartz oscillators*. in *Proceedings of the 1992 IEEE Frequency Control Symposium (Cat. No.92CH3083-3), 27-29 May 1992*. 1992. Hershey, PA, USA: IEEE. p. 442-7.

[97] Pierce, D.E., Y. Kim, and J.R. Vig. *A temperature insensitive quartz microbalance*. in *Proceedings of International Frequency Control Symposium, 28-30 May 1997*. 1997. Orlando, FL, USA: IEEE. p. 41-8.

[98] Vig, J.R., *Temperature-insensitive dual-mode resonant sensors-a review.* IEEE Sensors Journal, 2001. **1**(1): p. 62-8.

[99] Yoo, H.-I., C.-R. Song, and D.-K. Lee, *$BaTiO_{3-d}$:Defect structure, electrical conductivity, chemical diffusivity, thermoelectric power, and oxygen nonstoichiometry.* Journal of Electroceramics, 2002. **8**(1): p. 5-36.

[100] Porat, O., H.L. Tuller, M. Shelef, and E.M. Logothetis, *Electrical conductivity and nonstoichiometry in $Pr_{0.545}Ce_{0.455}O_{2-x}$.* Materials Research Society Symposium, 1997. **453**: p. 531-535.

[101] Porat, O. and H.L. Tuller, *Oxygen nonstoichiometry and defects in Mn-doped $Gd_2Ti_2O_{7+x}$.* Journal of American Ceramic Society, 1996. **79**(12): p. 3078-3082.

[102] Knauth, P. and H.L. Tuller, *Nonstoichiometry and relaxation kinetics of nanocrystalline mixed praseodymium-cerium oxide $Pr_{0.7}Ce_{0.3}O_{2-x}$.* J. Euro. Ceram. Soc., 1999. **19**(6-7): p. 831-836.

[103] Narine, S.S. and A.J. Slavin, *Use of the quartz crystal microbalance to measure the mass of submonolayer deposits: Measuring the stoichiometry of surface oxides.* Journal of Vacuum Science & Technology A (Vacuum, Surfaces, and Films), 1998. **16**(3): p. 1857-62.

[104] Rahtu, A., T. Alaranta, and M. Ritala, *In situ quartz crystal microbalance and quadrupole mass spectrometry studies of atomic layer deposition of aluminum oxide from trimethylaluminum and water.* Langmuir, 2001. **17**(21): p. 6506-9.

[105] Etchenique, R. and E.J. Calvo, *Electrochemical quartz crystal microbalance gravimetric and viscoelastic studies of nickel hydroxide battery electrodes.* Journal of the Electrochemical Society, 2001. **148**(4): p. 361-7.

[106] Fricoteaux, P. and O. Savadogo, *Quartz microbalance investigation of nickel electrodeposited in sulphuric acid with and without silicotungstic acid (STA).* Journal of New Materials for Electrochemical Systems, 2004. **7**(1): p. 59-63.

[107] Jope, D., J. Sell, H.W. Pickering, and K.G. Weil, *Application of a quartz crystal microbalance to the study of copper corrosion in acid solution inhibited by triazole-iodide protective films.* Journal of the Electrochemical Society, 1995. **142**(7): p. 2170-3.

[108] Park, H.-K., K. Podolske, Z. Munshi, W.H. Smyrl, and B.B. Owens, *Quartz crystal microbalance and electrochemical studies of Li intercalation in* V_6O_{13}. Journal of the Electrochemical Society, 1991. **138**(2): p. 627-8.

[109] Phillips, T.E., C.B. Bargeron, and R.C. Benson, *Thermogravimetric analysis of selected condensed materials on a quartz crystal microbalance.* Journal of Vacuum Science & Technology A (Vacuum, Surfaces, and Films), 1995. **13**(6): p. 2726-31.

[110] Fritze, H., H. Seh, H.L. Tuller, and G. Borchardt, *Operation limits of langasite high temperature nanobalances.* Journal of the European Ceramic Society, 2001. **21**: p. 1473-1477.

[111] Maria, J.-P., S. Trolier-McKinstry, and D.G. Schlom. *Size effects in barium titanate thin film heterostructures with conductive oxide electrodes*. in *ISAF '96. Proceedings of the Tenth IEEE International Symposium on Applications of Ferroelectrics, 18-21 Aug. 1996*. 1996. East Brunswick, NJ, USA: IEEE. p. 333-6.

[112] Maier, J., *Point-defect thermodynamics and size effects.* Solid State Ionics, Diffusion & Reactions, 2000. **131**(1-2): p. 13-22.

[113] Stefanik, T.S. and H.L. Tuller. *Electrical conductivity in praseodymium-cerium oxide*. in *Solid State Ionics - 2002. Symposium, 2-5 Dec. 2002*. 2003. Boston, MA, USA: Mater. Res. Soc. p. 163-8.

[114] Stefanik, T.S., *Electrical properties and defect structures praseodymium-cerium oxide solid solution*, in *Department of Materials Science and Engineering*. 2004, Massachusetts Institute of Technology: Cambridge, MA.

[115] Knauth, P. and H.L. Tuller, *Nonstoichiometry and relaxation kinetics of nanocrystalline mixed praseodymium-cerium oxide Pr/sub 0.7/Ce/sub 0.3/O/sub 2-x/.* Journal of the European Ceramic Society, 1999. **19**(6-7): p. 831-6.

[116] Nomura, T., A. Saitoh, and S. Furukawa, *Surface acoustic wave vapor sensor using ultrathin multilayer films.* Joint Meeting EFTF - IEEE IFCs, 1999: p. 1082-1085.

[117] Rechenbach, T., U. Schramm, P. Boeker, G. Horner, C.E.O. Roesky, J. Trepte, S. Winter, R. Pollex, J. Bargon, E. Weber, and P.S. Lammers, *A humidity-independent ammonia sensor based on a quartz microbalance: a test under agricultural conditions.* Sensors and Actuators B, 1999. **57**: p. 255-260.

[118] Schlupp, M., C. Heil, A. Koch, J. Muller-Albrecht, U. Schramm, and J. Bargon, *Metal colloids as sensor-active materials for the detection of volatile compounds and solvents.* Sensors and Actuators B, 2000. **71**(1-2): p. 9-12.

[119] Seo, M., K. Yoshida, and K. Noda, *A quartz crystal microbalance study of the corrosion of iron thin films in neutral aqueous solutions.* Materials Science & Engineering A (Structural Materials: Properties, Microstructure and Processing), 1995. **A198**(1-2): p. 197-203.

[120] Grasjo, L., M. Seo, and N. Sato, *In-situ gravimetry of passivation of copper by means of quartz crystal microbalance.* Corrosion Science, 1990. **31**: p. 299-304.

[121] Koebel, M., M. Elsener, and G. Madia, *Recent advances in the development of urea-SCR for automotive applications.* SAE Technical Paper Series (2001-01-3625), 2001.

[122] Mital, R., J. Li, S.C. Huang, B.J. Stroia, and R.C. Yu, *Diesel exhaust emissions control for light duty vehicles.* SAE Technical Paper Series (2003-01-0041), 2003.

[123] Kim, Y.-W., J. Sun, I. Kolmanovsky, and J. Koncsol, *A phenomenological control oriented lean NOx trap model.* SAE Technical Paper Series (2003-01-1164), 2003.

[124] Choi, G.M., H.L. Tuller, and M.-J. Tsai, *Defects and Transport in* $YBa_2Cu_3O_{7-x}$, in *Non-Stoichiometric Compounds Surfaces, Grain Boundaries and Structural Defects*, J. Nowotny and W. Weppner, Editors. 1989, Kluwer Academic. p. 451-470.

[125] Knauth, P. and H.L. Tuller, *Thermodynamic properties of nanocrystalline praseodymium-cerium oxide* $Pr_{0.7}Ce_{0.3}O_{2-x}$. Ceramic Transactions, 1999. **92**.

[126] Knauth, P. and H.L. Tuller, *Electrical and defect thermodynamic properties of nanocrystalline titanium dioxide.* Journal of Applied Physics, 1999. **85**(2): p. 897-902.

[127] Kosacki, I., S. Kramer, and H.L. Tuller, *Non-stoichiometry and electrical transport in* $Gd_2(Ti_{1-x}Nb_x)_2O_7$. Diffusiona and Defect Data Part B: Solid State Phenomena, 1994. **39-40**: p. 117-121.

[128] Kosacki, I. and H.L. Tuller, *Electrical properties of donor and acceptor doped* $Gd_2Ti_2O_7$. MRS Symposium Proceedings, 1995. **369**: p. 703-708.

[129] Long, N.J., F. Lecarpentier, and H.L. Tuller, *Structure and electrical properties of Ni-substituted lanthanum gallate perovskites.* Journal of Electroceramics, 1999. **3**(4): p. 399-407.

[130] Moon, P.K. and H.L. Tuller, *Ionic conduction in the* $Gd_2Ti_2O_7$-$Gd_2Zr_2O_7$ *system.* Solid State Ionics, 1988. **28-30**: p. 470-474.

[131] Rotman, S.R. and H.L. Tuller, *Defect-property correlations in garnet crystals. VII: The electrical conductivity and defect structure of yttrium aluminum and yttrium iron garnet solid solutions.* Journal of Electroceramics, 1998. **2**(2): p. 95-104.

[132] Rotman, S.R., H.L. Tuller, M. Roth, and A. Linz, *Defect property correlations in garnet crystals. II. Electrical conductivity and optical absorption in* $Ca_3Al_2Ge_3O_{12}$. Journal of Applied Physics, 1985. **57**(12): p. 5320-5324.

[133] Rotman, S.R., R.P. Tandon, and H.L. Tuller, *Defect-property correlations in garnet crystals: the electrical conductivity and defect structure of luminescent cerium-doped yttrium aluminum garnet.* Journal of Applied Physics, 1984. **57**(6): p. 1951-1955.

[134] Tuller, H.L. and A.S. Nowick, *Defect structure and electrical properties of nonstoichiometric* CeO_2 *single crystals.* Journal of Electrochemical Society, 1979. **126**(2): p. 209-217.

[135] Malocha, D.C., M.P.d. Cunha, E. Adler, R.C. Smythe, S. Frederick, M. Chou, R. Helmbold, and Y.S. Zhou, *Recent measurements of material constants vs temperature for LGN, LGS and LGT.* IEEE International Frequency Control Symposium, 2000: p. 200-205.

[136] Smythe, R.C. and G.E. Hague, *Determination of the piezoelectric constants of LGN, LGS & LGT.* IEEE International Frequency Control Symposium, 2000: p. 191-194.

[137] Jung, I.H., Y.H. Kang, K. Joo, A. Yoshikawa, T. Fukuda, and K.H. Auh, $Ca_3Ga_2Ge_4O_{14}$ *(CGG)-type* $Sr_3Nb_{0.95}Ga_{3.083}Si_2O_{14}$ *single crystal grown by the Czochralski method for piezoelectric applications.* Materials Letters, 2001. **51**: p. 129-134.

[138] Jung, I.H., J.M. Ko, K.B. Shim, T. Fukuda, and K.H. Auh, *Influence of starting melt composition on* $La_3(Ta_xGa_{1-x})Ga_5O_{14}$ *crystals grown by Czochralski method.* Journal of Crystal Growth, 2000. **220**: p. 275-280.

[139] Jung, I.H., A. Yoshikawa, K. Lebbou, T. Fukuda, and K.H. Auh, *Crystal growth by micro-pulling-down of* $Ca_3Ga_2Ge_4O_{14}$ *(CGG) type-*$Sr_3Nb_{1-x}Ga_{3+(5/3)x}Si_2O_{14}$ *compounds.* Journal of Crystal Growth, 2001. **226**: p. 101-106.

[140] Jung, I.H., A. Yoshikawa, T. Fukuda, and K.H. Auh, *Growth and structure of* $A_3NbGa_3Si_2O_{14}$ *(A=Sr,Ca) compounds.* Journal of Alloys and Compounds, 2002. **339**: p. 149-155.

[141] Smyth, D.M., *The Defect Chemistry of Metal Oxides*. 2000, Oxford University Press.

[142] Kingery, W.D., H.K. Bowen, and D.R. Uhlmann, *Introduction to Ceramics*. 1976: John Wailey & Son.

[143] Chiang, Y.-M., D.B. III, and W.D. Kingery, *Physical Ceramics*. 1997: John Wiley & Sons, Inc.

[144] Tuller, H.L., *Mixed conduction in nonstoichiometric oxides*, in *Nonstoichiometric Oxides*, O.T. Sorensen, Editor. 1981, Academic Press: New York. p. 271-335.

[145] Fritze, H. and H.L. Tuller, *Langasite for high temperature bulk acoustic wave applications.* Applied Physics Letters, 2001. **78**: p. 976-977.

[146] Schulz, M., H. Fritze, H.L. Tuller, and H. Seh, *Diffusion related implications for langasite resonator operation.* IEEE Transactions on Ultrasonics, Ferroelectrics, and Frequency Control, 2004. **51**(11): p. 1381-1387.

[147] Hyodo, T., K. Sasahara, Y. Simizu, and M. Egashira, *Fabrication of macroporous* SnO_2 *thick film and its gas sensor application.* Chemical Sensors, 2003. **19B**: p. 220-222.

[148] Sasahara, K., T. Hyodo, Y. Shimizu, and M. Egashira, *Microporous and nanosized ceramic films prepared by modified sol-gel method with PMMA microsphere templates.* Journal of the European Ceramic Society, 2001. **24**: p. 1961-1967.

[149] Merkle, R. and J. Maier, *Defect association in acceptor-doped* $SrTiO_3$*: Case study for* $Fe_{Ti}'V_0$*and* $Mn_{Ti}''''V_0$*.* Physical Chemistry Chemical Physics, 2003. **5**(11): p. 2297-303.

[150] Wang, D.Y., D.S. Park, J. Griffith, and A.S. Nowick, *Oxygen-ion conductivity and defect interactions in yttria-doped ceria.* Solid State Ionics, 1981. **2**: p. 95-105.

[151] Kramer, S.A. and H.L. Tuller, *A novel titanate-based oxygen ion conductor:* $Gd_2Ti_2O_7$. Solid State Ionics, Diffusion & Reactions, 1995. **82**(1-2): p. 15-23.

[152] Taehwan, Y. and H.L. Tuller, *Ionic conduction and disorder in the* $Gd_2Sn_2O_7$ *pyrochlore system.* Solid State Ionics, Diffusion & Reactions, 1996. **86-88**(pt.1): p. 177-82.

[153] Tuller, H.L., *Oxygen ion conduction and structural disorder in conductive oxides.* Journal of the Physics and Chemistry of Solids, 1994. **55**(12): p. 1393-404.

[154] Fritze, H., M. Schulz, H. Seh, and H.L. Tuller. *High temperature operation and stability of langasite resonators*. in *Material Research Society Meeting*. 2004. Boston, MA: In press.

[155] Ashcroft, N.W. and N.D. Mermin, *Solid State Physics*. 1976: Saunders College Publishing.

[156] Ohmi, S., C. Kobayashi, I. Kashiwagi, C. Ohshima, H. Ishiwara, and H. Iwai, *Characterization of* La_2O_3 *and* Yb_2O_3 *thin films for high-k gate insulator application.* Journal of the Electrochemical Society, 2003. **150**(7): p. 134-40.

[157] Rebien, M., W. Henrion, M. Hong, J.P. Mannaerts, and M. Fleischer, *Optical properties of gallium oxide thin films.* Applied Physics Letters, 2002. **81**(2): p. 250-2.

[158] Scofield, J.H. and D.M. Fleetwood, *Physical basis for nondestructive tests of MOS radiation hardness.* IEEE Transactions on Nuclear Science, 1991. **38**(6, pt.1): p. 1567-77.

[159] Seh, H., H.L. Tuller, and H. Fritze, *Langasite for high-temperature acoustic wave gas sensors.* Sensors and Actuators B, 2003. **93**: p. 169-174.

[160] Verma, A.J., S. Sharma, S. Singh, A. Kapoor, and K.N. Tripathi, *Fabrication and characterization of ZnO thin films by envelope and waveguide methods.* Journal of Optics, 1996. **27**(1): p. 13-17.

[161] Lide, D.R., ed. *CRC Handbook of Chemistry and Physics*. 74th ed., CRC Press.